Heat Transfer and Flow Characteristics on the Rotor Tip and Endwall Platform Regions in a Transonic Turbine Cascade

Allan N. Arisi

Dissertation submitted to the faculty of the Virginia Polytechnic Institute and State University in partial fulfillment of the requirements for the degree of

Doctor of Philosophy

In

Mechanical Engineering

Wing F. Ng (Chair)

Srinath V. Ekkad

Thomas E. Diller

Walter F. O'Brien

K. Todd Lowe

December 4th, 2015

Blacksburg, Virginia, U.S.A.

Keywords: Gas Turbines, Heat Transfer, Squealer, Transonic, Secondary Flows, Film Cooling, Endwall, Rotor Tip, Experimental, Computational Fluid Dynamics

Heat Transfer and Flow Characteristics on the Rotor Tip and Endwall Platform Regions in a Transonic Turbine Cascade

Allan N. Arisi

ABSTRACT

This dissertation presents a detailed experimental and numerical analysis of the aerothermal characteristics of the turbine extremity regions i.e. the blade tip and endwall regions. The heat transfer and secondary flow characteristics were analyzed for different engine relevant configurations and exit Mach/Reynolds number conditions. The experiments were conducted in a linear blowdown cascade at transonic high turbulence conditions of M_{exit} ~ 0.85, 0.60 and 1.0, with an inlet turbulence intensity of 16% and 12% for the vane and blade cascade respectively. Transient infrared (IR) thermography technique and surface pressure measurement were used to map out the surface heat transfer coefficient and aerodynamic characteristics. The experiments were complemented with computational modeling using the commercial RANS equation solver ANSYS Fluent. The CFD results provided further insight into the local flow characteristics in order to elucidate the flow physics which govern the measured heat transfer characteristics. The results reveal that the highest heat transfer exists in regions with local flow reattachment and new-boundary layer formation. Conversely, the lowest heat transfer occurs in regions with boundary layer thickening and separation/lift-off flow. However, boundary layer separation results in additional secondary flow vortices, such as the squealer cavity vortices and endwall auxiliary vortex system, which significantly increase the stage aerodynamic losses. Furthermore, these vortices result in a low film-cooling effectiveness as was observed on a squealer tip cavity with purge flow. Finally, the importance of transonic experiments in analyzing the turbine

section heat transfer and flow characteristics was underlined by the significant shock-boundary layer interactions that occur at high exit Mach number conditions.

ACKNOWLEDGEMENTS

I would like to express my heartfelt gratitude to my family Margaret, Ruth, Lestley, Geoffrey and Sanders for their loving support and encouragement. You have always been there for me and I would not be writing this without you. I deeply love you guys and truly appreciate everything you have done for me.

Special thanks to my advisor Dr. Wing F. Ng for giving me the opportunity to work on this research project. Your guidance, motivation and mentorship during the course of my graduate school have helped me to learn and develop as an engineer. I would also like to thank Dr. Srinath Ekkad, Dr. Thomas Diller, Dr. Todd Lowe and Dr. Walter O'Brien for taking time to be part of my research committee. Your insightful comments, guidance and discussions on the relevant physics have helped me tackle many of the technical challenges I faced throughout the course of this research.

I would also like to thank my James Philips and David Mayo for the long hours and months they spent assisting me with experiment setup and data collection. To Xue Song, thank you for the many insightful discussions we had regarding heat transfer, film-cooling and data reduction techniques. I would also like to thank Dr. Zhigang Li for his help during some of the experiments and monitoring some of the numerical computations. I am very grateful to the guys at the machine shop, Bill, Johnny, James and Tim for their invaluable advice on parts design and timely completion of the machining and 3D printing tasks. A very special thanks to Diana Israel for her assistance with purchasing and many other logistics related to this research project. Also thanks to Ben and Jamie for their help in resolving a lot of the computer/network systems issues.

Finally, I would like to thank Solar Turbines Inc. for sponsoring this project. I would like to specifically thank Dr. HeeKoo Moon and Dr. Luzeng Zhang for their great ideas, discussions

and challenging questions asked which led to great improvements in the experiment and understanding the data.

ATTRIBUTION

I would like to acknowledge my co-authors Wing F. Ng, James Philips, Xue Song, Hee-Koo Moon, Luzeng Zhang and Zhigang Li. Wing F. Ng is currently a professor at Virginia Tech and was my advisor and also the project supervisor. HeeKoo Moon and Luzeng Zhang were the project point of contact for Solar Turbines Inc. They were involved in the research project planning and provided input on the problem definition/specs. Xue Song and James Philips, who are currently affiliated with Techsburg Inc. and Navigant Inc. respectively, assisted with the experiment data collection for the work presented in Chapter 1 and Chapter 2. David Mayo and Zhigang Li assisted with the experiment data collection and processing, and monitoring the CFD solution process respectively, for the work presented in Chapter 3. David Mayo is a graduate student at Virginia Tech while Zhigang Li was a visiting scholar at the time of the research work.

TABLE OF CONTENTS

LIST OF FIGURES

LIST OF TABLES

PREFACE

The work presented in this dissertation encompasses the heat transfer characteristics under the influence of secondary flows in a gas turbine engine. Three primary secondary flow regions in a gas turbine section – blade tip, near tip, and nozzle endwall – were experimentally and computationally analyzed and the findings presented in a coherent style in three research publications. This research project was sponsored by Solar Turbines Inc. and its author was the lead graduate student researcher in all the work presented herein. The author was involved in all aspects of heat transfer analysis including experiment design, instrumentation, data reduction and analysis with comprehensive literature review. Over the course of this research, the author worked closely with three graduate students - Xue Song, James Philip and David Mayo - and a visiting scholar, Dr. Zhigang Li.

The first two chapters provide a detailed experimental and numerical analysis of the aerothermal characteristics of the turbine blade tip and near-tip regions as influenced by the over-tip leakage secondary flow. Two tip designs were analyzed-flat tip and squealer tip-with the latter having two discrete holes for purge flow and a series of in-cavity ribs. The work presented in the third chapter focuses on understanding the effects of combustor-turbine misalignment; which results in a backward facing step at the turbine inlet, on the endwall secondary flows and heat transfer. All the findings presented herein have been reviewed, presented (or awaiting presentation) at the joint ASME-IGTI conferences in 2014, 2015 and 2016. The research findings from the first two chapters have been published and recommended for publication in the Journal of Turbomachinery. This research work was carried out with the following three main objectives:

I. Closely represent the actual turbine gas path conditions in order to fully capture all the relevant flow physics. This includes the transonic high turbulence and high Reynolds number flow conditions.

II. Accurately measure the relevant aerothermal variables of interest including pressure, heat transfer coefficient and film-cooling effectiveness at the regions of interest under engine representative conditions and configurations.

III. To elucidate the fundamental flow physics governing the observed/measured aerothermal characteristics with the aid of computational fluid dynamics.

The final section of this dissertation contains a series of appendices which provide additional information on other aspects of this research including: test section design, instrumentation, experimental setup, heat transfer and film-cooling data processing technique, uncertainty analysis and computational methods.

BACKGROUND

The turbine section of a gas turbine engine is exposed to extreme gas temperature propagating downstream from the combustors. In order to improve the turbine efficiency, it is often desired to increase the turbine inlet temperature (TIT). For this reason, modern engines have very compact combustors which burn leaner/hotter and result in a radially uniform temperature profile to the turbine inlet. As a consequence, the turbine extremities i.e. the blade tip and endwall, are also exposed to very high heat transfer driving temperature which may exceed the turbine material melting temperature. Therefore, it is paramount that the heat load distribution and flow characteristics are clearly understood and carefully managed in order to prevent thermal damage and subsequent turbine failure.

Understanding the heat transfer and flow characteristics at these turbine extremities poses a common but unique challenge to any turbine designer. In addition to the high temperatures, both the blade tip and endwall are exposed to incoming boundary layer fluid which interacts with the blade/vane potential field and the extremity surface geometry resulting in strong secondary flows. These secondary flows determine the unique heat transfer characteristics on the turbine tip and endwall as well as the turbine stage aerodynamic efficiency/losses. The characteristics of these secondary flows are extremely sensitive to the tip and endwall surface configuration as well as the mainstream gas conditions and any slight changes in these factors may result in drastic changes in the heat transfer characteristics. It is also common for some blade tip designs, such as a shrouded blade tip, to lend strongly into the endwall flow and heat transfer characteristics. Consequently, understanding the flow and heat transfer characteristics for both the turbine blade tip and endwall is a related subject that is relevant to the gas turbine community and has significant implications on the overall turbine stage performance.

CHAPTER 1

Numerical Investigation of Aerothermal Characteristics of the Blade Tip and Near-Tip Regions of a Transonic Turbine Blade

A. Arisi, S. Xue, W. F. Ng
Mechanical Engineering Department
Virginia Polytechnic Institute and State University
Blacksburg, VA 24061

H.K. Moon, L. Zhang
Solar Turbines Inc.
San Diego, CA 92101

ASME-IGTI Paper GT2014-25492

Published in the Journal of Turbomachinery

ABSTRACT

In modern gas turbine engines, the blade tips and near-tip regions are exposed to high thermal loads caused by the tip leakage flow. The rotor blades are therefore carefully designed to achieve optimum work extraction at engine design conditions without failure. However, very often gas turbine engines operate outside these design conditions which might result in sudden rotor blade failure. Therefore, it is critical that the effect of such off-design turbine blade operation be understood to minimize the risk of failure and optimize rotor blade tip performance. In this study, the effect of varying the exit Mach number on the tip and near-tip heat transfer characteristics was numerically studied by solving the steady Reynolds Averaged Navier Stokes (RANS) equation. The study was carried out on a highly loaded flat tip rotor blade with 1% tip gap and at exit Mach numbers of M_{exit} = 0.85 (Re_{exit} = 9.75 x 10^5) and M_{exit} = 1.0 (Re_{exit} = 1.15 x 10^6) with high freestream turbulence (Tu = 12%). The exit Reynolds number was based on the rotor axial chord. The numerical results provided detailed insight into the flow structure and heat transfer distribution on the tip and near-tip surfaces. On the tip surface, the heat transfer

was found to generally increase with exit Mach number due to high turbulence generation in the tip gap and flow reattachment. While increase in exit Mach number generally raises he heat transfer over the whole blade surface, the increase is significantly higher on the near-tip surfaces affected by leakage vortex. Increase in exit Mach number was found to also induce strong flow relaminarisation on the pressure side near-tip. On the other hand, the size of the suction surface near-tip region affected by leakage vortex was insensitive to changes in exit Mach number but significant increase in local heat transfer was noted in this region.

NOMENCLATURE

C	True chord of the blade
C_x	Axial chord of the blade
HTC	Heat Transfer Coefficient
M	Mach number
M_{exit}	Exit Mach number
P_o	Total pressure
q	Surface heat flux
Re	Reynolds number (Based on axial chord)
Re_{exit}	Exit Reynolds number
s	Blade surface distance from leading edge
T	Temperature
T_o	Total temperature
T_{aw}	Adiabatic wall temperature
T_w	Wall temperature
TFG	Thin film gage

TG Tip gap

TLC Transient liquid crystal

Tu Streamwise turbulence intensity

x Axial distance

μ Laminar Viscosity

μ_t Turbulent viscosity

INTRODUCTION

The design of highly efficient gas turbine engines requires careful consideration of the aerodynamics, heat transfer and mechanical strength of the engine material. This is especially true in the turbine section where engine components are subjected to high thermal and mechanical loads. To increase the efficiency of any gas turbine engine, high inlet temperature is desired in the turbine section. Unfortunately, high temperatures compromise the integrity of the blade material which ultimately results in failure. This is particularly true for the blade tip and near-tip region which is one of the most susceptible areas to thermal failure.

In gas turbine engines, leakage flow is important in determining the performance of the rotor blade. Not only does leakage flow represent aerodynamic losses in the turbine section, but is also a cause of very high heat transfer rates on the rotor. This is because leakage flow is characterized by very thin thermal boundary layer in the narrow tip gap which results in very high heat transfer rates. Degradation of the blade tip accounts for approximately one third of high pressure turbine failures [1]. Heat transfer is further increased by the fact that these regions operate in a transitional flow regime experiencing extreme thermal-fluid conditions [2]. Such challenges have necessitated sustained research in the aero-thermal characteristics of the rotor tip and near-tip through experimental and numerical studies.

Early work on the rotor blade heat transfer was carried out by Mayle and Metzger [3]. Their study showed that the pressure difference between the suction and pressure sides is the dominating factor in tip leakage flow and therefore the effects of relative motion of the rotor and shroud on heat transfer are negligible. As a result, numerous successive studies [4-15] on turbine blade tip aerodynamics and heat transfer have been carried out in stationary cascades on various aspects of design, tip configuration and engine operating conditions.

The aerodynamics of the leakage flow around the tip region was studied by Key et al [4] using oil flow visualization and static pressure measurements. The study revealed the key flow features in leakage flow such as pressure side separation vortex and impingement flow on the tip surface near the leading edge and on the suction surface near-tip. The study further showed that leakage flow is responsible for loading of the rear portion of the rotor. A preceding study by Moore and Tilton [5] also confirms the above observations and the authors had observed evidence of formation of a vena contracta at the gap entrance and uniform pressure distribution due to mixing near the gap exit. Heat transfer studies documented in open literature have shown a strong relation with this documented aerodynamics.

Bunker et al. [6] studied the general heat transfer distribution on a flat tip rotor using hue detection based on transient liquid crystal technique. The tip surface heat transfer was characterized by a low heat transfer central “sweet spot” near the leading edge and a high heat transfer region along the pressure side edge caused by reattaching flow. It was also observed that the heat transfer characteristic was similar to that of entry flow into a sudden contraction. Similar studies have been performed to study the effect of varying the tip clearance size. Such conditions may arise from tip material loss caused by rubbing against the turbine casing. Azad et al. [7] observed that changing the tip clearance size alters the leakage flow path with diminishing

clearance shifting the flow towards the leading edge suction side. A study by Zhang et al. [8] revealed that heat transfer on the frontal tip surface region is dominated by thermal diffusion which decreases as the tip gap increases. These studies [7-12], carried out at different tip clearances, have shown a consistent trend of generally increasing rotor tip heat transfer with tip gap size.

The tip surface heat transfer also depends on the tip geometry. Many tip geometries are used in the turbine section to diminish leakage flow losses and tip heat load. Jian-Jun et al. [13] and Kwak et al. [14] used numerical and experimental methods respectively to compare heat transfer on a flat tip to a squealer tip. Their studies revealed that the squealer tip reduced the average tip heat transfer and leakage flow. However, the heat transfer levels on the squealer rim were comparable to that on the flat tip geometry.

Wheeler et al. [15] investigated tip heat transfer in low and high speed flows. A 60% tip heat load reduction was noted when the exit Mach number was increased from 0.1 to 0.98. This was due to reduction in driver temperature. The authors observed that low speed flows are dominated by turbulent dissipation compared to high speed flows.

The effect of turbulence on tip heat transfer has also been documented in open literature. Using a simplified blade model, Wheeler and Sandberg [16] investigated the effect turbulence intensity has on tip heat transfer. Their study found that turbulence intensities greater than 10% significantly augments tip surface heat transfer. Similarly, Zhang et al. [17] found that turbulence intensities below 9% have no noticeable effect on the tip heat transfer for flat tipped turbine blades.

Preceding heat transfer studies were carried out under steady flow conditions. However, it is important to appreciate that in actual gas turbine engines, the flow is highly unsteady. Atkins

et al. [18] studied the effect of such unsteadiness on tip heat transfer in a rotating rig. The study found that the occurrence of tip surface heat flux fluctuations is caused by changes in the local driving temperature. As a result, the tip surface heat transfer coefficient undergoes periodic fluctuation. Their observations complimented the numerical results detailed by Jun Li et al. [19] that unsteady flow conditions results in a periodic fluctuation of tip heat transfer levels.

Even though there have been extensive studies on the rotor tip heat transfer, there are relatively limited reported studies on the near-tip surface heat transfer. Early work by Metzger and Rued [20, 21] used sink and source flow models in a flow channel to analyze the effect of leakage flow on the pressure and suction near-tip. Jin and Goldstein [22] further explored the near-tip mass transfer using naphthalene sublimation technique with different tip clearances, turbulence intensity and exit Reynolds number. Kwak et al. [23] used transient liquid crystal technique to experimentally resolve the spatial near-tip heat transfer coefficient distribution for rotor blades with different tip geometries at tip clearances of 1.0%, 1.5% and 2.5%. The authors found that the heat transfer on the pressure surface was laterally uniform except very close to the tip region and was generally unaffected by the tip clearance size. The region affected by the leakage flow on the suction surface was as large as 20% of the blade span. Zhang et al. [8] spatially resolved the near-tip surface heat transfer coefficient distribution for blades with tip clearances of 0.5%, 1.0% and 1.5%. The results showed a streamwise increase in Nusselt numbers on the suction surface near-tip.

From the preceding literature review, it is clear that few studies have been carried out to investigate the effect of exit flow Mach/Reynolds number on tip and near-tip aerothermal characteristics. However, these studies have involved comparisons to low engine speed condition at low turbulence intensities. Such conditions, however, are not true representations of real gas

turbine engines which operate in a wide range of transonic engine speeds and high freestream turbulence intensities. The present study aims to address this by focusing on heat transfer on the tip and near-tip surfaces of a transonic rotor blade at high freestream turbulence intensity of 12%. This is representative of land based gas turbine engine conditions. The paper presents new numerical information on the effect of varying the exit Mach/Reynolds number within the transonic range on near-tip flow aerodynamics and heat transfer. Tip and near-tip heat transfer characteristics was studied at exit flow speed of Mach 0.85 (design condition) and Mach 1.0. Aerodynamic and heat transfer data at these exit conditions are discussed in detail and conclusions drawn as to the effect of exit flow Mach/Reynolds number.

COMPUTATIONAL METHOD

Solver and Turbulence Models

In this study, the Reynolds-Averaged Navier Stokes Equations were solved using the commercial CFD solver ANSYS *Fluent 14.5*. A pressure-based steady-state solver was used. The Transition-SST model, based on Wilcox k-omega model [24], was used with a wall integration approach to resolve the viscous sub-layer. Therefore, no wall functions were employed. Compressibility effects, curvature correction and viscous heating effects were accounted for in the model. Air was used as the working fluid and was modelled as an ideal gas. The SIMPLE turbulence algorithm was used and a second order or higher upwind advection scheme applied to solve the flow variables.

Computational Domain

Figure 1.1 shows the computational domain and a section of the tip and near-tip surface mesh. A multi-block structured grid was generated using the commercial meshing software *Pointwise v.17*. A total of 8.0 million cells were used to resolve the domain with the maximum y+ values

on the tip and near-tip surfaces being 0.7 and that on the shroud approximately y+ < 5.0. Thirty five cells were employed across the tip gap. This ensured that the flow around the rotor blade was effectively resolved.

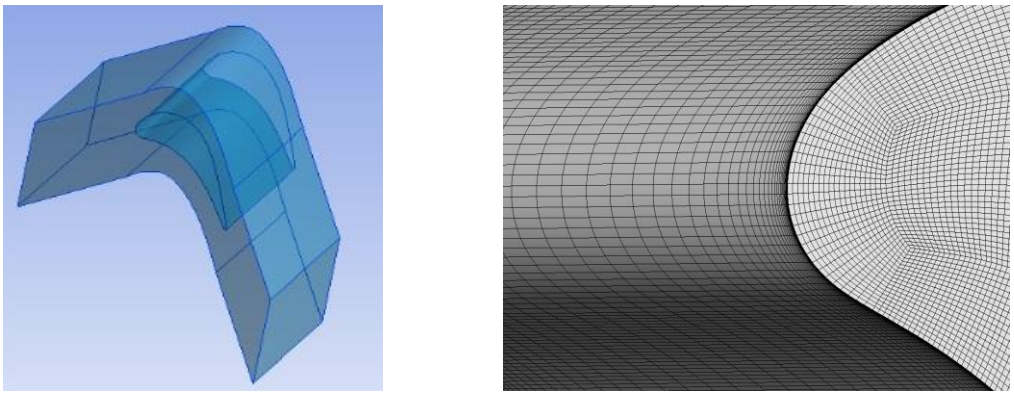

Figure 1.1: Numerical computation domain (left) and a section of the tip and near-tip surface mesh (right)

To minimize computational costs, only one pitch-wise blade passage was modeled with periodic boundary conditions applied to the top and bottom interfaces. The domain inlet and outlet were located 1-Chord upstream and downstream of the rotor leading edge and trailing edge respectively. The inlet total and exit static pressures were then applied at the pressure inlet and pressure outlet boundaries respectively. A uniform total inlet temperature of 400 ^{o}K was also specified at the domain inlet with a turbulence intensity of 12%. At the domain outlet, ambient temperature (300 ^{o}K) and pressure was specified. The remainder of the domain boundaries was designated as no slip walls with a specified thermal heat flux boundary condition. Further details of the cascade and blade properties are summarized in Table 1.1. The convergence of the numerical solution was determined by monitoring the residuals, blade loading and exit flow Mach number. The residuals were ensured to be less than 1×10^{-4}.

Table 1.1	Blade Cascade Properties
Blade Turn Angle	*107.5°*
Blade Span	*0.0762 m*
Axial Chord	*0.0352 m*
Blade True Chord	*0.0699 m*
Pitch	*0.0582 m*
Tip Gap Size	*1% & 2% of engine span*

Grid Dependency Study

To preclude the effects of mesh resolution on the numerical heat transfer results, a grid study was also conducted. The grid was refined until further refinement resulted in less than 1% variation in tip surface heat transfer coefficients with no changes in local heat transfer coefficient distribution. This way, the numerical results obtained were independent of the grid resolution. A summary of the grid study results is outlined in Table 1.2.

Table 1.2 Grid Dependency Study

Mesh	Cell Density	Average Tip HTC [W/m^2 K]
A	5.5×10^6	986.7
B	8.0×10^6	999.7
C	12.1×10^6	1001.7

Heat Transfer Prediction Methodology

The heat transfer coefficient was determined using a two simulation technique. This technique involves executing a first simulation with adiabatic wall conditions at the surfaces of interest. This way, the adiabatic wall temperature (T_{aw}) is determined. In the second simulation, a uniform wall temperature or surface heat flux was applied. For this study, the second simulation was carried out with a uniform wall heat flux (q) and the corresponding wall temperature (T_w) was found. The heat transfer coefficient was then calculated from Equation 1.1.

$$HTC = \frac{q}{T_{aw} - T_w} \tag{1.1}$$

Experiment Data

It is important at this point to summarize the key details of the experimental data used to validate the results of this numerical study. These experiments were carried out at the Virginia Tech Transonic tunnel, which is a blow-down facility with a linear cascade, where both the exit Mach number and Reynolds number are coupled. However, the authors would like to reiterate that this paper is based on a numerical study and experimental data has been used for validation purposes only.

The experimental data was collected on the same blade geometry used in this numerical study. The midspan distribution of heat transfer coefficient has been documented by Nasir et al. [25]. These measurements were made at M_{exit} = 0.78. The near-tip heat transfer measurements were carried out by Anto et al. [26]. Both of these studies used thin film gages for surface heat transfer measurements and the results have been published in open literature.

The authors of this study duplicated the work of Anto et al. [26] to obtain tip surface experiment data. The test setup and data reduction technique was the same as that reported by Anto et al. [26]. However, the authors of this study used a tip surface polycarbonate with a much lower thermal conductivity than the Macor material used by Anto et al. [26]. The technique used to obtain this experimental data is based on the assumption of 1-D heat conduction in a semi-infinite material. For this reason, experiment data near the rotor trailing edge and the near-edge tip surface where 2-D conduction is dominant is unreliable. However, the 2-D edge effects are less than in the Macor data which was reported by Anto et al. [26]. The overall uncertainty associated with the reported experiment midspan data (Nasir et al. [25]) and near-tip data (Anto

et al. [26]) is +/- 11.0% and +/- 11.5% respectively. Further details on the test setup and data reduction technique can be found in the literature referenced above.

RESULTS AND DISCUSSION

Comparison to Experiment: Midspan

The CFD results for M_{exit} = 0.85 with 1% tip gap is compared with pressure and heat transfer measurements made by Nasir et al. [25] on the same blade. Figure 1.2 shows the isentropic Mach number distribution at the blade midspan. The CFD and experimental data showed good agreement.

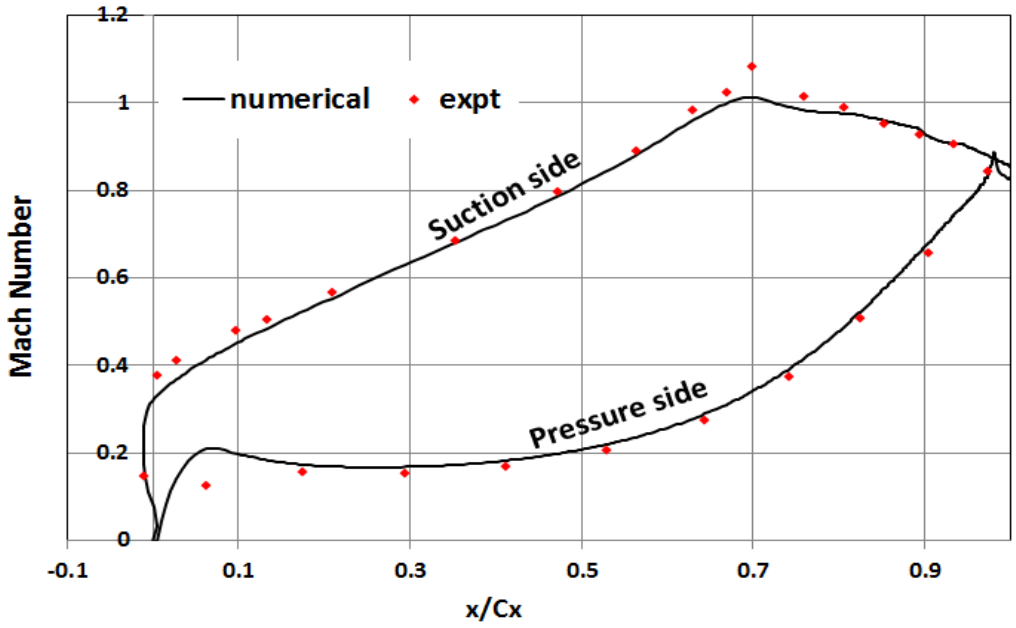

Figure 1.2: Midspan blade loading for M_{exit} = 0.85 with 1% tip gap clearance

Figure 1.3 shows CFD prediction of heat transfer coefficient distribution at midspan. There is a good qualitative agreement between the experiment measurements and the predicted heat transfer coefficient. This is not unexpected because the data measured by Nasir et al. [25] was at a slightly lower exit Mach number of 0.78. Also contributing to the over-prediction is the problem of "stagnation point anomaly" common with eddy-viscosity turbulence models. This over-prediction of surface heat transfer is highest at the blade leading edge and regions with

stagnation flow. Luo et al. [27] observed that this problem amplifies turbulence levels near the leading edge, causing over-prediction of turbulence and heat transfer downstream of the rotor surface.

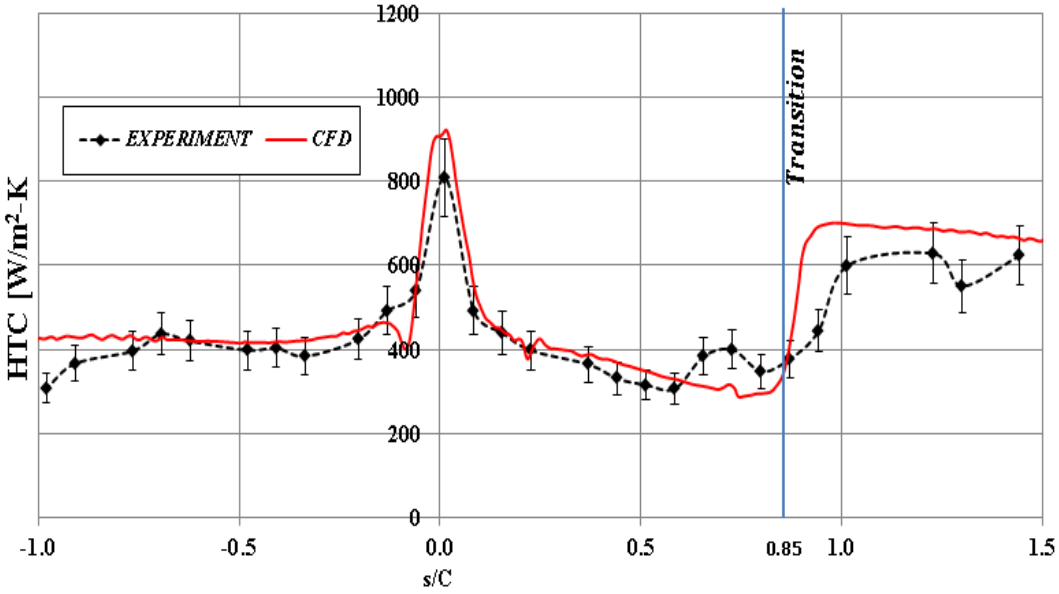

Figure 1.3: Midspan heat transfer coefficient predicted by CFD (M_{exit} = 0.85). Experiment data for M_{exit} = 0.78 reported by Nasir et al. [25].

<u>Comparison to Experiment:</u> Near-Tip

Figure 1.4 shows the heat transfer coefficient distribution at the near-tip (94% span). The qualitative agreement between CFD prediction and experiment is very good, but again over-predicts the heat transfer levels especially on the pressure side. CFD predicts the location of the onset downstream leakage flow at 94% span well but the location of peak HTC due to impingement flow is slightly further downstream for CFD relative to experiment. On the pressure side, CFD predicts the decreasing heat transfer trend. The red colored region of the Figure signifies the leakage affected region on the suction near-tip at 94% span.

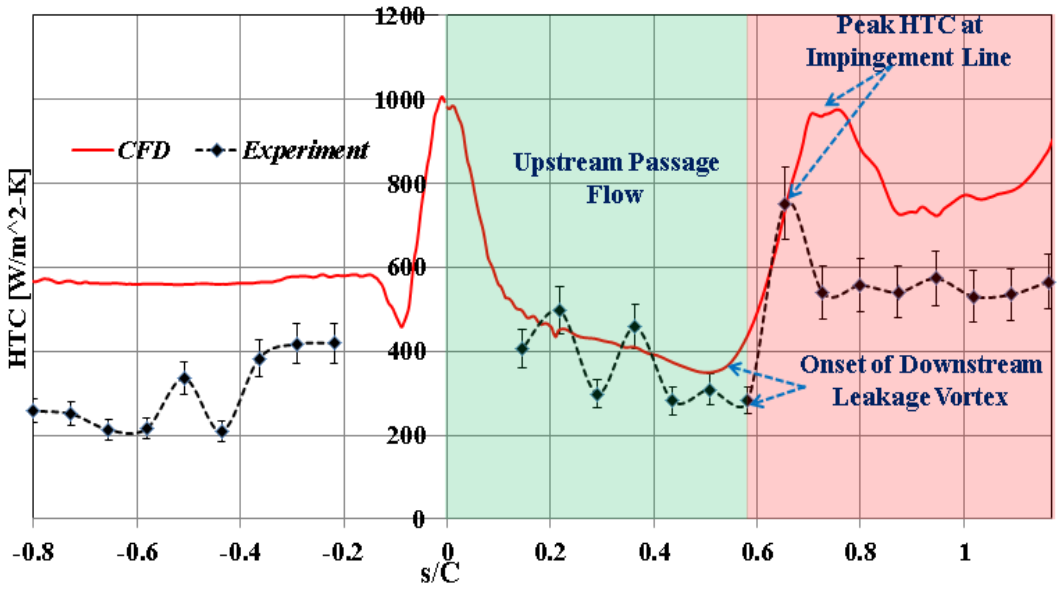

Figure 1.4: Near-tip (94% span) heat transfer coefficient distribution predicted by CFD and experiment data measured by Anto et al. [26] (M_{exit} = 0.85, 1% tip gap)

Heat transfer over-prediction at stagnation points can be resolved by using turbulence models incorporated with production limiters such as standard k-omega and k-epsilon models. Better still, heat transfer over-prediction on the blade surface can be avoided by using Reynolds Stress Models. However, such turbulence models are computationally expensive and highly unstable. In this study, the Transition-SST model was chosen as it showed better accuracy in modeling the heat transfer trends on both the tip and also blade pressure and suction surface where transitional flow is dominant.

<u>Comparison to Experiment:</u> Tip Surface

On the tip surface, CFD was able to predict the heat transfer levels with relative accuracy as shown in Figure 1.5. Good agreement with experiment measurements was noted albeit with slight over-prediction in some regions. S-A and SST k-omega models were also tried but no significant improvement in tip HTC prediction was seen. The experiment does not show the stripe of high heat transfer along the pressure side edge towards the trailing edge seen in the CFD results.

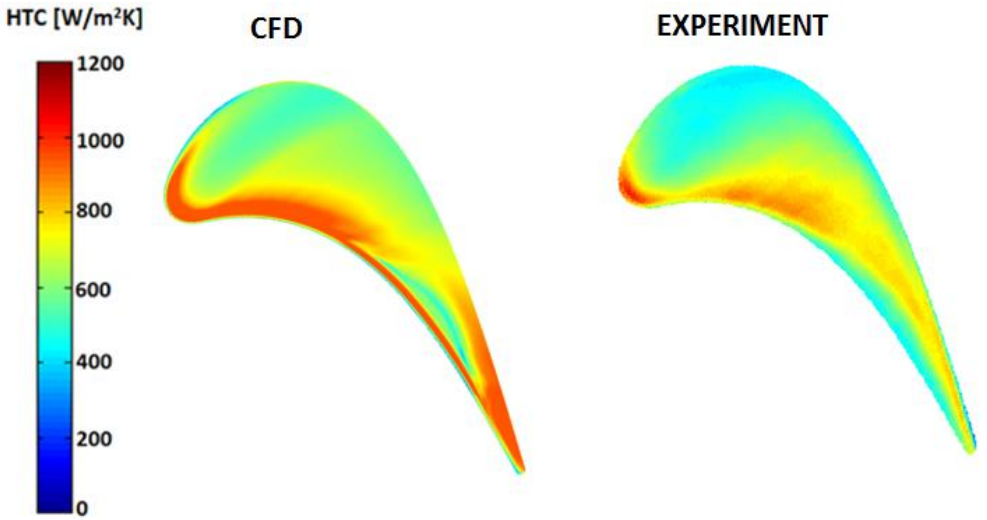

Figure 1.5: CFD and experiment tip heat transfer coefficient distribution at M_{exit} = 0.85 with 1% tip gap clearance

Aerodynamics Overview

The flow around the turbine blade tip is critical in understanding the heat transfer results. Figure 1.6 shows the overtip flow Mach number for M_{exit} = 0.85 at 1% tip gap size. Figure 1.6a shows the leakage flow Mach number distribution for 0 < M < 1.5. Figure 1.6b only shows only the leakage flow in the supersonic range (1.0 < M < 1.5). The tip surface has been marked into regions A, B and C for purposes of discussion.

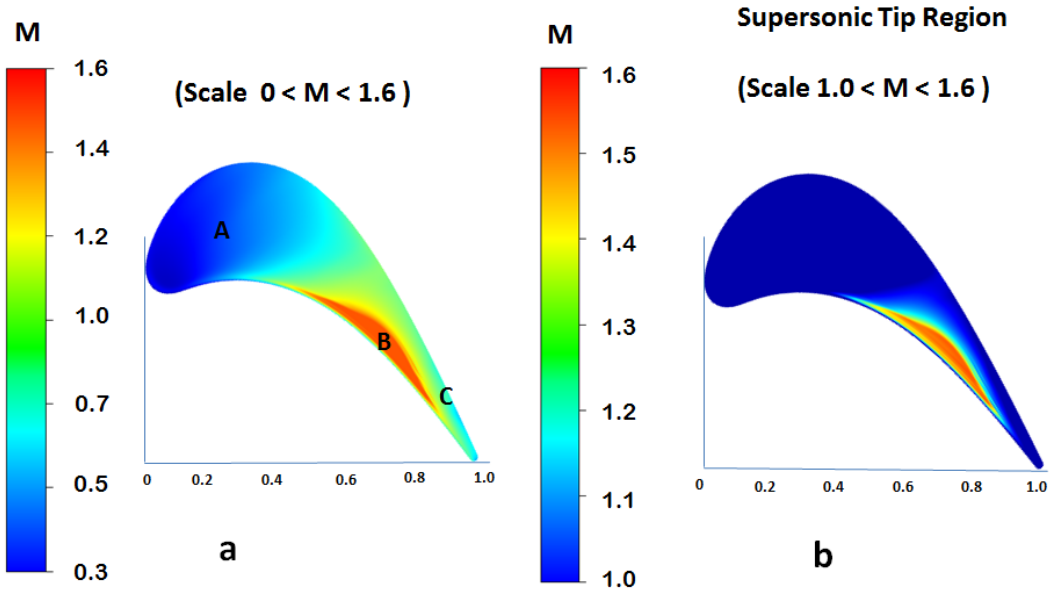

Figure 1.6: Over tip flow Mach number for M_{exit} = 0.85 taken at the mid-plane of the tip gap (CFD). Note the Mach number contour scale difference between Figure 1.6a and Figure 1.6b

Tip Surface Flow

From Figure 1.6, it can be seen that flow over the tip surface ranges from low subsonic flow of $M \sim 0.3$, to supersonic flow of with $M \sim 1.47$. Subsonic flow dominates the near-leading edge regions (Region A) and near the trailing edge towards the suction surface (Region C). The downstream portion of the tip surface near the pressure side edge, towards the trailing edge (Region B), has sonic and supersonic flow. Figure 1.6 shows that the peak leakage flow speed is along the pressure side edge, between $x/C_x = 0.7$ and $x/C_x = 0.9$. This flow distribution is better understood from studying the surface flow pattern and near-tip loading.

Figure 1.7 and Figure 1.8 show the surface flow pattern and the blade loading at 94% span respectively. From Figure 1.7, it is observed that flow over tip surface region A in Figure 1.6, originates from around the leading edge and exits the tip gap on the suction side with $x/C_x < 0.4$. The near-tip loading in Figure 1.8 shows that this region has a small pressure differential and therefore the tip surface flow speed is low.

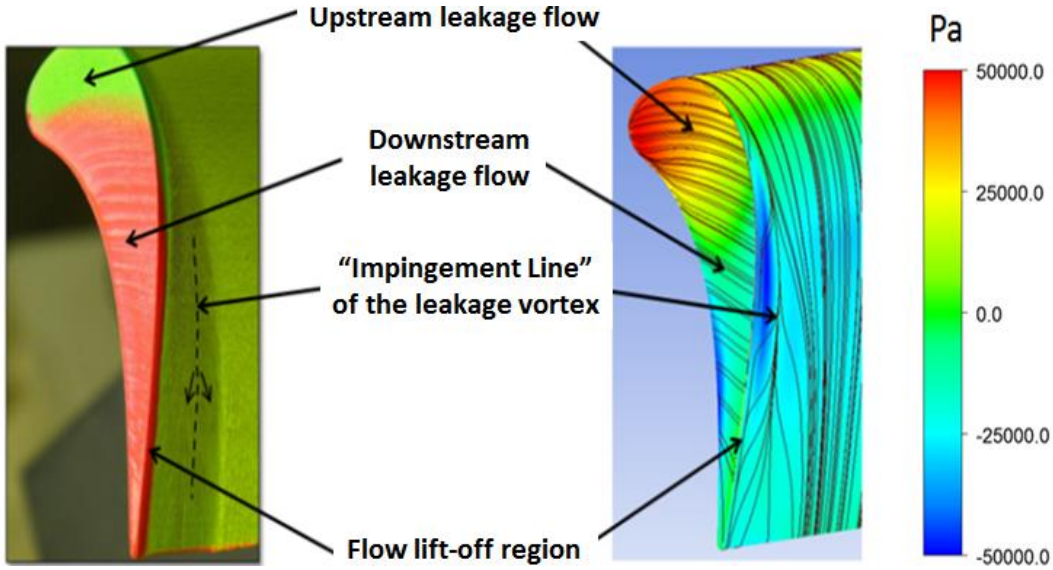

Figure 1.7: Tip and near-tip oil-flow visualization results at $M_{exit} = 0.85$ (left, courtesy of Anto et al. [26]). CFD surface flow streamlines at 0.1 mm above the blade surface with a colormap of local static pressure (right)

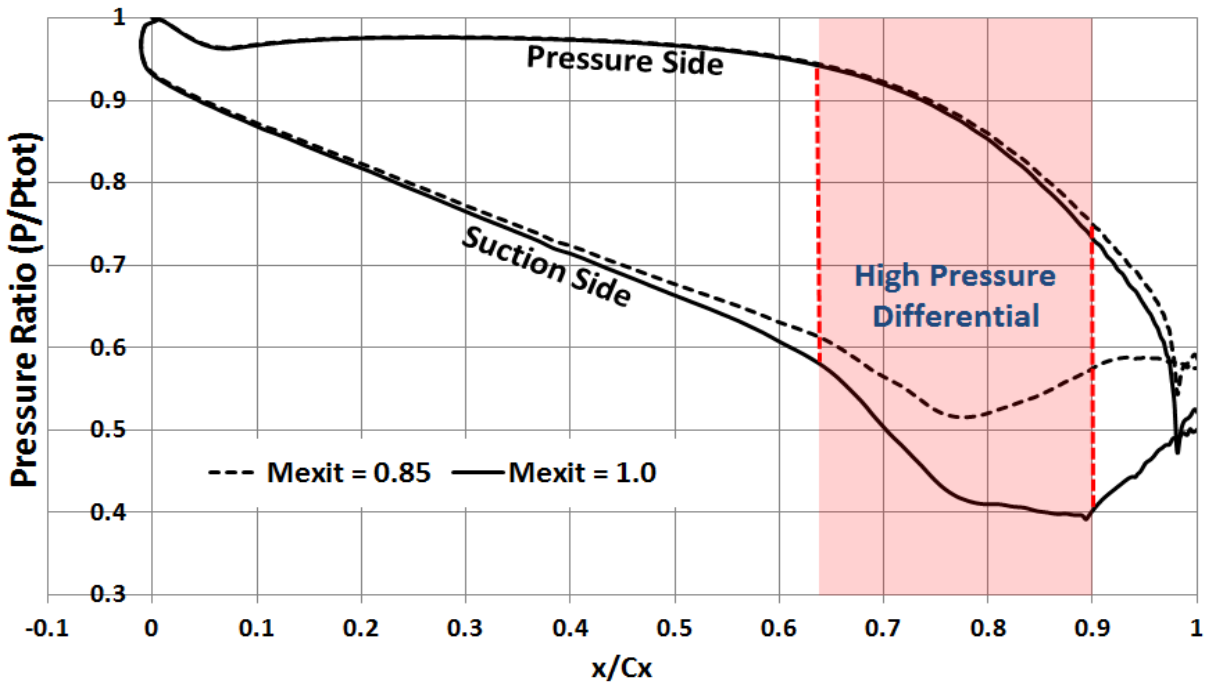

Figure 1.8: Rotor blade loading at 94% span for M_{exit} = 0.85 and M_{exit} = 1.0 (CFD)

High speed tip surface flow, noted in region B, is caused by a combination of high pressure difference between the pressure and suction sides as well as formation of a separation bubble along the pressure side edge. The presence of a separation bubble acts as a restriction at the gap entrance, forcing the flow to accelerate around the separation bubble. This is especially true for sharp edged tip corner radius, where the separation bubble is larger as noted by Ameri et al. [28]. In as much as the separation bubble may lower the mass flow entering the tip gap, the resulting flow acceleration around the bubble may have adverse effects on heat transfer upon reattachment on the tip surface.

Surface streamlines in Figure 1.9 shows high streamline divergence near the leading edge, and along the pressure and suction side edges. Flow entering the tip gap near the leading edge splits and flows briefly either along the suction side or pressure side tip edge as shown by the arrows in Figure 1.9. This is caused by the existence of a favorable pressure gradient along these edges near the leading edge (x/C_x < 0.05, see Figure 1.8). The two flows along the edges

then interact with flow entering the tip gap slightly downstream resulting in the streamline cross-flow. Downstream of x/C_x ~ 0.05, the pressure difference across the tip starts to increase, thereby driving the flow across the tip causing high streamline divergence seen in Figure 1.9a. Figure 1.9b and 1.9c shows the contours of turbulent viscosity in the tip clearance half plane for M_{exit} = 0.85 and M_{exit} = 1.0 respectively. Cross-flow and streamline divergence regions lead to high turbulence generation with increasing Mach number on the frontal part of the tip surface. This increased turbulence generation is marked by an increase in flow turbulent viscosity as seen in the turbulence viscosity contours in Figure 1.9b and Figure 1.9c. This flow characteristic has a significant effect on the tip heat transfer discussed in the latter sections of this paper.

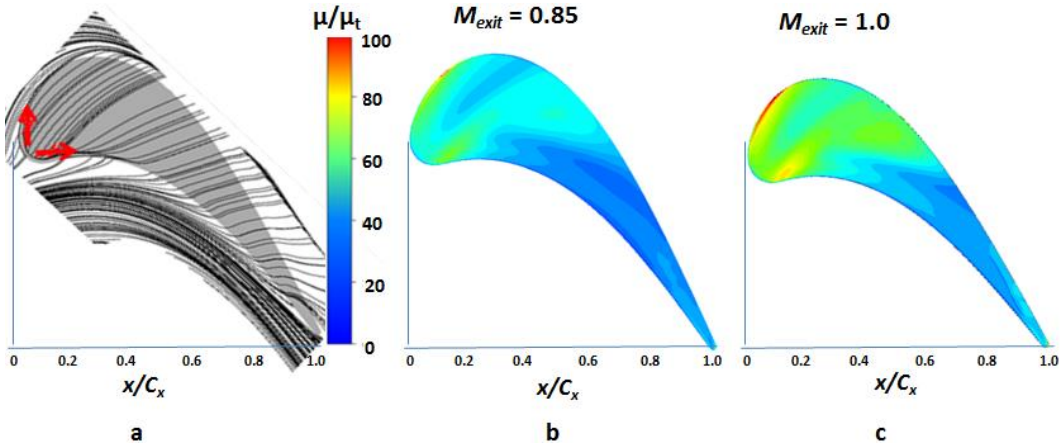

Figure 1.9: a.) CFD prediction of over-tip flow streamlines b.) Surface contours showing turbulent viscosity on the tip clearance half plane for M_{exit} = 0.85 and c.) M_{exit} = 1.0

Effect of Exit Mach/Reynolds Number on Aerodynamics

The flow speed at the tip clearance half plane at M_{exit} = 1.0 is shown in Figure 1.10. Figure 1.10a shows the leakage flow Mach number distribution for 0.3 < M < 1.6. Figure 1.10b only shows only the leakage flow in the supersonic range (1.0 < M < 1.6).

The peak leakage flow speed within the tip gap rises to M~1.6 with ~30% of the tip surface now experiencing supersonic leakage flow. Increasing the exit Mach number significantly increases the leakage flow speed but only on downstream portion of the tip surface

i.e. $x/C_x > 0.5$. The leakage flow upstream of $x/C_x = 0.5$ is relatively unaffected by changes in exit Mach number.

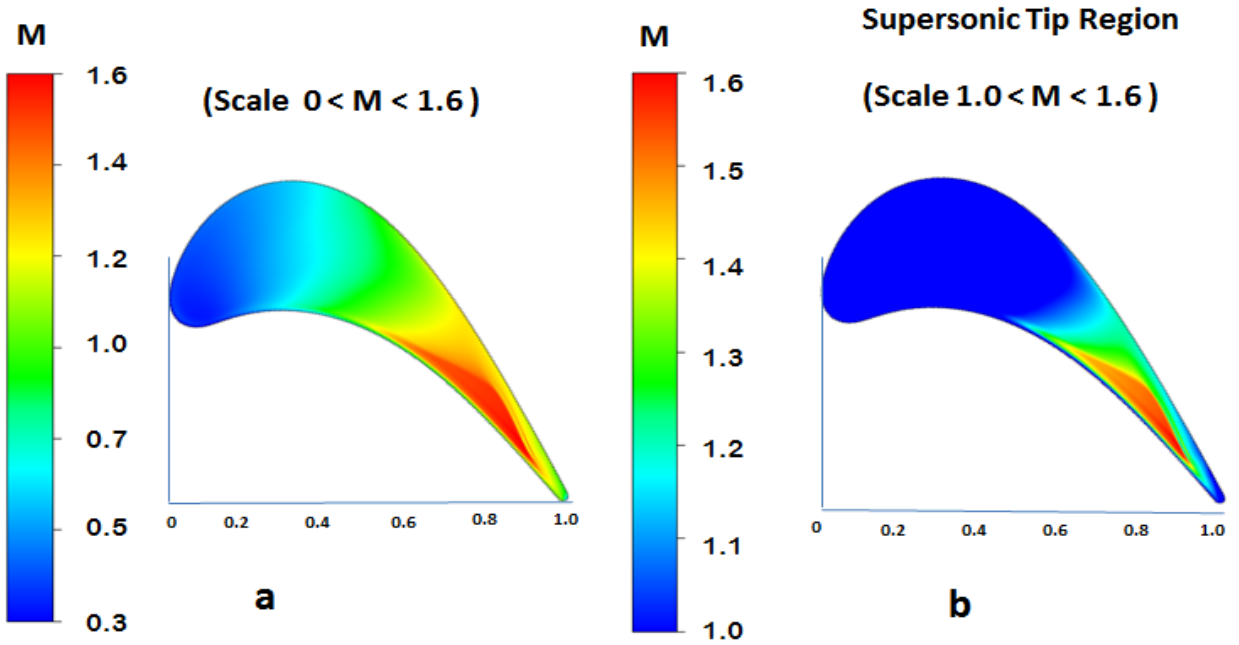

Figure 1.10: CFD Mach number distribution at the tip clearance half plane for M_{exit} = 1.0. Note the Mach number contour scale difference between Figure 1.10a and Figure 1.10b

The supersonic flow region creeps upstream towards the leading edge. The leakage flow downstream of $x/C_x \sim 0.65$ exits the tip gap at supersonic speed. It would be expected that the occurrence of supersonic leakage flow results in formation of shockwaves within the tip gap. This may lead to the possibility of choking occurring at the downstream tip gap clearance.

In general, the flow characteristic on the tip surface is strongly related to the rotor blade loading at the near-tip. Figure 8 shows the blade loading at 94% span for $M_{exit} = 1.0$. Increasing the exit Mach number significantly loads the aft portion of the rotor blade near-tip, between $x/C_x = 0.64$ and $x/C_x = 0.9$. However, this additional loading is a result of change in flow dynamics on only the suction surface. The pressure distribution on the rotor pressure side near-tip is insensitive to changes in exit flow Mach number. Therefore the flow characteristic on the pressure side near-tip surface is a weak function of the exit flow Mach number.

Tip Heat Transfer

Figure 1.11 shows the spatial heat transfer coefficient distribution on the tip surface for M_{exit} = 0.85 and M_{exit} = 1.0 for 1% tip gap. First, a look at tip surface heat transfer with the tip at design configuration (M_{exit} = 0.85). Near the leading edge, high heat transfer is predicted on the tip surface. In the earlier discussion, this region was noted for relatively low speed flow with high cross-flow diffusion and streamline divergence. Streamline cross flow causes turbulence production which is then diffused towards the mid-sections of the tip (Region H). This serves to increase heat transfer on the tip surface near the leading edge. Between the two cross-flows is a region of low leakage mass flow and low heat transfer, popularly referred to as the "sweet spot" (Region G).

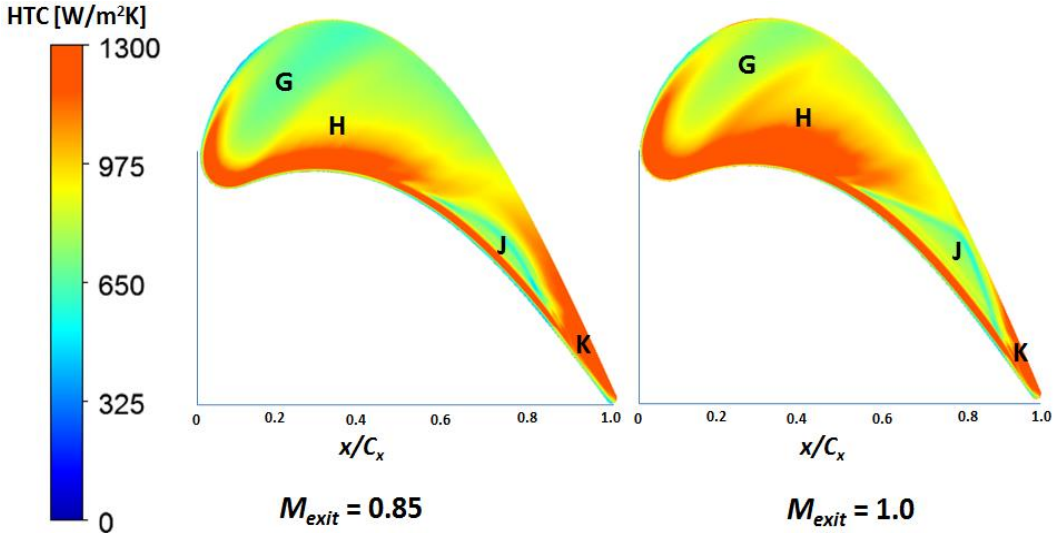

Figure 1.11: Tip surface heat transfer coefficient distribution for M_{exit} = 0.85 and M_{exit} = 1.0 (CFD)

On the pressure side downstream region between 0.65 < x/C_x < 0.85 (Region J), high heat transfer is caused by supersonic flow reattachment. High heat transfer is also observed near the trailing edge, towards the suction side (Region K). This high heat transfer is less pronounced at sonic exit Mach number, but the heat transfer levels are higher. Figure 1.12 shows turbulent viscosity on three planes across the tip gap. The planes are aligned along leakage flow

streamlines entering the tip at pressure side x/C_x = 0.2, x/C_x = 0.5 and x/C_x = 0.8. Turbulence generation, marked by increasing turbulent viscosity, is seen as the leakage flow approaches the gap exit. This turbulence generation should not be confused with that observed along the x/C_x = 0.2 plane, which is due to upstream cross flow discussed earlier.

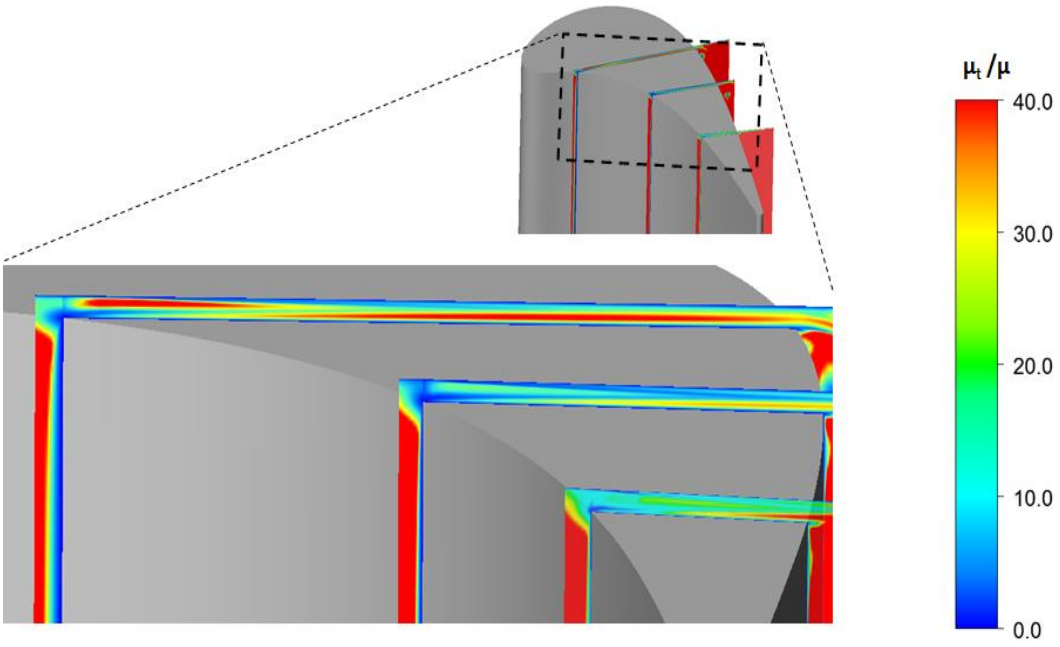

Figure 1.12: Leakage flow turbulent viscosity along flow streamlines from pressure side *x/Cx* = 0.2, *x/Cx* = 0.5 and *x/Cx* = 0.8

Effect of Exit Mach/Reynolds Number on Tip Heat Transfer

When the M_{exit} is increased to 1.0, the heat transfer near the leading edge increased as a result of increased cross-flow diffusion. Consequently, the size of the "sweet spot" decreases. Heat transfer near the pressure side edge, towards the trailing edge, also increases. The size of this heat affected region also increases significantly compared to the case with M_{exit} = 0.85. Figure 1.13 shows the density gradient on a plane across the tip gap near the rotor trailing edge (Region J in Figure 1.11). Spatial tip surface heat transfer distribution within this region is characterized by bands of high and low heat transfer (See Figure 1.13). This is a result of shock/boundary layer interaction on the tip surface by a series of reflecting oblique shocks

propagating from the pressure side entrance. Strong shock interaction is observed near the suction side exit (See Figure 1.13). Beyond this point, a boundary layer appears to develop over the tip and shroud surface. Very weak oblique shocks form between these two boundary layers and the flow exits the tip clearance at supersonic speed.

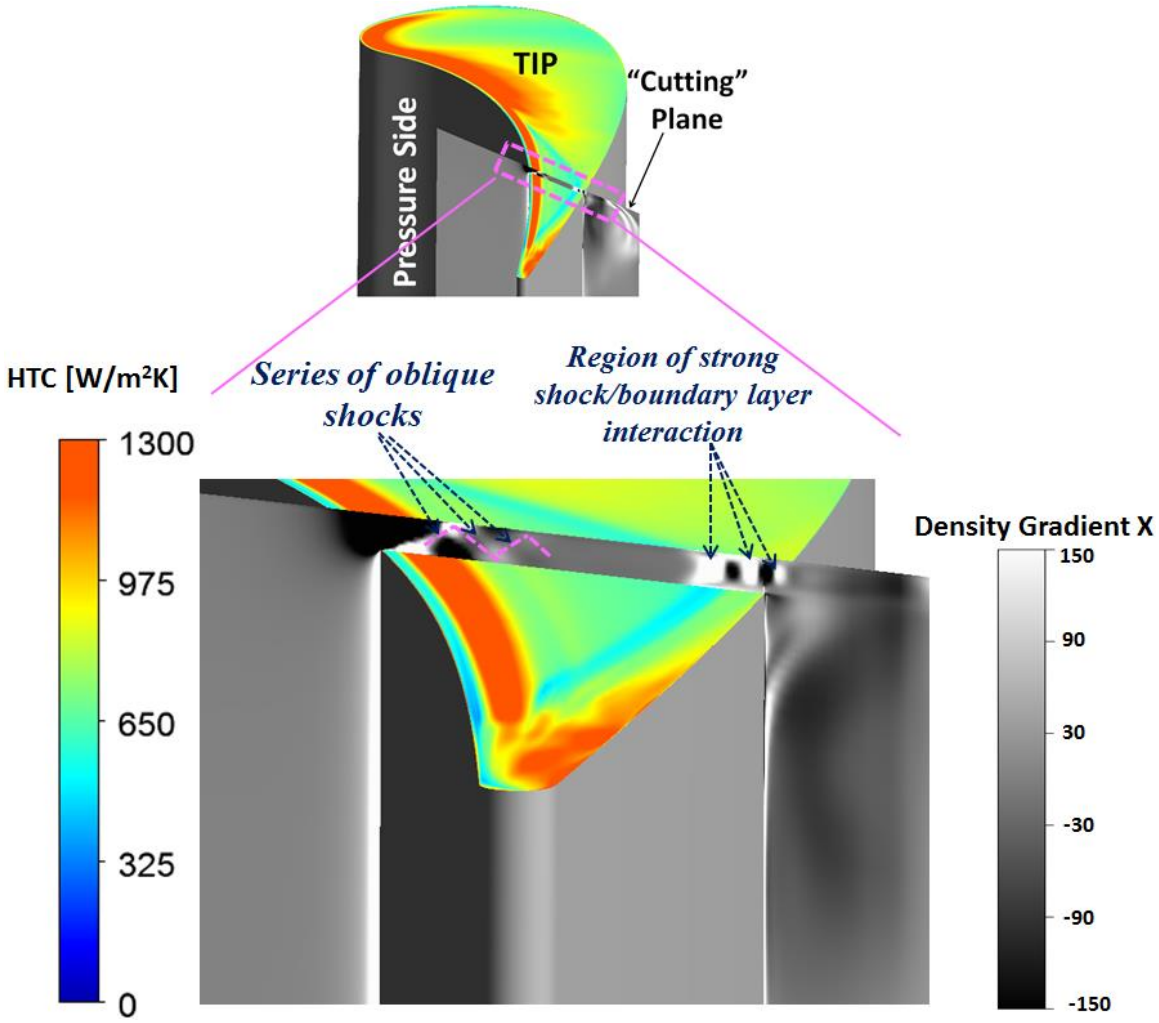

Figure 1.13: Density gradient on a plane across the tip gap showing overtip shocks for M_{exit} = 1.0. (Tip surface contours of heat transfer coefficient)

Effect of Over-tip Shocks on Heat transfer

Illustrated in Figure 1.14 is the formation and propagation of shock waves in the tip gap due to supersonic leakage flow. As the flow accelerates around the pressure side separation bubble (Region A), compression waves result in formation of an oblique shock wave. A local

hot-spot exists within region B due to flow reattachment coupled with entrance effects. The oblique shock wave reflects off the casing then back onto the tip surface causing a localized thickening of the boundary layer just upstream of this incident shock. This results in a low heat transfer band at region C. Subsequent local thinning of the boundary after the shock causes a high heat transfer band (Region D). The bands of high and low heat transfer on the tip surface, shown in Figure 1.13, are a direct result of these interactions. Because the developing boundary layer over the tip surface is thin near the gap entrance, the shock boundary layer interaction is stronger near the pressure side edge and consequently a greater effect on tip heat transfer is observed here. As the boundary layer grows towards the gap exit, the influence of the oblique shocks on tip heat transfer diminishes. Close to the gap exit, the system of reflecting over-tip shocks culminates in a normal shock. Consequently, the resulting strong shock/boundary layer interactions have significant effect on the tip heat transfer.

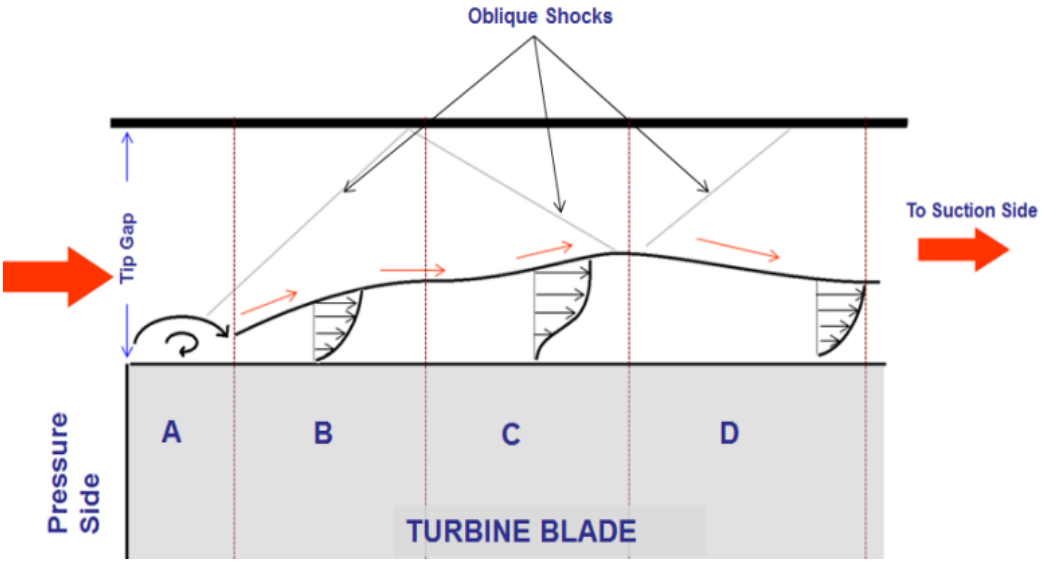

Figure 1.14: Illustration of shock/boundary layer interaction over the blade tip surface

Comparison to Literature and General Remarks

At this point, it is worth comparing these observations to that in open literature. Zhang et al. [29] observed that the flow in the tip gap, over the frontal part of the tip is subsonic. The

authors reported that enhanced cross-flow diffusion is responsible for high heat transfer on this part of the tip surface and the highest tip heat transfer was within this cross-flow region. The current study finds that the high heat transfer rates resulting from supersonic reattachment is comparable to that in the cross-flow region. Anto et al. [26] reported a diminishing 'sweet spot' with increasing exit Mach number. Studies by Zhang et al. [8, 29] and Wheeler et al. [15] have also reported the formation of over-tip shock waves. In their studies, nearly 50% of the tip surface (and much further upstream on the tip surface) was affected by over-tip shocks. However, in this study, over-tip shocks were observed in a much smaller region near the trailing edge. The authors postulate that this difference is a result of the differences in blade loading. Wheeler et al. [15] also reported a normal shock wave in the tip clearance, at the end of the reflecting oblique shocks. The study suggested that the position of the normal shock in the tip clearance is dependent on the width to gap ratio.

Near-Tip Heat Transfer

The spatial distribution of heat transfer coefficient on the rotor near tip surface is shown in Figure 1.15 for M_{exit} = 0.85 and M_{exit} = 1.0. Heat transfer coefficient is relatively uniform across the pressure side near-tip surface. On the suction surface near-tip, high heat transfer levels occur along the path of the leakage vortex. The peak levels of heat transfer occur along the impingement line where the leakage vortex forces hot air onto the blade surface. Increasing the exit Mach/Reynolds number does not appear to have an effect on the size of the heat affected region. However, high exit Mach number increases the peak heat transfer by nearly 30%. This seems to suggest that exit Mach/Reynolds number has little effect on the radial size of the leakage vortex but increases the strength of the leakage vortex significantly.

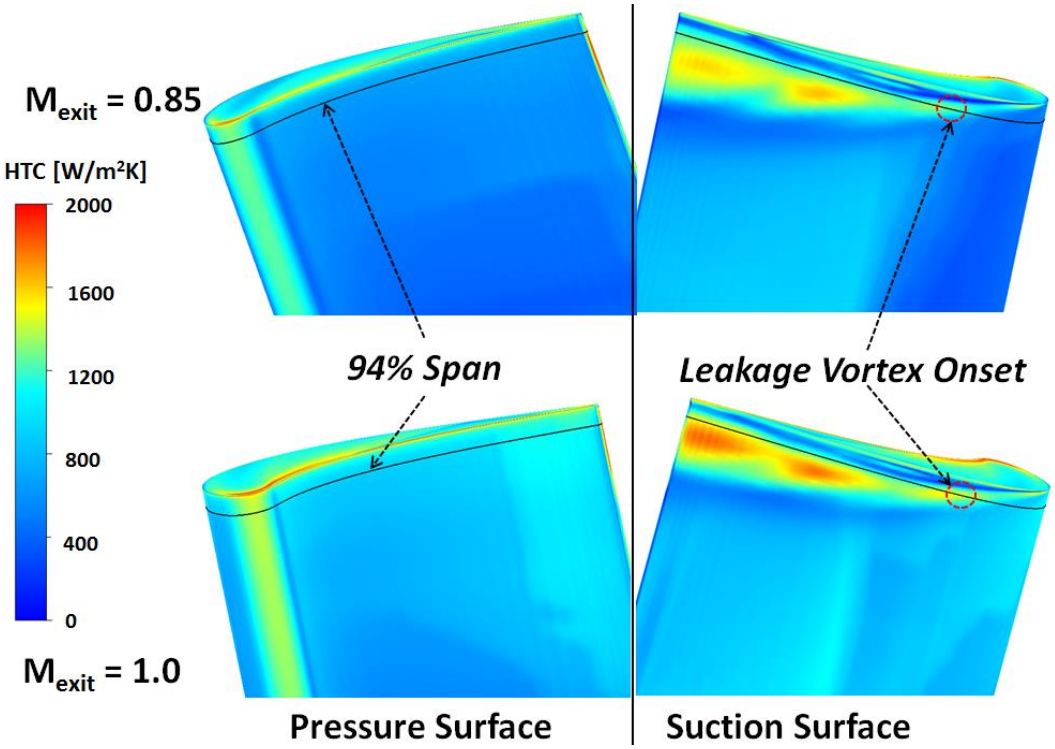

Figure 1.15: CFD prediction of the pressure and suction surface heat transfer coefficient distribution at M_{exit} = 0.85and M_{exit} = 1.0

Figure 1.16 shows the distribution of heat transfer coefficient along the streamwise direction at the blade near-tip (94% span). Heat transfer on the suction surface near-tip decreases downstream from the leading edge up to $s/C \sim 0.55$. At this location, the HTC level begins to rise, marking the onset of the leakage vortex. The onset position of the leakage vortex at 94% span is the same for both exit Mach numbers. This reinforces the conclusion that the radial size of the leakage vortex is unchanged with exit Mach number since a large vortex would shift the onset point upstream.

After the onset point, heat transfer rises steadily to a peak level where it stays high briefly, then drops off towards the trailing edge. This 'saddle' of high heat transfer, as shown in Figure 1.16, is caused by the impingement line moving over the 94% span line where data was collected. Heat transfer level at this point is comparable to that caused by stagnation flow at the rotor leading edge. Furthermore, from this point downstream, heat transfer difference between

the two exit Mach/Reynolds numbers is highest. While increasing the exit Mach number would generally raise the blade surface heat transfer by nearly 25%, the penalty is much more severe within the leakage affected near-tip surface where heat transfer increases by as much as 38%. Such an excessive heat transfer rate is likely to result in a high localized thermal heat load that may eventually facilitate tip failure.

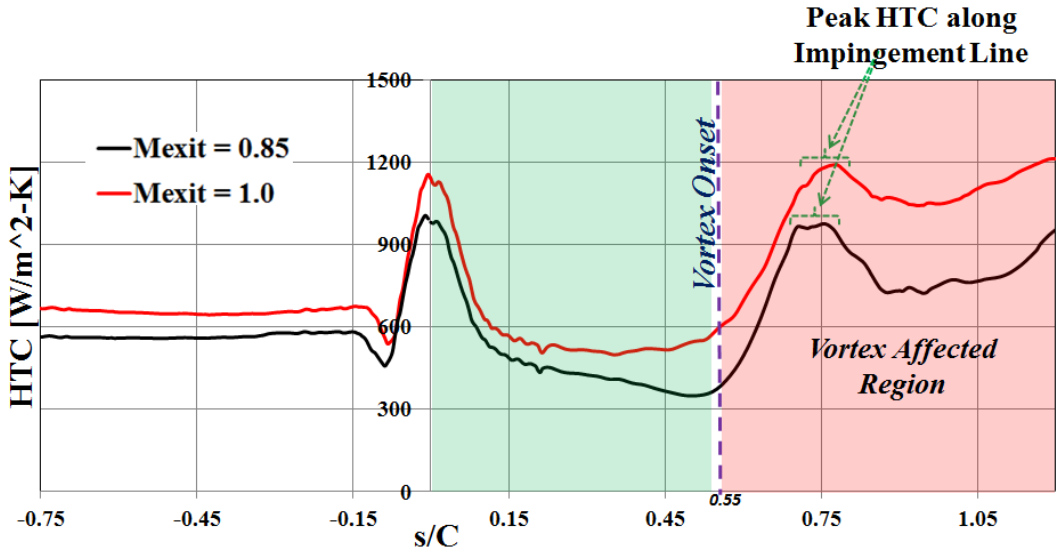

Figure 1.16: Streamwise heat transfer coefficient distribution at 94% span for M_{exit} = 0.85 and M_{exit} = 1.0 (CFD)

Pressure Side Near-Tip Heat Transfer

Figure 1.17 shows the change in flow turbulence and heat transfer coefficient, while approaching the tip from midspan for M_{exit} = 0.85. Generally the flow turbulence and heat transfer increases towards the tip gap. Even though the flow turbulence starts to increase from nearly 70% span, the heat affected pressure side near-tip is restricted to with 10% span from the tip. Heat transfer on the pressure side near-tip is generally laterally uniform from midspan to 90% span.

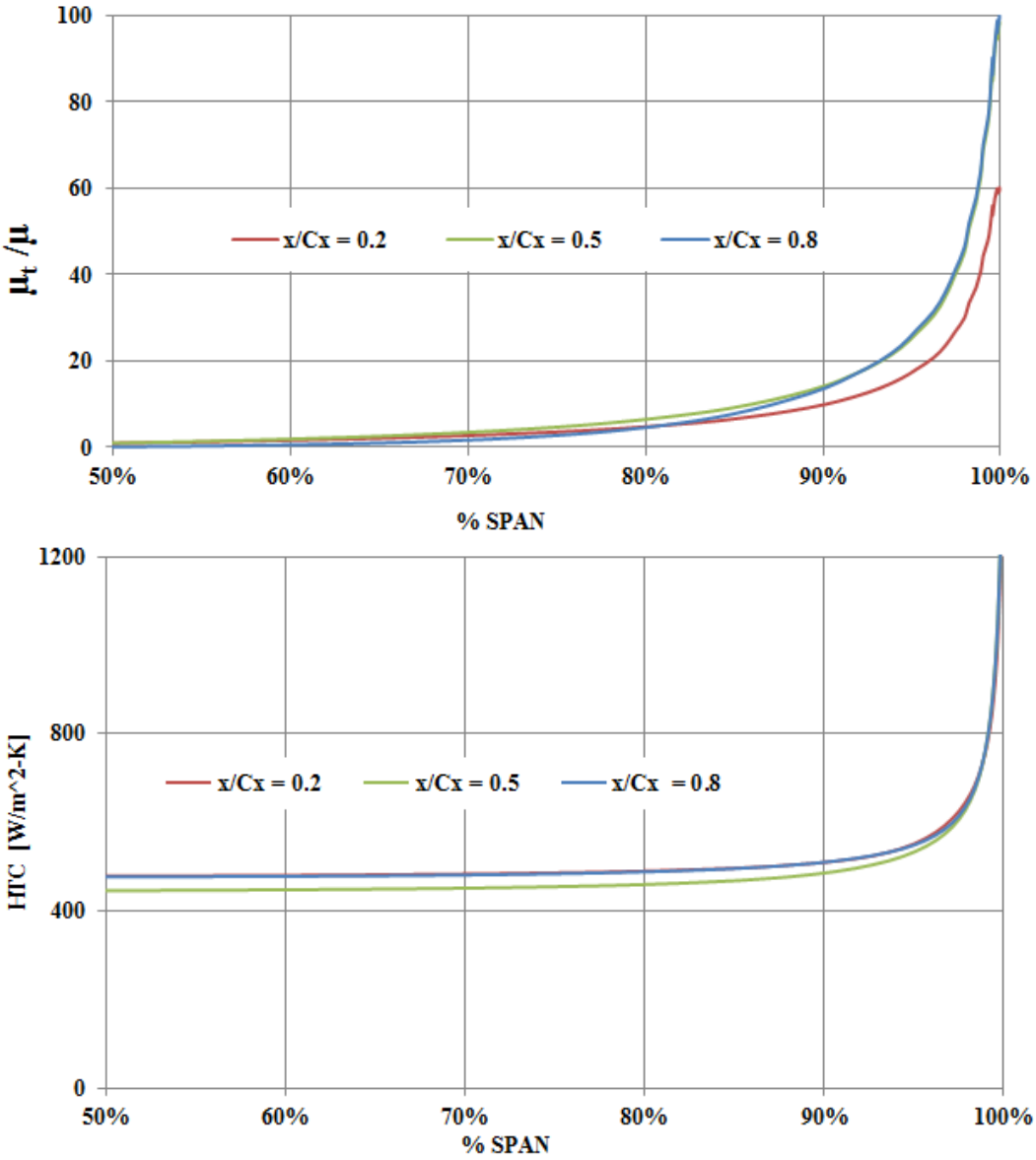

Figure 1.17: Pressure surface spanwise distribution of turbulent viscosity and heat transfer coefficient at x/C_x = 0.2, x/C_x = 0.5, x/C_x = 0.8 for M_{exit} = 0.85 (CFD)

Figure 1.18 shows similar information but for M_{exit} = 1.0. A reverse effect in flow turbulence is predicted i.e. decreasing flow turbulence near the tip gap. The turbulence intensity decreases from 95% span at x/C_x = 0.2 and from 90% at x/C_x = 0.8. This is due to strong flow acceleration into the tip gap, causing the flow to undergo relaminarisation marked by decreasing turbulent viscosity. The acceleration/relaminarisation effect is stronger downstream from x/C_x =

0.5, due to strong pressure differential across the tip gap. The entrance effects are restricted to within ~5% span from the tip, similar to M_{exit} = 0.85.

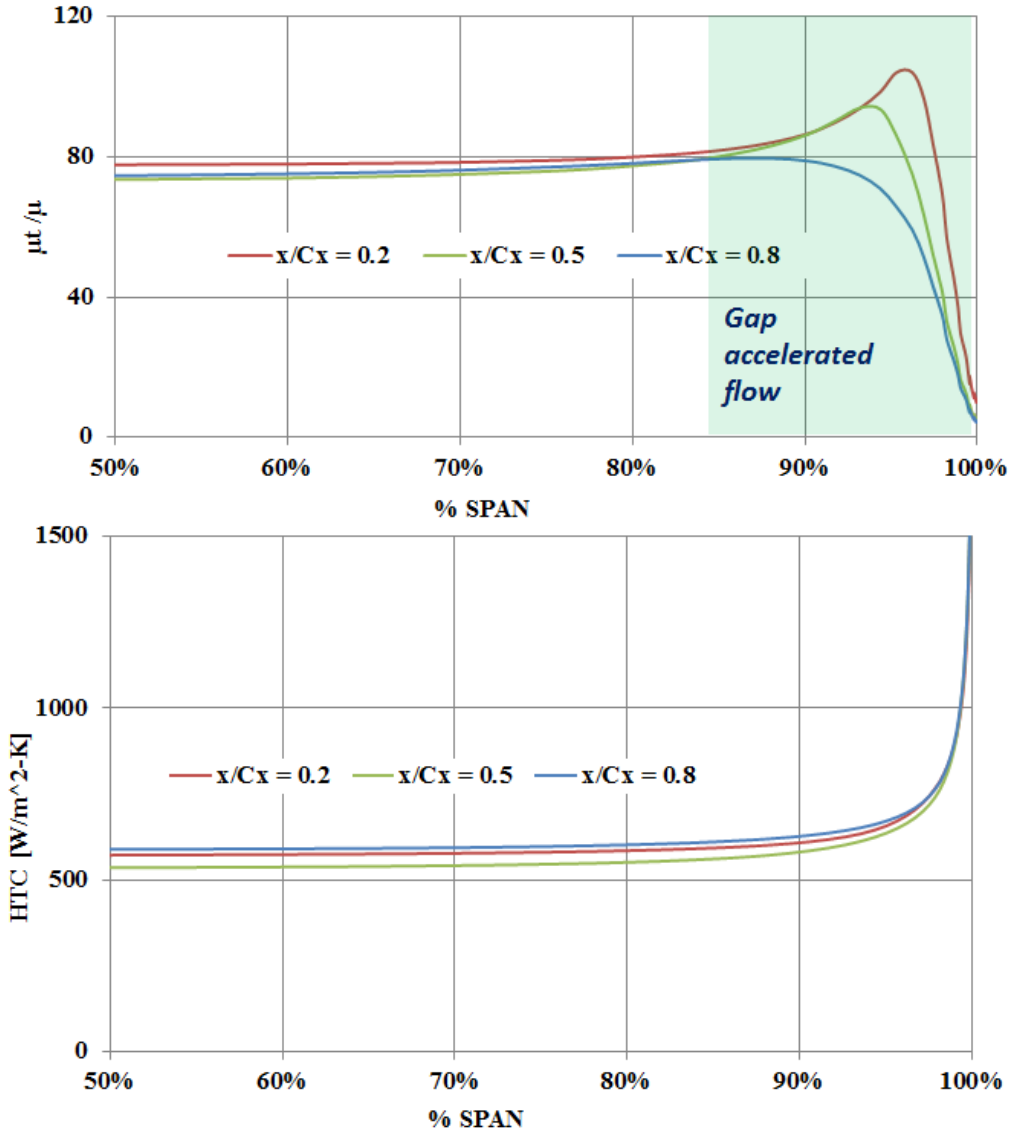

Figure 1.18: Pressure surface spanwise distribution of turbulent viscosity and heat transfer coefficient at x/C_x = 0.2, x/C_x = 0.5, x/C_x = 0.8 for M_{exit} = 1.0 (CFD)

Suction Side Near-Tip Heat Transfer

Figure 1.19 shows the effect of the leakage flow on the suction surface flow turbulence and heat transfer coefficient for M_{exit} = 0.85. The upstream near-tip surface at x/C_x = 0.2 is generally unaffected by leakage flow. This is caused by the fact that the upstream leakage flow is

low subsonic flow and therefore, its interaction with passage flow generates little turbulence. Moving downstream to x/C_x = 0.5 and x/C_x = 0.8, increasing leakage flow exit speed on the suction surface increases turbulence generation on the suction surface near-tip. The turbulence intensity, and therefore heat transfer, is highest within the leakage vortex. From Fig 1.19, the leakage vortex increases the near-tip surface heat transfer as far as ~17% span from the tip (for x/C_x = 0.80).

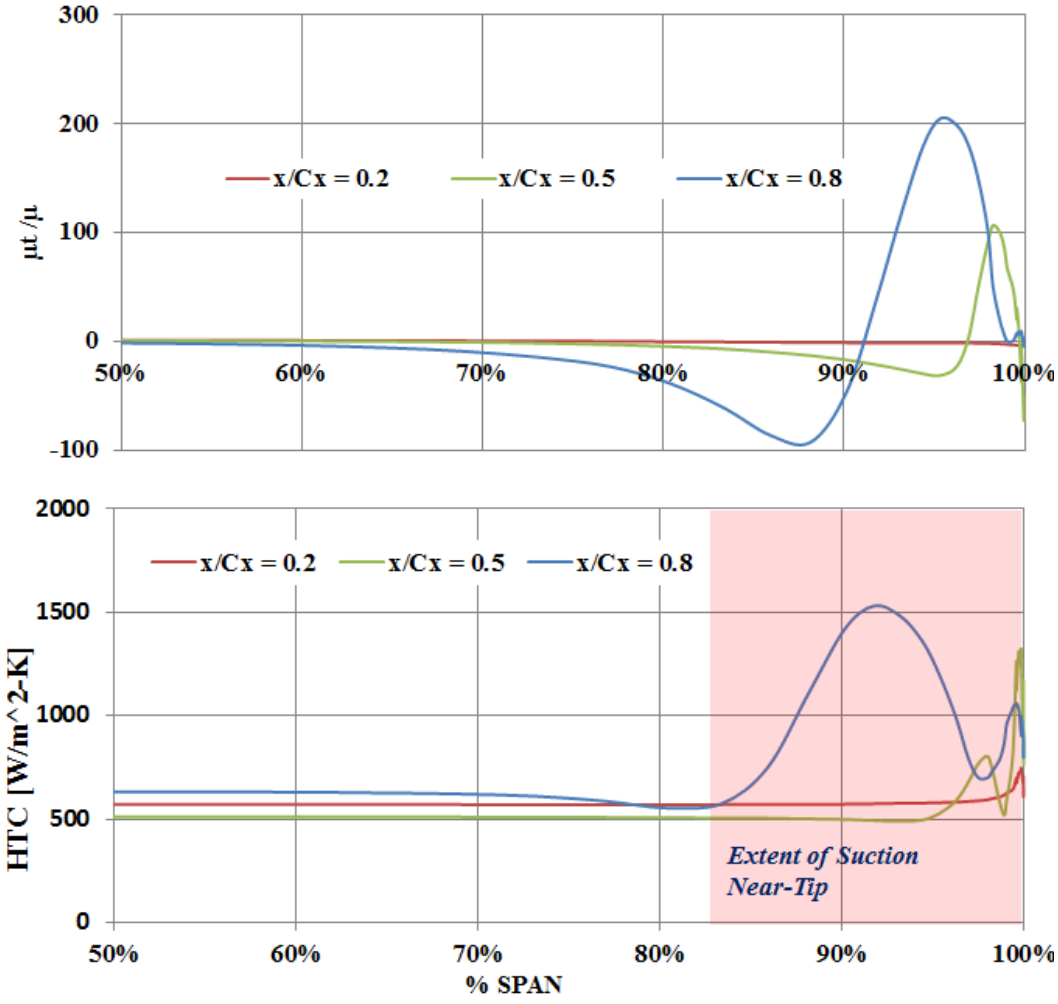

Figure 1.19: Suction surface spanwise distribution of turbulent viscosity and heat transfer coefficient at x/C_x = 0.2, x/C_x = 0.5, x/C_x = 0.8 for M_{exit} = 0.85 (CFD)

Figure 1.20 shows surface heat transfer coefficient distribution for M_{exit} = 1.0. It is interesting to note that the furthest extent of the leakage vortex is same as that for M_{exit} = 0.85

(shown in Figure 1.19). This is because the size of the leakage vortex is insensitive to the flow exit Mach/Reynolds number. However, the increasing strength of the leakage vortex with exit Mach/Reynolds number causes the peak heat transfer within this region to increase.

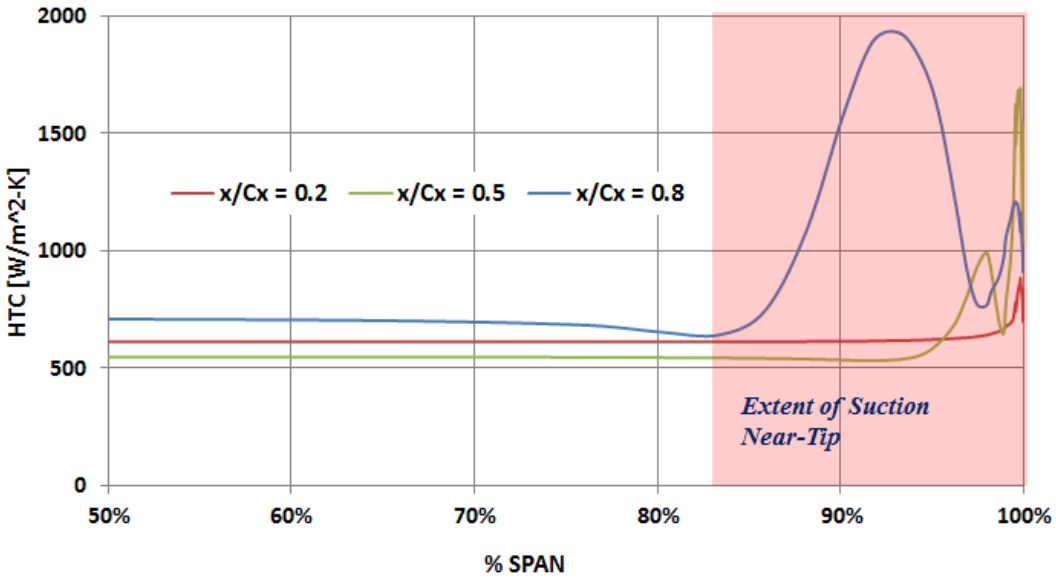

Figure 1.20: Suction surface spanwise distribution of heat transfer coefficient at x/C_x = 0.2, x/C_x = 0.5, x/C_x = 0.8 for M_{exit} = 1.0 (CFD)

Comparison to Literature and General Remarks

In other studies on near-tip heat transfer, Kwak et al. [23] had noted that the leakage vortex effect extended to nearly 20% span from the tip. Using mass transfer experiment measurements, Jin and Goldstein [22] found that the tip clearance effect is restricted to within 10% of the pressure side near-tip. These observations are in close agreement with the results of this study. In this study, the extent was found to be 17%. Even more interesting, this study has shown that the size of this region does not change with exit Mach/Reynolds number. The exit Reynolds number, though at low freestream, turbulence, increased the mass transfer on the near-tip regions. A study by Metzger and Rued [20] using a sink flow model showed that near-tip gap flow is highly accelerated and undergoes relaminarisation near the pressure side gap. However, this study is the first one to the authors' knowledge, where this characteristic has been studied on

actual rotor blade geometry at real turbine conditions. The leakage flow was also found to generate local heating near the gap. These studies align well with the observations made in this study thus far.

CONCLUSIONS

A numerical study on the aero-thermal performance of a gas turbine blade tip and near-tip surface has been performed under land based gas turbine representative conditions. The transonic exit flow Mach number was varied and changes in tip and near-tip heat transfer distribution investigated. The results provided detailed insight of the flow structure and heat transfer and the following key conclusions were made from this study:

1) Increasing the exit Mach number in the transonic range causes the tip heat transfer to increase. This is caused by high speed streamline divergence that generates turbulence near the leading edge and strong supersonic reattachment along the downstream pressure side edge. In this study, it was noted that at M_{exit} = 0.85 tip heat transfer is primarily dominated by upstream cross-flow. However, at sonic exit speeds, reattachment and shock-boundary layer interaction play a significant role in increasing the heat load on the blade tip.
2) By pushing the hot main flow into the boundary layer, the tip leakage vortex creates a high heat transfer region along the impingement line on the suction side near the tip. As a result, the near-tip heat transfer within the leakage vortex region is comparable to leading edge impingement heat transfer levels. Increasing the exit Mach from 0.85 to 1.0 increases the surface heat transfer by 25% over most of the blade. However, within the leakage vortex region, the heat transfer increase can be as high as 38%. Furthermore, the upstream leakage vortex has minimal effect on near tip heat transfer.

3) The size of the near-tip region affected by the leakage vortex is insensitive to exit Mach/Reynolds number. This means the radial size of the leakage vortex is unaffected by exit Mach/Reynolds number but the strength of the vortex increases considerably. The maximum spanwise extent of the heat affected region was found to be ~17% span from the tip at $x/Cx = 0.8$.

4) On the Pressure side near-tip, increasing the exit Mach/Reynolds number induces strong flow relaminarisation near the tip gap clearance. This is caused by flow acceleration into the tip gap.

Acknowledgements

This work was sponsored by Solar Turbines Inc. Special thanks to Dr. Kwak of South Korea Aerospace University for his inspiring discussions and suggestions during his sabbatical at Virginia Tech.

REFERENCES

[1] Bunker, R., 2006, "*Axial Turbine Blade Tips: Function, Design, and Durability*," AIAA Journal of Propulsion and Power, Vol. 22, No. 2, pp. 271-285.

[2] Bunker, R., 2001, "*A Review of Turbine Blade Tip Heat Transfer*," Ann. N.Y. Acad. Sci., 934, pp. 64-79.

[3] Mayle, R. E., and Metzger, D. E., 1982, "*Heat Transfer at the Tip of an Unshrouded Turbine Blade*," Proceedings of the Seventh International Heat Transfer Conference, Hemisphere, New York, pp. 87–92.

[4] Key, N. L., and Art, T., 2006, "*Comparison of Turbine Tip Leakage Flow for Flat Tip and Squealer Tip Geometries at High-Speed Conditions*," ASME J. Turbomach, Vol. 128(2), pp. 213-220.

[5] Moore, J., and Tilton, J. S., 1988, "*Tip Leakage Flow in a Linear Turbine Cascade*", ASME J. Turbomach., Vol. 110, pp. 18-26.

[6] Bunker, R.S, Bailey, J.C., and Ameri, A.A, 2000, "*Heat Transfer and Flow on the First-Stage Blade Tip of a Power Generation Gas Turbine: Part 1-Experimental Results*," ASME J. Turbomach., Vol. 122, pp. 263-271.

[7] Azad, G., Han, J.C., and Teng, S., 2000, "*Heat Transfer and Pressure Distributions on a Gas Turbine Blade Tip*," ASME J. Turbomach., Vol. 122, pp. 717-724.

[8] Zhang, Q., O'Dowd, D. O., He, L., Oldfield, M. L. G., and Ligrani, P. M., 2011, "*Transonic Turbine Blade Tip Aerothermal Performance with Different Tip Gaps- Part I: Tip Heat Transfer*," ASME J. Turbomach., Vol. 133(4), pp. 1-9.

[9] Ameri, A.A, Steinthorsson, E., and Rigby, D.L., 1999, "*Effects of Tip Clearance and Casing Recess on Heat Transfer and Stage Efficiency in Axial Turbines*," ASME J. Turbomach., Vol. 121, pp. 683-693.

[10] El-Gabry, L.A., 2009, "*Numerical Modeling of Heat Transfer and Pressure Losses for an Uncooled Gas Turbine Blade Tip: Effect of Tip Clearance and Tip Geometry*," ASME J. Thermal Science and Engineering Applications, Vol. 1, 022005, pp. 1-9.

[11] Tallman, J., and Lakshminarayana, B., 2001, "*Numerical Simulation of Tip Leakage Flows in Axial Flow Turbines, with Emphasis on Flow Physics: Part I-Effect of Tip Clearance Height*," ASME J. Turbomach., Vol. 123, 041027, pp. 314-323.

[12] Nasir, H., Ekkad, S., Kontrovitz, D., Bunker, R., and Prakash, C., 2004, "*Effect of Tip Gap and Squealer Geometry on Detailed Heat Transfer Measurements Over a High Pressure Turbine Rotor Blade Tip*," ASME J. Turbomach., Vol. 126, pp. 221-228.

[13] Liu, J., Li, P., Zhang, C., and An, B.T, 2013, "*Flowfield and Heat Transfer Past an Unshrouded Gas Turbine Blade Tip with Different Shapes*," J. Thermal Science, Vol. 22, pp. 228-134.

[14] Kwak, J.S., Ahn, J., Han, J.C., Lee, C.P., Bunker, R.S., Boyle, R., and Gaugler, R., 2003, "*Heat Transfer Coefficients on the Squealer Tip and Near-Tip Regions of a Gas Turbine Blade with Single or Double Squealer*," ASME J. Turbomach., Vol. 125, pp. 778-787.

[15] Wheeler, A. P. S., Atkins, N.R., and He, L., 2011, "*Turbine Blade Tip Heat Transfer in Low and High Speed Flows*," ASME J. Turbomach., Vol. 133(4), pp. 1-9.

[16] Wheeler, Andrew P.S., and Richard Sandberg. "*Direct Numerical Simulations of a Transonic Tip Flow with Free-stream Disturbances*," Proc. of ASME 2013 Turbine Blade Tip Symposium and Course Week, Hamburg.

[17] Zhang, Q., L. He, and A. Rawlinson. "*Effects of Inlet Turbulence and End-Wall Boundary layer on Aero-thermal Performance of a Transonic Turbine Blade Tip*," Proc. of ASME 2013 Turbine Blade Tip Symposium and Course Week, Hamburg.

[18] Atkins, N.R., Thorpe, S.J., and Ainsworth, R.W., 2012, "*Unsteady Effects on Transonic Turbine Blade-Tip Heat Transfer*," ASME J. Turbomach., 1Vol.134, pp. 1-11.

[19] Li, J., Sun, H., Wang, J., and Feng, Z., 2013, "*Numerical Investigations on the Steady and Unsteady Leakage Flow and Heat Transfer Characteristics of a Rotor Blade Squealer Tip*," J. Thermal Science., Vol. 20, pp. 204-311.

[20] Metzger, D.E., and Rued, K., 1989, "*The Influence of Turbine Clearance Gap Leakage on Passage Velocity and Heat Transfer Near Blade Tips: Part I-Sink Flow Effects on Blade Pressure Side*," ASME J. Turbomach., Vol. 111, pp. 284-292.

[21] Metzger, D.E., and Rued, K., 1989, "*The Influence of Turbine Clearance Gap Leakage on Passage Velocity and Heat Transfer Near Blade Tips: Part II-Source Flow Effects on Blade Suction Sides*," ASME J. Turbomach., Vol. 111, pp. 293-300.

[22] Jin, P., and Goldstein, R.J., 2003, "*Local Mass/Heat Transfer on Turbine Blade Near-Tip Surfaces*," AIAA Journal of Thermophysics and Heat Transfer, Vol. 17, No. 3, pp. 297-303.

[23] Kwak, J.S., and Han, J.C., 2003, "*Heat Transfer Coefficients of a Turbine Blade-Tip and Near-Tip Regions*," ASME J. Turbomach., Vol. 125, pp. 769-677.

[24] Menter, F.R., 1994, "*Two-Equation Eddy-Viscosity Turbulence Models for Engineering Applications*," AIAA Journal, Vol. 32, No. 8, pp. 1598-1605.

[25] Nasir, S., Carullo, J.S., Ng, W.F., Thole, K.A., Wu, H., Zhang, L.J., and Moon, H.K., 2009, "*Effects of Large Scale High Freestream Turbulence, and Exit Reynolds Number on Turbine Vane Heat Transfer in a Transonic Cascade*," ASME J. Turbomach., Vol. 131, 021021.

[26] K. Anto, S. Xue and W.F. Ng, L.J. Zhang and H.K. Moon, "*Effects of Tip Clearance Gap and Exit Mach Number on Turbine Blade Tip and Near-Tip Heat Transfer*," Proceedings of ASME Turbo Expo GT2013-94345.

[27] Luo, J., and Razinsky, E.H., 2008, "*Prediction of Heat transfer and Flow Transition on Transonic Turbine Airfoils under High Freestream Turbulence*," Proceedings of ASME Turbo Expo GT2008-50868.

[28] Ameri, A. A., and Bunker, R. S., 2000, "*Heat Transfer and Flow on the First-Stage Blade Tip of a Power Generation Gas Turbine: Part 2-Simulation Results*," ASME J. Turbomach., Vol. 122, pp. 272-277.

[29] Zhang, Q., O'Dowd, D. O., He, L., Wheeler, A. P. S., Ligrani, P. M., and Cheong, B. C. Y., 2011, "*Overtip Shock Wave Structure and Its Impact on Turbine Blade Tip Heat Transfer*," ASME J. Turbomach., Vol. 133(4), pp. 1-8.

CHAPTER 2

An Experimental and Numerical Study on the Aerothermal Characteristics of a Ribbed Transonic Squealer-Tip Turbine Blade with Purge Flow

A. Arisi, J. Phillips, W. F. Ng, S. Xue
Mechanical Engineering Department
Virginia Polytechnic Institute and State University
Blacksburg, VA 24061

H.K. Moon, L. Zhang
Solar Turbines Inc.
San Diego, CA 92101

ASME-IGTI Paper GT2015-43073

Recommended for publication in the Journal of Turbomachinery

ABSTRACT

Detailed heat transfer coefficient (HTC) and film cooling effectiveness (Eta) distribution on a squealer tipped first stage rotor blade were measured using an infrared (IR) technique. The blade tip design, obtained from a Solar Turbines Inc. gas turbine, consisted of double purge hole exits and four ribs within the squealer cavity, with a bleeder exit port on the pressure side close to the trailing edge. The tests were carried out in a transient linear transonic wind tunnel facility under land-based engine representative Mach/Reynolds number. Measurements were taken at an inlet turbulent intensity of Tu =12%, with exit Mach numbers of 0.85 ($Re_{exit}=9.75x10^5$) and 1.0 ($Re_{exit} = 1.15x10^6$) with the Reynolds number based on the blade axial chord and the cascade exit velocity. The tip clearance was fixed at 1% (based on engine blade span) with a purge flow blowing ratio BR= 1.0. At each test condition, an accompanying numerical study was performed using Reynolds Averaged Navier Stokes (RANS) equations solver ANSYS Fluent to further understand the tip flow characteristics. The results showed that the tip purge flow has

a blocking effect on the leakage flow path. Furthermore, the ribs significantly altered the flow (and consequently heat transfer) characteristics within the squealer tip cavity resulting in a significant reduction in film cooling effectiveness. This was attributed to increased coolant-leakage flow mixing due to increased recirculation within the squealer cavity. Overall, the peak heat transfer coefficient on the cavity floor increased with exit Mach/Reynolds number.

NOMENCLATURE

BR Averaged blowing Ratio (BR = $\rho_c U_c / \rho_\infty U_{\infty,avg}$)

C True chord of blade (69.9 mm, 2.75 in)

C_x Axial chord of blade (58.2 mm, 2.29 in)

C_{p0} Total pressure loss coefficient ($\boldsymbol{C_{p0} = \frac{P_{0_1} - P_{0_2}}{P_{0_1} - P_{s_2}}}$)

h Convective heat transfer coefficient (HTC) [W/m^2·K]

k Thermal conductivity [W/m·K] M Mach number

P Pressure [Pa]

q" Heat flux [W/m^2]

Re Reynolds number

T Temperature [K]

TG Tip Clearance Gap (% of engine blade span)

Tu Turbulence intensity at cascade inlet

Greek Symbols

α Thermal diffusivity [m^2/s]

η (Eta) Local film cooling effectiveness

ρ Local density of air [kg/m^3]

ø Overall film cooling effectiveness

Subscripts

1 Inlet conditions

2 Exit conditions

aw Adiabatic wall

c Coolant

i Initial conditions

o Stagnation or total

r Recovery

w Wall

∞ Mainstream

INRODUCTION

In modern gas turbine engines, air is pressurized in a compressor, mixed with fuel and ignited in a combustor. This hot, pressurized gas then enters the turbine section where power is extracted for various applications. The efficiency of a gas turbine engine can be improved by increasing the turbine inlet temperature. As a result, the turbine inlet temperature is continually increasing beyond the blade material yield temperature.

The turbine blade tips in these engines are exposed to high thermal and mechanical loads and are therefore very susceptible to failure. Bunker [1] reports that approximately one third of high pressure turbine failures occur due to blade tip degradation. Leakage flow over the tip of an unshrouded turbine blade is the cause of both mechanical failure and decreased efficiency. These deficiencies are exacerbated due to the transonic conditions present in the three dimensional flow over the turbine tip [2]. The tip clearance, which allows for rotational motion of the blade, is also

a source of aerodynamic losses due to pressure-to-suction leakage flow. Such challenges have necessitated sustained research in the aero-thermal characteristics of the rotor tip and near-tip through experimental and numerical studies.

The effect that the tip gap has on the flow field was studied by Sjolander and Cao [5] for simplified flat tipped blade geometry in a low speed stationary linear cascade. Using flow visualization and chord-wise pressure measurements, they found that the flow over the tip of the blade separates at the pressure side edge and can reattach further down the flow path on the surface of the tip. Anto et al. [6] conducted heat transfer measurements on a flat tip Macor blade under isentropic exit Mach numbers of 0.85 and 1.05 and tip gap clearances of 1% and 2%. Their study found that the heat transfer coefficient increased with increasing Mach number. Furthermore, an increase in Mach number, from 0.85 to 1.05, produced a larger heat transfer coefficient increase than an increase in the tip gap, from 1% to 2%. Numerous other studies [7 - 9] among many others have been carried out to study heat transfer and flow characteristics over a flat tip turbine blade

In an effort to offset the high thermal loads and aerodynamic losses, recent turbine designs have a squealer tip geometry where recirculating flow within the squealer cavity acts as a labyrinth seal for reducing leakage flow. It is also common for coolant flow from the internal cooling passages to be ejected through tip purge holes, thereby protecting the tip surface from thermal damage. In other modern blade tips, ribs are often incorporated within the squealer tip cavity for structural purposes and this subsequently affects the leakage flow behavior and overall tip heat transfer distribution.

Numerous studies on squealer tips have been carried out in low speed facilities [10-17]. Kwak et al. [10] conducted their heat transfer tests on a single and double squealer tips with

1.0%, 1.5% and 2.5% tip gap. The authors found that the heat transfer coefficient on the blade tip and endwall were significantly reduced by the use of a squealer tip, as opposed to a flat tipped blade. They also observed that changing the squealer rim location changed the leakage flow path which in turn produced different heat transfer distributions across the tip. Azad et al. [11] concluded that the use of a squealer rim significantly reduces the amount of leakage flow over the blade tip as compared to a flat tipped blade. A study by Azad et al. [12] concluded that the squealer tip heat transfer increases as the tip clearance size increases. Park et al. [13] analyzed the aerothermal characteristics of a multi-cavity squealer tip under low-speed, low turbulence conditions. The authors observed that multi-cavity squealer tip generally reduced the leakage flow pressure losses. Furthermore, the maximum heat transfer coefficient on the cavity floor was reduced with the peak tip heat transfer occurring on the rim surface near the leading edge.

The effect of tip surface film cooling has been of interest in recent research studies. Kwak et al. [14] added film cooling holes along the camber line to both flat and squealer tipped blades. They found that the overall heat transfer coefficient increased with increasing tip gap and decreased with increasing blowing ratio, while the film cooling effectiveness increased with increasing blowing ratio. In a numerical study by Ameri et al. [15], the authors noted that heat transfer on the squealer tip is strongly affected by the vortical flow within the cavity. Mhetras et al. [16] observed that higher blowing ratios on cooled squealer tips resulted in better film cooling effectiveness. Newton et al. [17] performed the aerothermal investigations of tip leakage on a purge cooled turbine blade. They tested the blade with tip gap of 1.6% and 2.8% chord under Reynolds Number of 2.3 x 105. They observed that a hot spot occurs where the

separate leakage flow reattaching the tip surface, and they also found the optimal blowing ratio is around 0.6 - 0.8 for the purge cooling.

A few studies have been carried out under transonic conditions. Key et al. [18] conducted an aerodynamic study at the squealer tip region. Using flow-vis and pressure measurements, the authors found that the squealer tip geometry was very effective in reducing leakage flow. Zhou et al. [19] studied the aerodynamic performance/losses from cooled tips. It was found that tip cooling induces aerodynamic losses and that the purge coolant blockage effect was more significant for flat tips than squealer tips. Recent study by Naik at al. [20] on a full and partial squealer tip with very low turbulence intensity of 0.8% concluded that coolant from purge holes generated local cold spots on the endwall.

As evidenced in the preceding section, many studies have been conducted, both experimental and numerical, on the tip region of turbine blades. However, most of these studies have been conducted at low speeds and low turbulence intensities. The effect that Mach/Reynolds number has on heat transfer coefficient and film cooling effectiveness of a squealer tipped blade has not been examined to this researcher's knowledge. This study also reports new data on the complex flow and heat transfer characteristics of a squealer tip with combined purge flow and ribs present within the squealer cavity.

EXPERIMENTAL SETUP

This study was conducted at Virginia Tech's Transonic Wind Tunnel, which is a blow down facility. This facility has been used in previous heat transfer experiments by Anto [6], Holmberg [21], Nix et al. [22], Smith et al. [23], Popp et al. [24], Carullo et al. [25] and Nasir et al. [26]. Figure 2.1 shows a scale drawing of the wind tunnel as seen in the test facility.

An upstream compressor safely pressurizes air into a tank after which a control valve regulates the inlet pressure at a steady level for up to 20 seconds. Before a heat transfer run is performed, valves 1 and 2 are closed and the heater and fan are turned on. When the heating loop reaches ~115°C (240°F) the valves are opened, allowing pressurized air through the heat exchanger. An upstream passive turbulence grid generates free-stream turbulence intensity of 12% as measured and validated by Nasir et al. [26]. The periodicity of a similar cascade with the same blade geometry was determined by Carullo et al. [25].

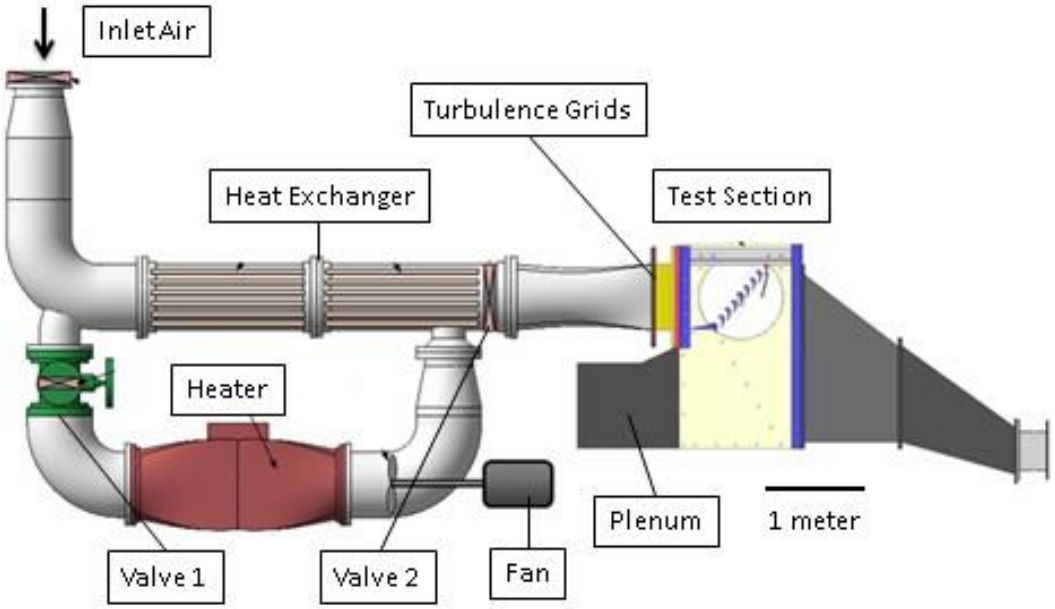

Figure 2.1: Scale model of the Transonic Wind Tunnel at Virginia Tech

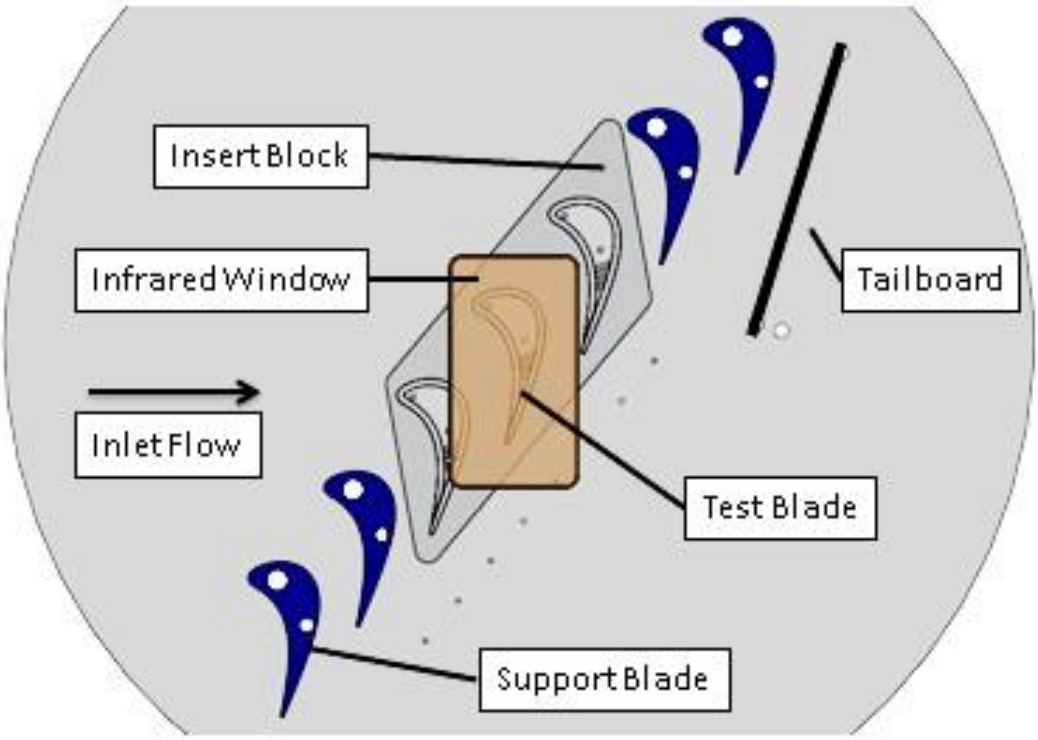

Figure 2.2: Linear cascade with three squealer tipped blades, capable of purge flow blowing

The test section consists of seven full blades, with the three center blades having identical tip clearances and squealer tip geometry as shown in Figure 2.2. The cascade has a pitch of 58.2 mm (2.29 in.) and a turning angle of 107.5°. The true and axial chord values are 69.9 mm (2.75 in.) and 58.2 mm (2.29 in.), respectively. The inlet total and static pressures were measured upstream of the blades. Static pressure was also measured 0.5 C downstream of the blades and used to calculate the isentropic exit Mach and Reynolds number. In this facility, the Mach number and Reynolds number are coupled and cannot be varied independently.

Figure 2.3 shows the geometry of the test blade model. The blade was printed using ABS P-430 material which is a low conductivity polycarbonate (k = 0.188 W/m-K). The cavity depth of the squealer was 2.29 mm (0.09 in.), with two 2.54 mm (0.1 in.) diameter purge holes. The downstream section of the squealer cavity had four support ribs and a bleeder opening on the pressure side. Cooling air was supplied to the plenum of the three blades and the respective

plenum pressures were measured to ensure periodicity. However, heat transfer data was collected on only the central blade.

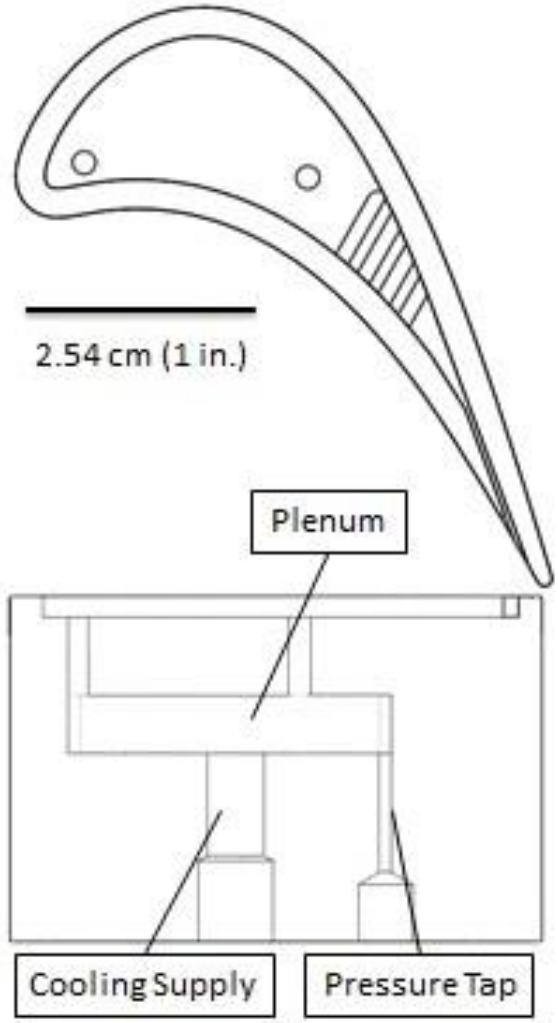

Figure 2.3: Squealer tip test blade geometry

DATA REDUCTION TECHNIQUE

The test blade was made of a low conductivity polycarbonate material with very short data acquisition time window. Therefore, a 1-D semi-infinite heat transfer conduction assumption (Equation (2.2)) was valid in most of regions on the measured surface, except near the edge, where the 2-d or 3-d conduction may cause ineligible errors in the HTC value. A finite difference code was then employed to calculate the surface heat flux from the measured surface temperatures.

$$\eta = (T_r - T_{aw})/(T_r - T_c) \tag{2.1}$$

$$\frac{\partial^2 \mathrm{T}}{\partial \mathrm{y}^2} = \frac{1}{\alpha}\frac{\partial \mathrm{T}}{\partial \mathrm{t}} \tag{2.2}$$

A two-test strategy with the Dual Linear Regression Technique developed by Xue et al. [27] was then used to determine the HTC and Eta. In this testing method, data was recorded at identical mainstream flow conditions and blowing ratio but with different coolant temperatures. The two sets of data were used to perform the linear regression calculation based on the following governing equation:

$$\frac{q}{T_r - T_c} = h\frac{T_r - T_w}{T_r - T_c} - h\eta \tag{2.3}$$

which can be derived from the definition of Eta in Equation (2.1), and the convective surface heat transfer equation:

$$\mathrm{q} = \mathrm{h}(\mathrm{T_{aw}} - \mathrm{T_w}) \tag{2.4}$$

The Dual Linear Regression Technique allows for the simultaneous calculation of Eta, HTC and T_r. The uncertainty associated with the HTC and film cooling effectiveness was calculated using the perturbation procedure described by Moffat [28]. The uncertainty was found to be ± 9.6% and ± 0.102 in h and Eta respectively.

NUMERICAL METHOD

Solver and Turbulence Models

In this study, the Reynolds-Averaged Navier Stokes Equations were solved using the commercial CFD solver ANSYS *Fluent 14.5*. A pressure-based steady-state solver was used. The transition-SST model, developed by Menter [29] based on the Wilcox k-omega model, was used with a wall integration approach to resolve the viscous sub-layer. Compressibility effects, curvature correction and viscous heating effects were accounted for in the model. Air was used as the working fluid and was modelled as an ideal gas. Viscosity, conductivity and specific

heat of the fluid were modelled using molecular kinetic theory. The SIMPLEC turbulence algorithm was applied and a second order or higher upwind advection scheme was used to solve the flow variables.

Computational Domain

Figure 2.4 shows the computational domain and a section of the tip and near-tip surface mesh. A multi-block structured grid was generated using the commercial meshing software *Pointwise v.17*. A total of ~7.0 million cells were used to resolve the domain after grid dependency study had been performed. The maximum y+ values on the tip and shroud/casing surfaces was y+ < 3.0. Twenty cells were employed across the tip gap. This ensured that the flow around the squealer tip was effectively resolved.

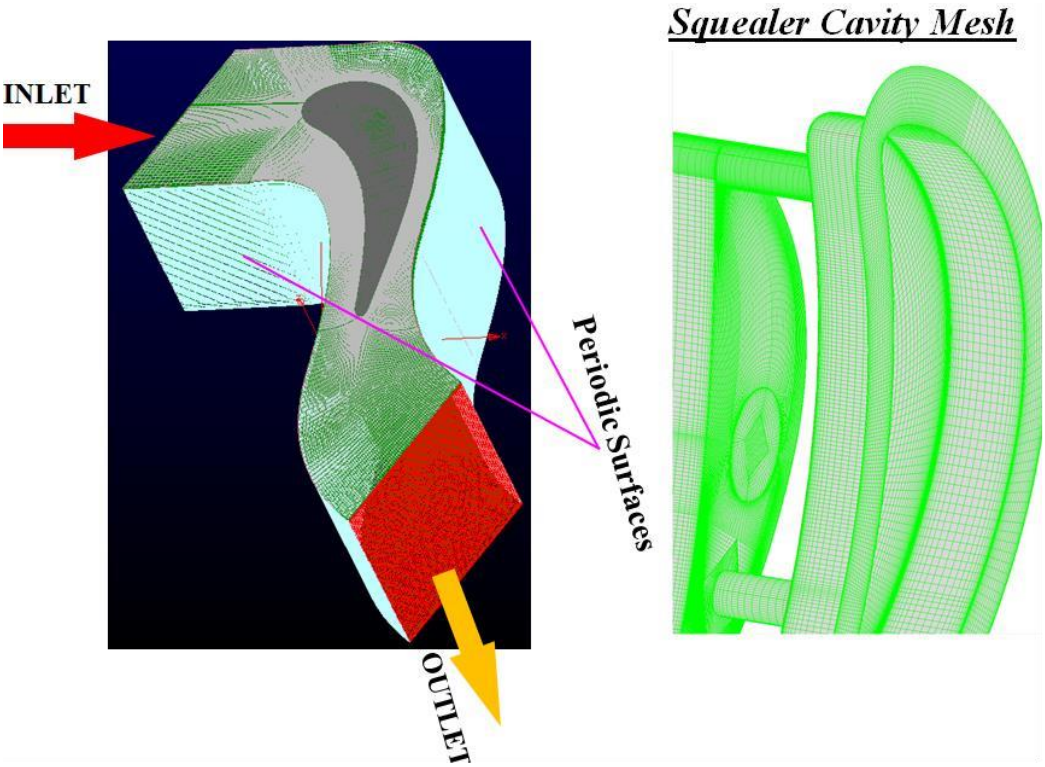

Figure 2.4: CFD computational domain

Three-Simulation Technique

To obtain both Eta and convective heat transfer coefficient from the numerical study, a Three-Simulation Technique proposed by Wu et al. [30] was employed. This technique involves three independent simulations that are performed with the same cascade inlet and exit conditions. The first simulation is performed without coolant injection in order to find the local T_r, which is also the adiabatic wall temperature for the case where there is no coolant injection. The second simulation is performed with a particular blowing ratio to find T_{aw} with the film cooling present. Based on the result of these two simulations, Eta can be calculated using Equation (2.1). The third simulation is performed with the same blowing ratio as the previous one, but with a constant surface heat flux boundary condition imposed on the blade surface. Combining with the result from the second simulation, the third simulation allows for the calculation of heat transfer coefficient using Equation (2.4).

RESULTS AND DISCUSSION

Velocity and Pressure Distribution

Figure 5 shows the experimental results from surface oil flow tests and CFD prediction of surface velocity vectors on the squealer tip. The experiment was carried out at design conditions (M_{exit} = 0.85/Re_{exit} = 9.75x10^5, BR = 1.0, tip gap = 1%) in order to determine the flow characteristic around the squealer tip. Different color pigment was applied on the blade pressure, suction, squealer cavity and squealer rim surfaces (yellow, green, red and blue respectively, with the background in black color). CFD prediction of the tip surface flow was also obtained from a numerical study conducted at matching conditions.

Paint accumulation was observed along the pressure side corner of the cavity and across the squealer cavity starting just downstream of the first purge hole. These regions are

characterized by recirculating and lift-off flows which lead to color pigment accumulation. Figure 2.5 shows majority of the paint was washed away in regions A and B, which indicates the impingement/reattaching of the cooling purge flow (because there is no mixing of the green or blue dye from the pressure side or the leading edge). These regions coincide with reattachment/impingement flow within the squealer cavity surface. Combining these observations, it becomes clear that the squealer cavity flow is dominated by strong vortical flow that develops just downstream of the first purge hole ($x/C_X \sim 0.2$) and grows in radial size further downstream. This vortical flow occupies almost the entire cavity width at $x/C_X \sim 0.3$ but then appears to dissipate approaching the second purge hole.

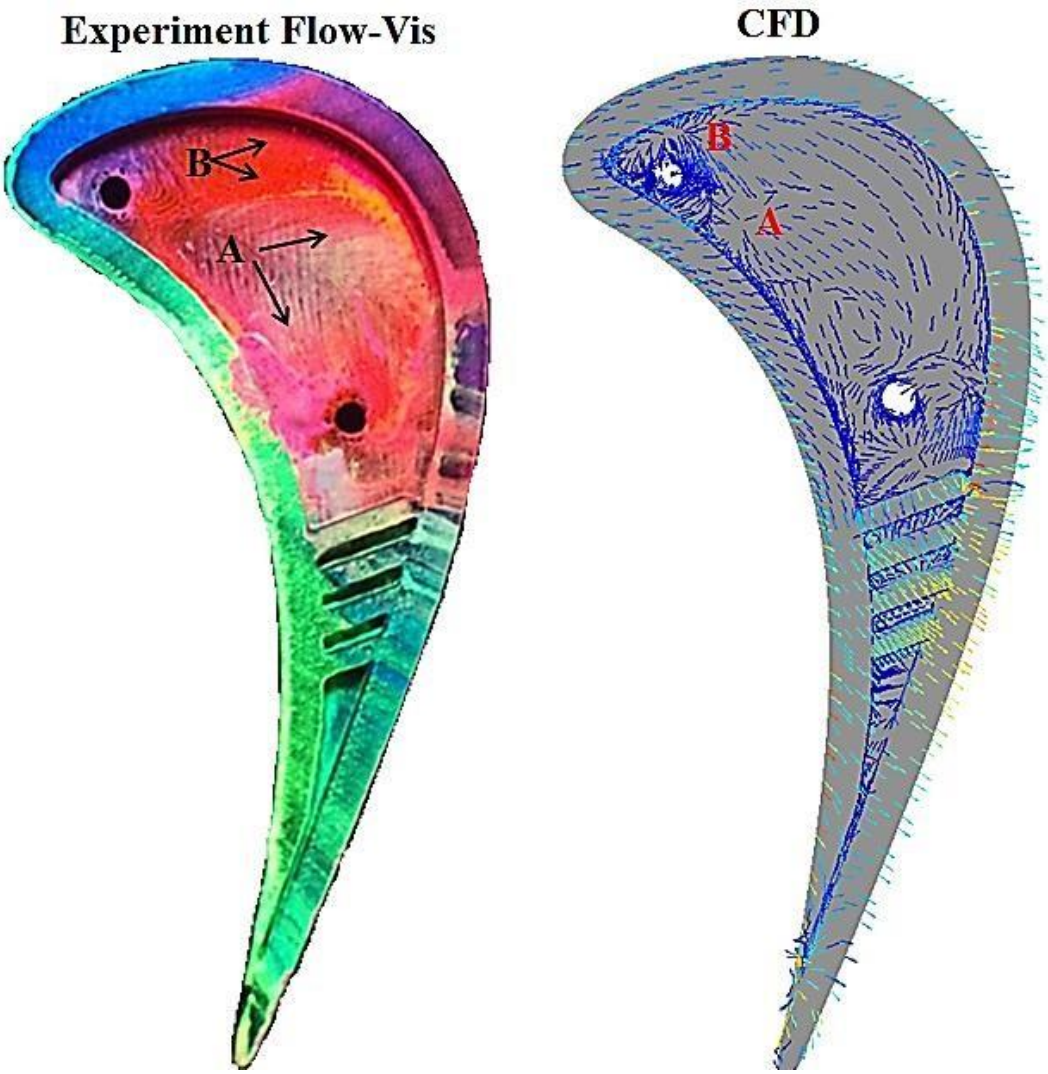

Figure 2.5: Experiment and CFD prediction of squealer tip surface flow at M_{exit} = 0.85

The distribution of the color pigment on the tip surface also sheds some light into the leakage flow characteristics. Between the leading edge and x/C_x ~0.25, there is no leakage flow with the suction side rim color pigment maintaining its original blue color. Slightly further downstream, between x/C_x ~ 0.25 and x/C_x ~ 0.6, the suction side rim is covered with the red color from the squealer cavity. This hints to the fact that the flow exiting the tip gap at this region is mainly from the purge flow which interacts strongly with the cavity floor color pigment. In fact, since no green coloration is present within the squealer cavity, it shows that the recirculation flow within the squealer cavity is very effective in protecting the blade tip from the

hot leakage flow in a gas turbine engine. The majority of pressure to suction leakage flow takes place downstream of the $x/C_x \sim 0.7$, over the ribs. This region in Figure 2.5 is covered by a thick layer of green pigment coming from the blade pressure side.

Figure 2.6 shows the CFD result of near-tip (94% span) pressure distributions for tips with ribs present and without ribs. It seems that with and without ribs present, the near tip pressure loading is about the same, except at downstream locations (s/c > 0.8). The ribs generate more pressure fluctuation and pressure drop on the suction side.

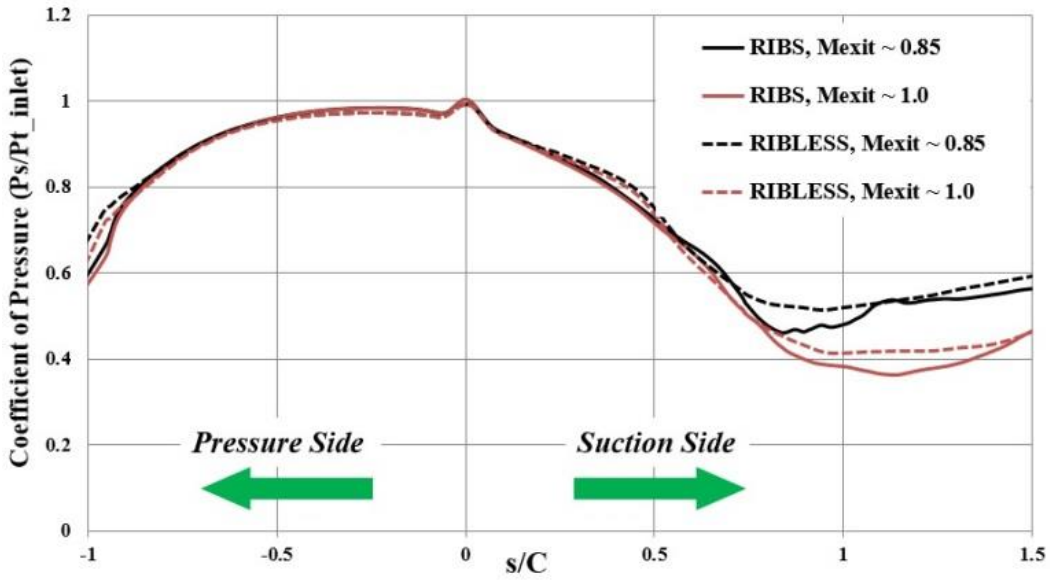

Figure 2.6: CFD result of near tip (94% height) pressure loading comparison between rib and ribless tip blade.

Effect of Ribs on Leakage Flow

It is important to compare the above described leakage flow behavior to that over a squealer tip without ribs within the cavity. As such, the effect of cavity ribs can be isolated. Such flow has been well documented in open literature such as the study by Key and Art [18], and the result obtained by these authors is shown in Figure 2.7a. Figure 2.7b shows CFD prediction of the surface flow for a similar blade geometry used in this study but without ribs. The two results, Figure 2.7a and Figure 2.7b, show very good qualitative agreement.

The presence of ribs within the squealer cavity significantly alters the flow characteristics around the blade tip. Consequently, significant difference in heat transfer results is expected as will be discussed in coming sections. From Figure 2.7a and 2.7b, the flow within the squealer cavity without the ribs is only in the downstream direction. The leakage flow also reattaches on the cavity surface at only one location (marked R on Figures 2.7a and 2.7b), before migrating from the cavity suction to pressure side along the drawn arrows. However, for the ribbed squealer cavity shown in Figure 2.7c, two reattachment regions are evident on the cavity floor (regions R). In between these two regions, a lift-off flow region forms, moving from the cavity pressure to suction side along the marked arrow (near region R). This is opposite to the flow observed for a squealer tip without ribs. Therefore, significant differences in heat transfer distribution of the two geometries is expected with impingement flow generally expected to create high heat transfer areas.

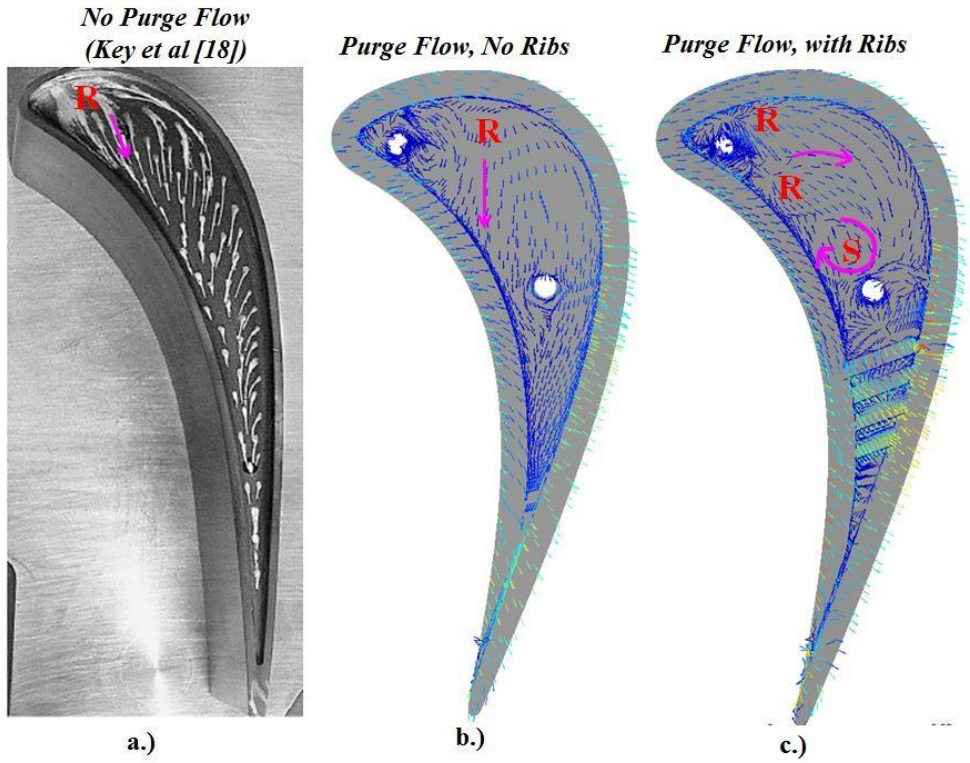

Figure 2.7: a) Surface oil flow-vis on a squealer tip with no ribs and no purge flow (Key and Art [18]). b) CFD prediction of near surface velocity vectors. c) Squealer tip with ribs near surface flow velocity vectors.

The ribs also have an effect of turning the flow in the upstream direction along the cavity pressure side edge. This result in a swirling flow developing in region S of Figure 2.7c; a feature not present on the squealer geometry without ribs. The ribs enhance the development of vortices and recirculating flows within the squealer cavity that would otherwise be less chaotic when the ribs are absent.

Although the ribs seem to have a limited impact on the near tip pressure distribution (as shown in Figure 2.6), they increase the total pressure loss significantly. Table 2.1 compares the mass weighted average total pressure loss coefficient between the rib and rib-less blade tip results. It can be seen that for both Mach numbers, the ribs increase the amount of total pressure loss. This is because the ribs fill up the cavity space, and compromise the sealing effect of the squealer tip.

Table 2.1: Total pressure loss coefficient (Cp_0) for different tip geometry at different exit Mach number

	$M_{exit} = 0.85$	$M_{exit} = 1.00$
RIBS	*0.069*	*0.096*
RIBLESS	*0.130*	*0.148*

Heat Transfer Results

A mesh dependency study was performed to verify that the present heat transfer result is independent of the grid density. Figure 8 shows the heat transfer coefficient result with different meshes under the same flow condition (exit Mach number 0.85). It can be seen that increasing the grid density does not significantly change the heat transfer distribution when the grid density is higher than 7.8 million cells.

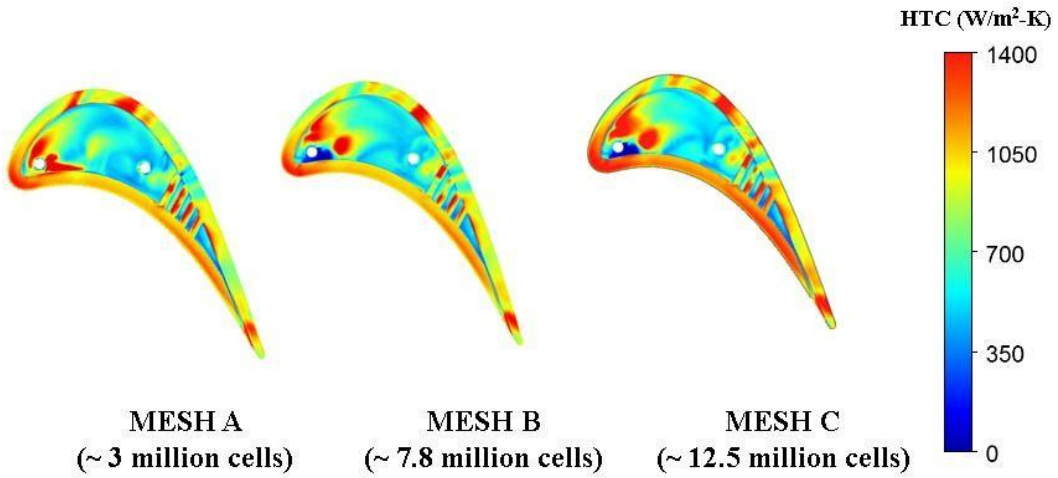

Figure 2.8: Heat transfer coefficient distribution of different mesh at exit Mach number 0.85

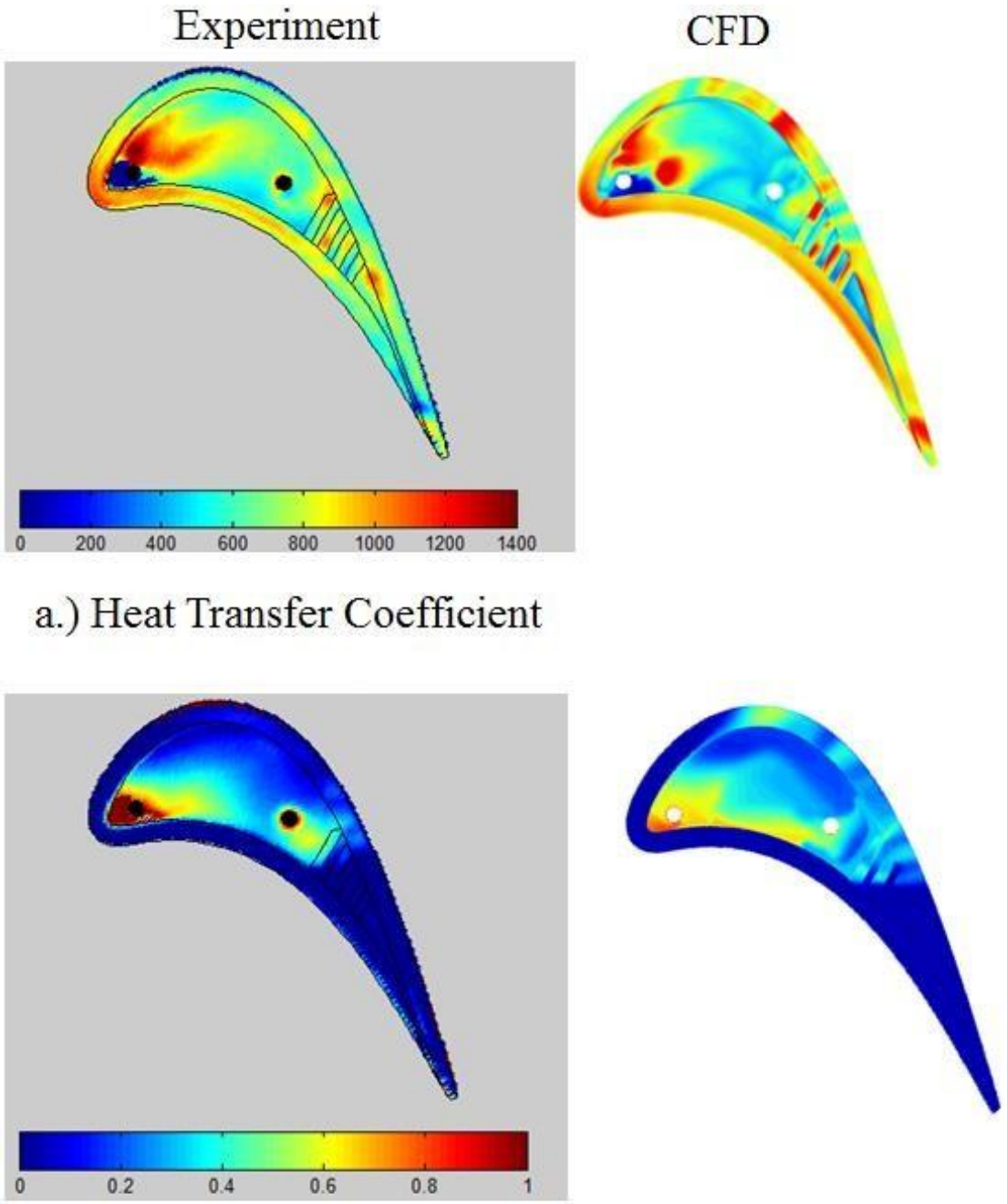

Figure 2.9: a) Experiment and CFD result of heat transfer coefficient distribution; b.) Experiment and CFD result of film cooling effectiveness distribution

Figure 2.9 shows the heat transfer coefficient and film cooling effectiveness distribution on the squealer tip at design engine conditions. The highest heat transfer coefficient within the squealer cavity is observed in a small region close to the first purge hole. From the preceding

discussion of the surface flow, these high heat transfer regions coincide with the reattachment/impingement flow. The level of heat transfer coefficient is higher than that on the squealer rim surface which is usually expected to be the peak heat transfer region on squealer tip geometry. Between this reattachment region and the second purge hole, there is relatively low heat transfer coefficient level. As flow moves over the ribs, the edges of the these ribs trip the flow creating "bursts" of turbulence that consequently result in the high heat transfer spots.

The distribution of film cooling effectiveness is shown in Figure 2.9b. The experimental result and numerical results agree well with each other. The highest film cooling effectiveness was measured and predicted at the cavity leading edge corner. Significant film cooling effect from the second purge hole is limited to the cavity pressure side, with close to zero film cooling observed towards the suction side. Film cooling effect from the second purge hole is limited and restricted to only the first two ribs of the squealer tip. Downstream of these ribs, there is no film cooling effect. These distributions of both heat transfer coefficient and film cooling is closely knit to the cavity flow features highlighted earlier and the coolant-leakage flow interaction. This is made clear from the CFD prediction discussed in detail in the following section.

Figure 2.10 to Figure 2.13 provide further insight into the squealer cavity flow characteristics. The figures represent cut planes across the squealer tip at different pressure side axial locations. The color contours on these planes represent the fluid temperature which in turn gives an indication of the coolant flow path and leakage-coolant mixing. Coolant flow regions are characterized by low fluid temperature whereas high mixing regions have faded temperature contours. The cutting planes were oriented along the average stream direction at specified pressure side x/C_x locations.

Upstream Cavity (x/Cx~0.1)

Figure 2.10 shows the flow vector plots along the shown cut plane with a colormap of the fluid static temperature. Recall from the discussion of Figure 2.9a, this cavity region was characterized by high heat transfer coefficient levels near the suction side and very high film cooling effectiveness around the cavity leading edge corner.

Notice that the purge flow actually never impinges on the casing surface. In fact, leakage flow from the pressure side close to the leading edge pushes the purge flow back into the cavity with very little mixing occurring between the leakage and purge flow. This causes the coolant to accumulate in the cavity leading edge corner resulting in the high film cooling effectiveness region noted in Figure 2.9b. Furthermore, the effective clearance the leakage flow "sees" is greater than one ($\sigma > 1$). This has a diffusing effect where the leakage flow path is slowed down and separation occurs on the casing surface just above the purge hole.

Mid-Section Cavity (x/Cx~0.2 – x/Cx~0.4)

Similar cutting planes to that in the preceding discussion were placed at x/C_x ~0.2 and x/C_x ~ 0.4. This is the region between the purge holes. Diminished film cooling effectiveness on the pressure side and high heat transfer close to the suction side were observed in the experiment results. At x/C_x ~ 0.2, the coolant accumulation along the pressure side is shown to have reduced because of the mixing caused by the growing cavity vortex. No recirculation bubble exists on the casing surface at this location. The coolant that was accumulating along the pressure side corner upstream is seen to entrain along the casing surface and this effectively cools the casing surface. This suggests that the rotor tip purge flow has a first order effect on cooling the engine shroud over the rotor tip surface.

At x/C_x ~ 0.4 shown in Figure 2.12, the flow within the squealer cavity is dominated by two counter-rotating vortices which result in complete mixing of the coolant and the leakage flow. This explains the low film cooling effectiveness aforementioned in Figure 2.9.

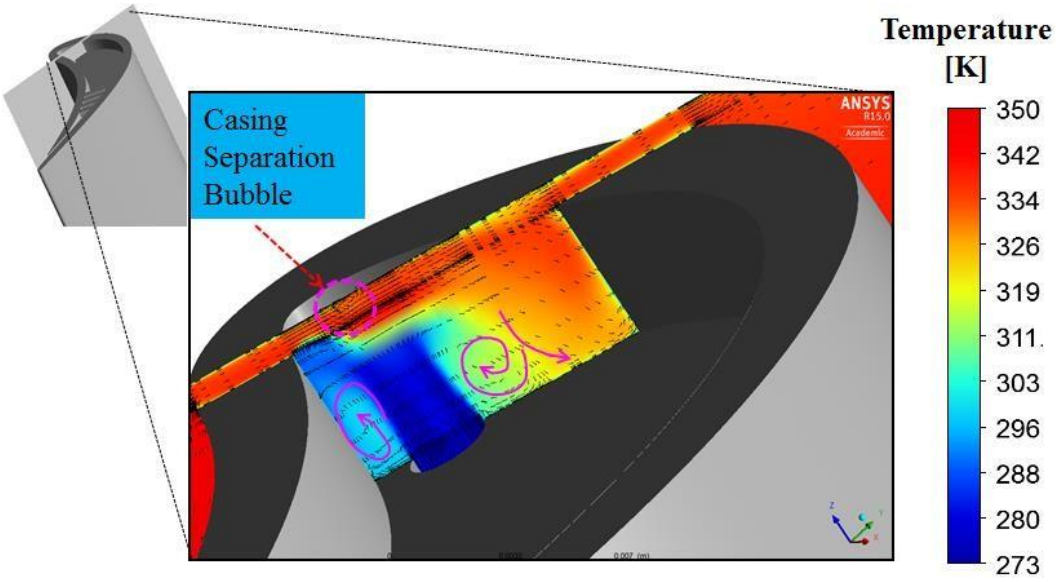

Figure 2.10: Velocity vector plot and cavity fluid temperature distribution along leakage path at x/C_x = 0.1

Downstream Cavity Region(x/Cx ~ 0.5)

The location shown in Figure 2.13 coincides with the second purge hole exit. Unlike the first purge hole flow, coolant from the second purge hole penetrates the leakage flow layer and impinges on the casing surface. The coolant is then entrained along the casing surface towards the suction side further reinforcing the idea of purge flow having a first order effect on shroud cooling. Because of the impingement of the flow onto the casing, the effective clearance is reduced to zero ($\sigma = 0$). This means that the leakage flow is blocked from crossing from the pressure to suction side at this location.

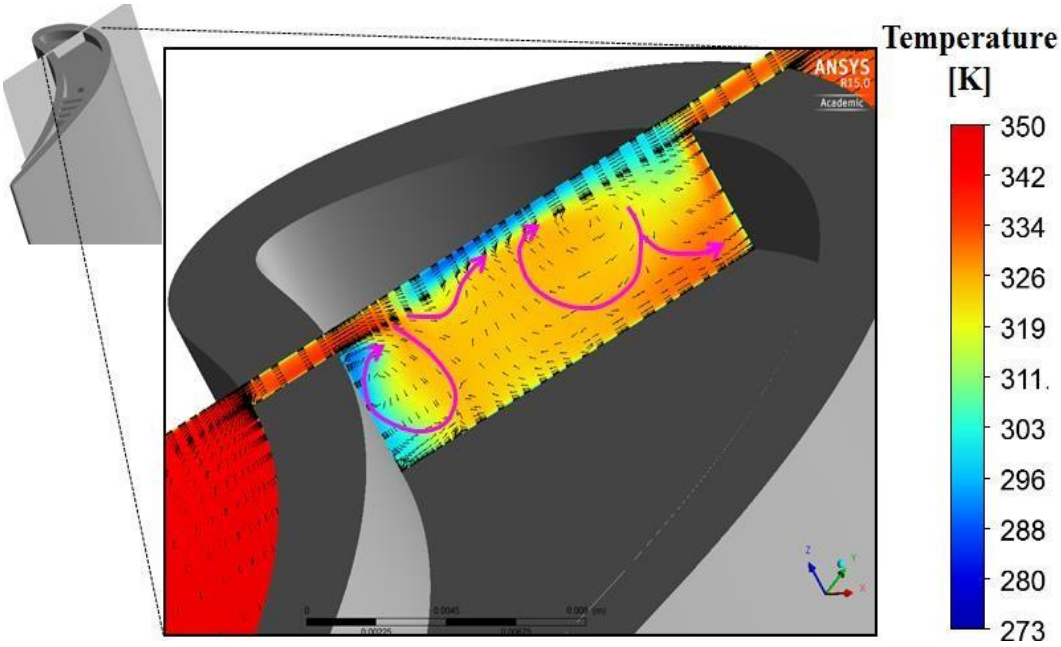

Figure 2.11: Velocity vector plot and cavity fluid temperature distribution along leakage path at $x/C_X = 0.2$

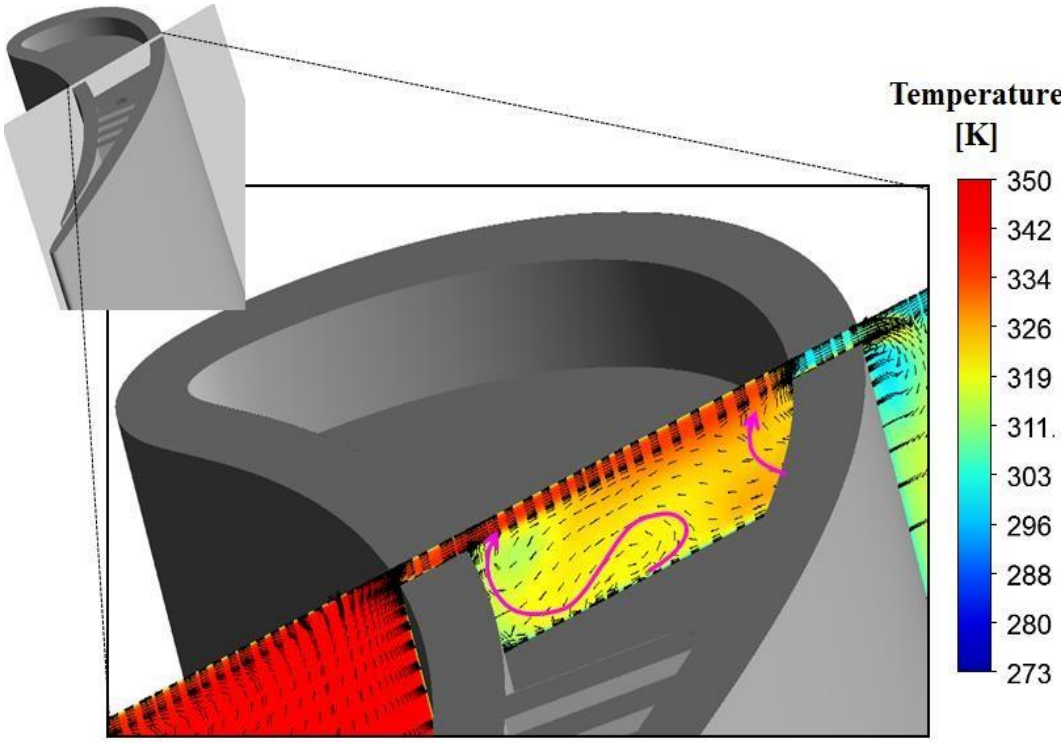

Figure 2.12: Velocity vector plot and cavity fluid temperature distribution along leakage path at $x/C_X = 0.4$

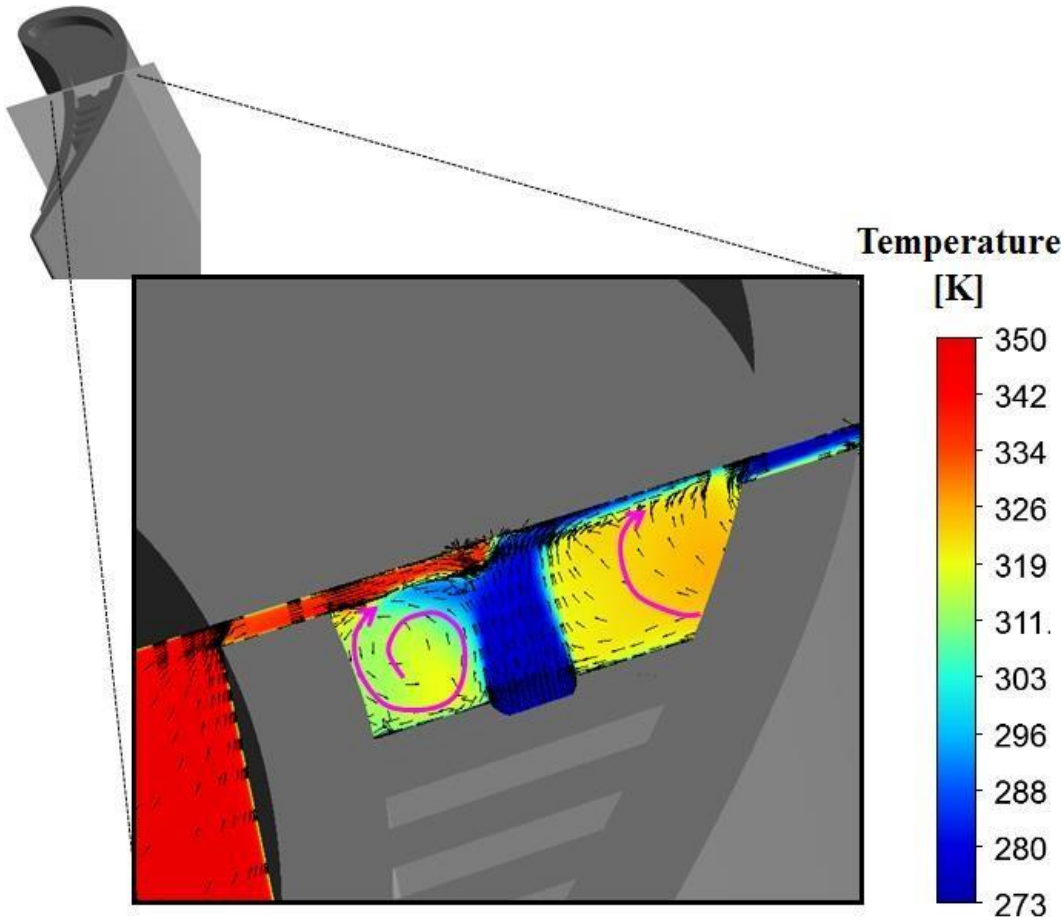

Figure 2.13: Velocity vector plot and cavity fluid temperature distribution along leakage path at x/Cx = 0.5

Effect of Purge Flow on Leakage Flow

From the preceding discussions, it was noted that the leakage- purge flow interaction varies between the two purge holes. Leakage flow seemed to penetrate the purge flow jet from the first hole but not that from the second purge hole. The authors believe that this phenomenon is linked to the static pressure on the blade pressure side. Close to the leading edge, the low speed flow (high pressure) overcomes the purge flow resistance. However, where the pressure side flow has a higher velocity, the low static pressure cannot overcome the purge flow jet and instead flows around the jet where the surrounding pressure is less. The resulting effect is that the purge flow blocks the region of the tip clearance and acts as a wedge splitting the leakage flow into two high speed streams on either side of the purge flow jet. Even though the

two purge flows are fed from the same pressure, the difference in penetration effect is because the leading edge purge flow "sees" a higher resisting pressure from the leakage flow. This is evident from the pressure measurements shown in Figure 2.14. These measurements were taken on the shroud surface adjacent the squealer tip. Two distinct high speed leakage flow regions (low static pressure ratio) were observed.

The CFD result further reinforces this observation. Figure 2.15 shows contours of leakage mass flow exiting the tip clearance. There is a high mass flux upstream and downstream of the purge hole and ribs. This also agrees with the flow visualization results where high leakage flow was suspected to occur over the downstream region of the blade tip.

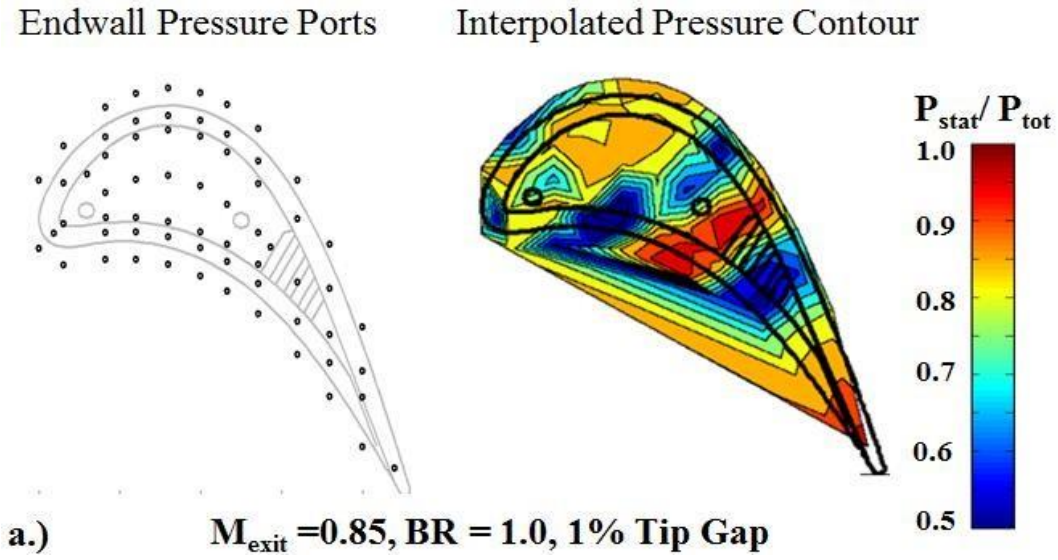

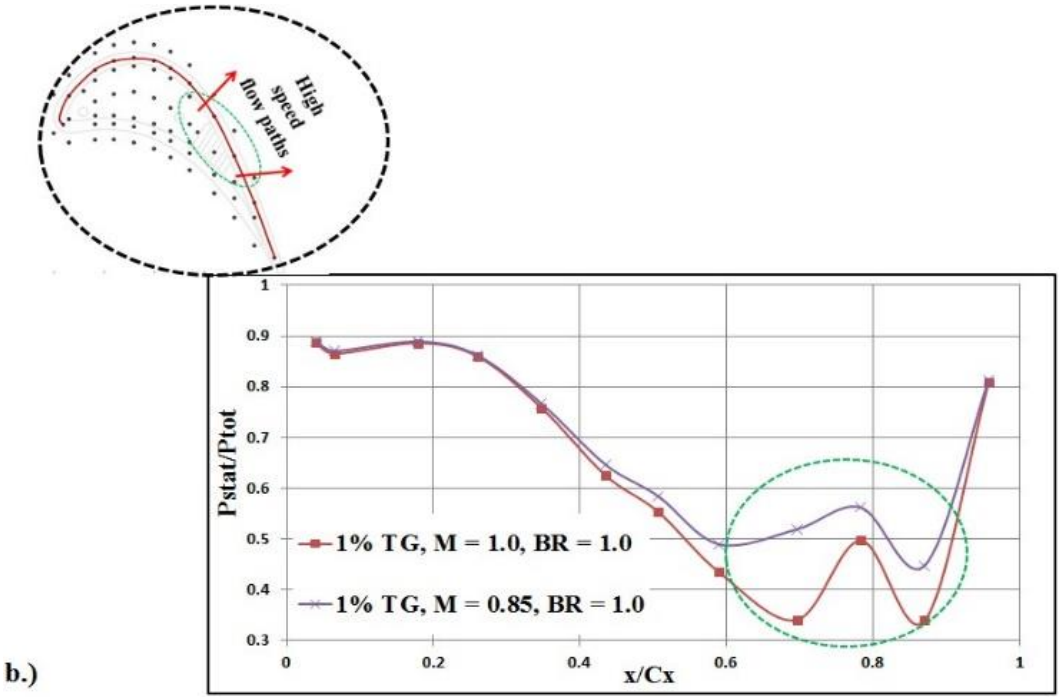

Figure 2.14: a) Pressure distribution on the endwall surface (Experiment); b) Static to total pressure ratio on the endwall surface above the suction side rim

Effect of Exit Mach/Reynolds number

Figure 2.16 compares the heat transfer coefficient and film cooling effectiveness distribution at M_{exit} = 0.85 and 1.0 (Re_{exit} = $1.15x10^6$). For M_{exit} = 1.0, the heat transfer level at the reattachment flow region on the squealer cavity and the rim surfaces increases. However, the size of this high heat transfer region remains relatively the same as that at M_{exit} = 0.85. This is because the vortical flow within the squealer cavity increases in strength but remains relatively the same size.

Near the cavity suction side, a region of low heat transfer ("sweet spot") becomes more distinct. Sweet spot regions on a blade tip surface have been long associated with only the flat tipped geometry. Most studies carried out on squealer tipped blades without ribs have not shown this feature. In this particular study, the authors allude that the formation of this squealer tip sweet spot is linked to the location of the first purge hole that causes two reattachment regions on either side of the hole. In between, lift off flow causes the low heat transfer region termed as

the sweet spot. With increasing exit Mach/Reynolds number, the sweet spot region appears to grow and heat transfer levels drop even further.

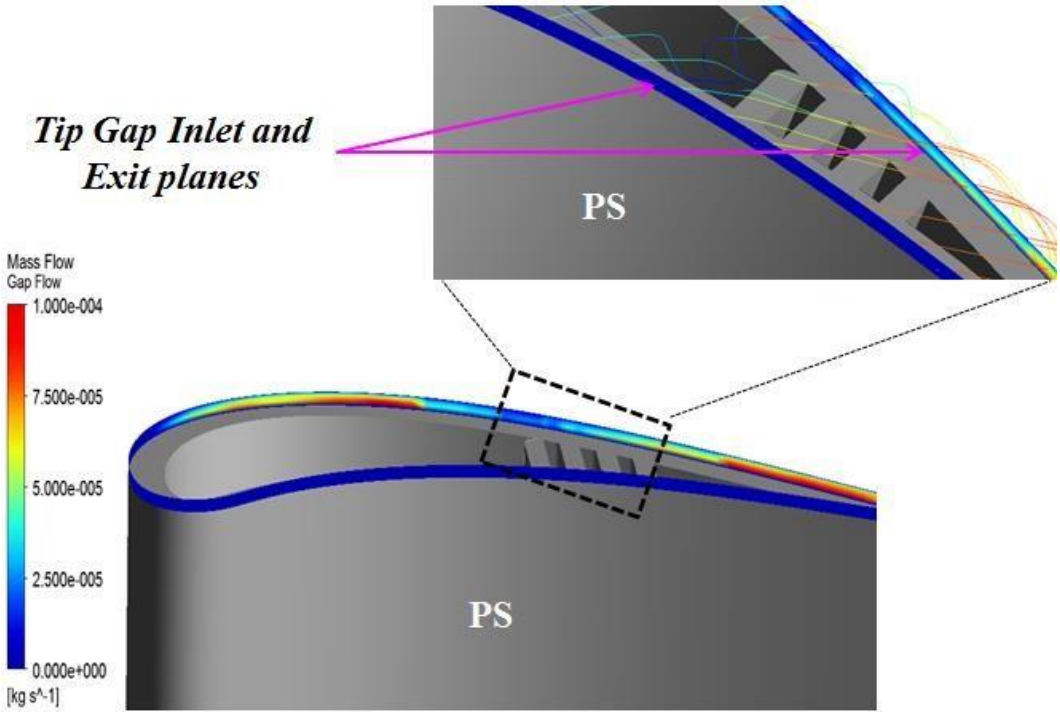

Figure 2.15: Contours of leakage mass flow rate at the tip clearance exit

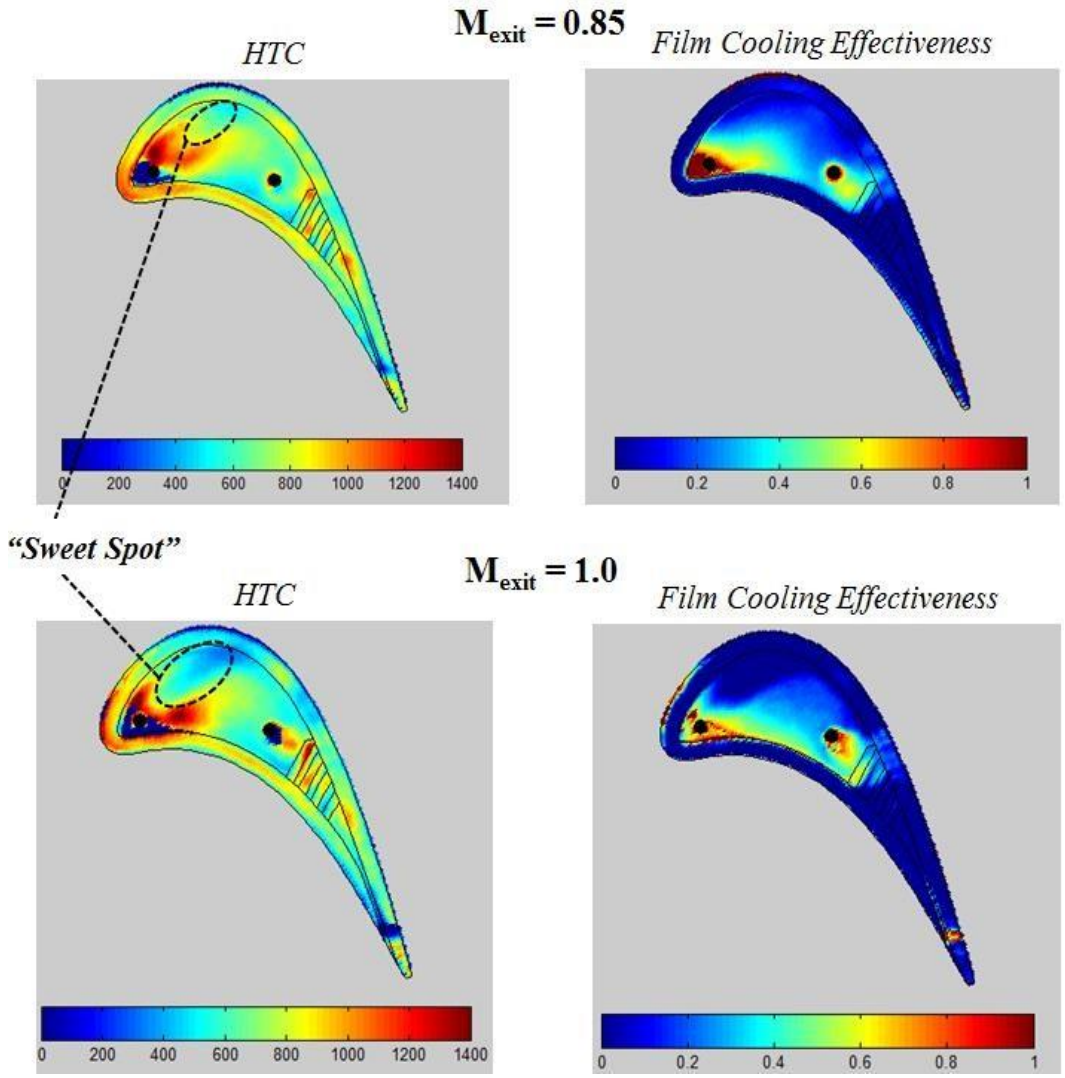

Figure 2.16: Heat transfer coefficient and film cooling effectiveness distributions on the squealer tip at M_{exit} = 1.0 (Experiment)

Film cooling effectiveness levels drop with increasing exit Mach/Reynolds number. The area of the squealer tip cavity cooled by the purge flow also diminishes with film cooling nearly nonexistent towards the suction side of the tip surface. The size of the recirculation region remains relatively the same between the two Mach/Reynolds number, but the recirculation velocity associated with the flow increases. This increased recirculation increases coolant-leakage flow mixing causing the reduction in film cooling effectiveness observed. It is also noted that the tip surface film cooling is restricted to within the squealer cavity i.e. upstream of the first rib, for both exit Mach/ Reynolds number. This is because the ribs block the coolant

flow path thereby preventing the rib surfaces and the downstream tip surface from being effectively cooled by the purge flow.

Comparison to Literature and General Remarks

At this point, it is worth discussing some of the observations and conclusions drawn from this study in relation to studies documented in open literature. Kwak and Han [14], Ameri et al. [15], and Naik et al. [20], among others, also noted that the peak heat transfer region on the cavity floor occurs where the flow reattached close to the leading edge. The studies by Kwak and Han [14] and Ameri et al. [15] found that the peak heat transfer occurred on the squealer rim surface. In this study, the peak heat transfer was noted to be on the cavity floor at the reattachment region close to the leading edge. Furthermore, the formation of double reattachment region and a "sweet spot" on a squealer tip has not been noted before in open literature. Sweet spot formation has commonly been associated with only the flat tip geometry. This aerothermal characteristic is shown to be strongly related to the combined effect of cavity ribs and tip purge flow close to the leading edge. This study also agrees with the observation noted by the Naik et al. [20] that tip purge flow has a cooling effect on the engine shroud. Finally, this study reveals that introduction of cavity ribs enhances cavity swirl flows and induces reverse cavity flow (downstream to upstream). Such cavity flow characteristic has not been reported before to this author's knowledge.

CONCLUSIONS

An experimental and numerical study on the aero-thermal characteristic of a gas turbine blade tip has been performed under land based gas turbine representative conditions. The blade comprised of unique squealer tip geometry with ribs and purge flow within the squealer tip cavity. The distribution of heat transfer coefficient and film cooling effectiveness on

this blade tip was analyzed at M_{exit} = 0.85 and 1.0. Numerical results were also used to shed light into the tip flow characteristics that explain the heat transfer and film cooling distributions observed. The following were the key conclusions from this study.

a.) The peak heat transfer region on a squealer tip is caused by flow reattachment squealer cavity floor. This peak level increases with increasing exit Mach/Reynolds number. However, the size of the "sweet spot" region within the squealer cavity floor increases and the sweet spot heat transfer coefficient levels reduce.

b.) Film cooling within the squealer cavity diminishes with increasing exit Mach/Reynolds number as a result of increased recirculation strength of the cavity vortical flows.

c.) The purge flow from the squealer tip has a blocking/sealing effect on the tip clearance. Consequently, high leakage mass flow occurs downstream of the purge hole; low leakage mass flow occurs directly across the purge hole.

d.) Distribution of purge flow coolant within the squealer cavity suggested that the tip purge flow has a first order effect on cooling the casing surface compared to the tip surface. This was evident from the entrainment of low temperature coolant fluid along the casing/shroud surface.

e.) The presence of ribs within the squealer cavity significantly alters flow characteristic on the squealer tip. Reversed cavity flow (downstream to upstream) develops in the cavity. Overall, squealer tips with ribs or other forms of interference will tend to trip more complex swirling flows in the squealer cavity compared to those without ribs.

f.) Ribs on the squealer cavity have a detrimental effect on film cooling due to their blocking effect. As a result, high heat transfer levels and low film cooling effectiveness occurs on the tip surface downstream of the ribs.

ACKNOWLEDGEMENTS

Special thanks to Dr. Jae Su Kwak of the South Korea Aerospace University for his inspiring discussions and suggestions during the course of this work.

REFERENCES

[1] Bunker, Ronald. "*Axial Turbine Blade Tips: Function, Design, and Durability*," Journal of Propulsion and Power 22.2 (2006): 271-85.

[2] Bunker, R., "*A Review of Turbine Blade Tip Heat Transfer*," Ann. N.Y. Acad. Sci., 934 (2001): 64-79.

[3] Mayle, R. E., and Metzger, D. E., ''*Heat Transfer at the Tip of an Unshrouded Turbine Blade*,'' Proc. Seventh Int. Heat Transfer Conf., Hemisphere Publishing, Washington, DC (1982): 87–92.

[4] Kline, S.J., and McKlintock, F.A., "*Describing Uncertainties in Single sample Experiments*," Mechanical Engineering, 75, Jan. 1953, pp. 3-8.

[5] Sjolander, S.A., and Cao, D., "*Measurements of the flow in an idealized turbine tip gap*," ASME J. Turbomach., 117 (1995): 578-584.

[6] K. Anto, S. Xue and W.F. Ng, L.J. Zhang and H.K. Moon, "*Effects of Tip Clearance Gap and Exit Mach Number on Turbine Blade Tip and Near-Tip Heat Transfer*," Proceedings of ASME Turbo Expo GT2013-94345.

[7] Bunker, R.S, Bailey, J.C., and Ameri, A.A, "*Heat Transfer and Flow on the First-Stage Blade Tip of a Power Generation Gas Turbine: Part 1-Experimental Results*," ASME J. Turbomach. Vol. 122 (2000): 263-271.

[8] Azad, G., Han, J.C., and Teng, S., "*Heat Transfer and Pressure Distributions on a Gas Turbine Blade Tip*," ASME J. Turbomach., Vol. 122 (200): 717-724.

[9] Zhang, Q., O'Dowd, D. O., He, L., Oldfield, M. L. G., and Ligrani, P. M., 2011, "*Transonic Turbine Blade Tip Aerothermal Performance with Different Tip Gaps- Part I: Tip Heat Transfer*," ASME J. Turbomach., Vol. 133(4), pp. 1-9.

[10] Kwak, Jae Su, Jaeyong Ahn, Je-Chin Han, C. Pang Lee, Ronald S. Bunker, Robert Boyle, and Raymond Gaugler. "*Heat Transfer Coefficients on the Squealer Tip and Near-Tip Regions of a Gas Turbine Blade with Single or Double Squealer*," Journal of Turbomachinery 125.4 (2003): 778-87.

[11] Azad, GM S., Han, J. C., Bunker, R. S., and Lee, C. P., ‘‘*Effect of Squealer Geometry Arrangement on a Gas Turbine Blade Tip Heat Transfer*,’’ ASME J. Heat Transfer, 124 (2002): 452–459.

[12] Azad, GM S., Han, J. C., and Boyle, R. J., ”*Heat Transfer and Flow on the Squealer Tip of a Gas Turbine Blade*,” Proceedings of ASME Turbo Expo 2000-GT-0195.

[13] Park, Jung Shin, Sang Hoon Lee, Jae Su Kwak, Won Suk Lee, and Jin Taek Chung, “*Measurement of Blade Tip Heat Transfer and Leakage Flow in a Turbine Cascade with a Multi-Cavity Squealer*,” Proc. of ASME 2013 Turbine Blade Tip Symposium and Course Week, Germany, Hamburg.

[14] Kwak, Jae Su, and Je-Chin Han, "*Heat Transfer Coefficients and Film Cooling Effectiveness on the Squealer Tip of a Gas Turbine Blade*," Journal of Turbomachinery 125.4 (2003): 648.

[15] Ameri, A. A., E. Steinthorsson, and D. L. Rigby. "*Effect of Squealer Tip on Rotor Heat Transfer and Efficiency*," Journal of Turbomachinery 120.4 (1998): 753-59.

[16] Mhetras, S., Narzary, D., Gao, Z., and Han, J. C., “*Effect of a Cutback Squealer and Cavity Depth on Film-Cooling Effectiveness on a Gas Turbine Blade Tip*,” ASME J. Turbomach., 130 (2008): 021002-1-021002-13

[17] Newton, P. J., Lock, G. D., Krishnababu, S. K., Hodson, H. P., Dawes, W. N., Hannis, J., and Whitney, C., “*Aerothermal Investigations of Tip Leakage Flow in Axial Flow Turbine – Part III: Tip Cooling*,” ASME J. Turbomach, Vol. 131 (2009): 011008-1-011008-12

[18] Key, N. L., and Art, T., "*Comparison of Turbine Tip Leakage Flow for Flat Tip and Squealer Tip Geometries at High-Speed Conditions*," ASME J. Turbomach, Vol. 128-2 (2006): 213-220.

[19] Zhou, C., and Hodson, H., “*The Tip Leakage Flow of an Unshrouded High Pressure Turbine Blade with Tip Cooling*,” ASME J. Turbomach, Vol. 133 (2011): 041028-1-041028-12.

[20] Naik, S., Georgakis, C., Hofer, T., and Lengani, D., “*Heat Transfer and Film Cooling of Blade Tips and Endwalls*,” ASME J. Turbomach, Vol. 134 (2012): 041004-1-041004-11

[21] Holmberg, D.G., and Diller, T.E., "*Simultaneous Heat Flux and Velocity Measurements in a Transonic Turbine Cascade*," ASME J. Turbomach., 127 (2005), 502-506.

[22] Nix, A.C., Diller, T.E., and Ng, W.F., "*Experimental Measurements and Modeling of the Effects of Large-Scale Freestream Turbulence on Heat Transfer*," ASME J. Turbomach., 129 (2007), 542-550.

[23] Smith, D.E., Bubb, J.V., Popp, O., Grabowski, H.C., Diller, T.E. Schetz, J.A. and Ng. W.F., 2000, "*Investigation of Heat Transfer in a Film Cooled Transonic Turbine Cascade, Part I: Steady Heat Transfer*," ASME 2000-GT-202.

[24] Popp, O., Smith, D.E., Bubb, J.V., Grabowski, H.C., Diller, T.E. Schetz, J.A. and Ng. W.F., 2000, "*Investigation of Heat Transfer in a Film Cooled Transonic Turbine Cascade, Part II: Unsteady Heat Transfer*," ASME 2000-GT-203.

[25] Carullo, J. S., Nasir, S., Cress, R. D., Ng, W. F., Thole, K. A., Zhang, L. J., and Moon, H. K., "*The Effects of Freestream Turbulence, Turbulence Length Scale, and Exit Reynolds Number on Turbine Blade Heat Transfer in a Transonic Cascade*," ASME J. Turbomach., 133 (2011), 011030.

[26] Nasir, S., Carullo, J.S., Ng, W.F., Thole, K.A., Wu, H., Zhang, L.J., and Moon, H.K., "*Effects of Large Scale High Freestream Turbulence, and Exit Reynolds Number on Turbine Vane Heat Transfer in a Transonic Cascade*," ASME J. Turbomach., 131 (2009), 021021.

[27] S. Xue, A. Roy, W. F. Ng and S. V. Ekkad 2014, "*A Novel Transient Technique to Determine Recovery Temperature, Heat Transfer Coefficient, and Film Cooling Effectiveness Simultaneously in a Transonic Turbine Cascade,*" ASME J. Thermal Sci. Eng. Appl., Vol. 7 (2014), No. 011016. doi: 10.1115/1.4029098.

[28] Moffat, R. J., 1988, "*Describing Uncertainties in Experimental Results*," Exp. Thermal and Fluid Science, 1988, pp. 3-17.

[29] Menter, F.R., "*Two-Equation Eddy-Viscosity Turbulence Models for Engineering Applications*," AIAA Journal, Vol. 32 (1994), No. 8, 1598-1605.

[30] H. Wu, S. Nasir, W.F. Ng, H.K. Moon, 2008, "*Showerhead Film Cooling Performance of a Transonic Turbine Vane at High Freestream Turbulence (Tu =16%): 3-D CFD and Comparison with Experiment.*" ASME International Mechanical Engineering Congress and Exposition, IMECE2008-67782

CHAPTER 3

An Experimental and Numerical Investigation of the Effect of Combustor-Nozzle Platform Misalignment on Endwall Heat Transfer at Transonic High Turbulence Conditions

A. Arisi, D. Mayo, Z. Li, W. F. Ng
Mechanical Engineering Department
Virginia Polytechnic Institute and State University
Blacksburg, VA 24061

H.K. Moon, L. Zhang
Solar Turbines Inc.
San Diego, CA 92101

ASME-IGTI Paper GT2016-57763

To be submitted to the Journal of Turbomachinery

ABSTRACT

A detailed experimental and numerical study has been conducted to investigate the endwall heat transfer characteristics on a nozzle platform that has been misaligned with the combustor exit resulting in a backward facing step at the nozzle inlet. The study was carried out under transonic engine representative conditions with exit Mach numbers of 0.85 and 1.0 (Re_{exit} = 1.5 x 10^6 and Re_{exit} = 1.9 x 10^6) respectively. A high freestream turbulence of 16% was set at the inlet located 0.48 chords upstream of the vane leading edge which is typical of turbulence conditions in a gas turbine engine. The experiment was conducted in a blowdown facility with a 2-D linear cascade and a transient infrared thermography technique coupled with endwall static pressure ports used to map the endwall surface heat transfer and aerodynamic characteristics respectively. A numerical study was also conducted by solving the steady state Reynolds Averaged Navier Stokes (RANS) equations using the commercial CFD solver ANSYS Fluent v.15. The numerical results were then validated by comparing to experiment data and good agreement

was observed. These CFD results provided further insight into the development and evolution of the near endwall secondary flows which explain the endwall heat transfer characteristics observed.

The results reveal that the presence of an upstream backward facing misalignment between the combustor exit and a flat nozzle endwall significantly influences the heat transfer characteristics on the nozzle endwall surface. The classical endwall secondary flows (endwall crossflows, horseshoe and passage vortices) are weakened but a unique auxiliary vortex system develops within the passage and interacts with the weakened horseshoe vortex. It is observed that heat transfer in the first half of the passage endwall is heavily influenced by this auxiliary vortex system. Heat transfer augmentation of between 15% and 40% was also observed throughout the NGV endwall. Furthermore, the auxiliary vortex system results in a delayed cross-passage migration of the horseshoe vortex which consequently results in large lateral gradient in heat transfer downstream of the throat. The reattachment length varied significantly ahead of the leading edge with all the upstream recirculating flow feeding into the development of the auxiliary vortex system which affected heat transfer throughout the passage. The overall effect of Mach/Reynolds number on endwall heat transfer and NGV stage aerodynamic losses is also explored in this study.

NOMENCLATURE

C True chord of vane (91.1 mm, 3.59 in)

C_{p0} Total pressure loss coefficient ($\boldsymbol{C_{p0} = \frac{P_{0_1} - P_{0_2}}{P_{0_1} - P_{s_2}}}$)

C_x Axial chord of vane (50.0 mm, 1.97 in)

h Convective heat transfer coefficient [W/m^2·K]

k Thermal conductivity [W/m·K]

M Mach number

NGV Nozzle Guide Vane

Nu Nusselt number (hC/k_{air})

P Pressure [Pa]

q Heat flux [W/m^2]

Re Reynolds number (based on chord length)

T Temperature [K]

t time [s]

Tu Turbulence intensity at cascade inlet

Greek Symbols

α Thermal diffusivity [m^2/s]

γ Specific heat ratio

ρ Density [kg/m^3]

Subscripts

1 Inlet conditions

2 Exit conditions

aw Adiabatic wall

i Initial conditions

r Recovery factor

s Static

t Total or stagnation

w Wall

∞ Mainstream

INTRODUCTION

In modern gas turbine engines, air is pressurized in a compressor, mixed with fuel and ignited in a combustor. This hot, pressurized gas then enters the turbine section where power is extracted for various applications. The power density of a gas turbine engine can be improved by increasing the turbine inlet temperature. As a result, the turbine inlet temperature is continually increasing beyond the blade material yield temperature.

The first stage nozzle guide vane endwall region of a gas turbine engine is exposed to extremely high gas temperature and turbulence conditions propagating downstream from the combustor. This results in very high heat loads and metal temperature on the endwall surface. In addition to these harsh conditions, heat transfer is further exacerbated by secondary flows that are generated near the endwall surface. In order to minimize this heat transfer exacerbation and aerodynamic losses due to secondary flows, it is desired to have a smooth transition between the combustor exit and the nozzle section.

However, it is often unavoidable to have misalignment between the combustor exit and endwall platform as the engine undergoes thermal transients or due to buildup of assembly tolerances. Recent engine designs have very compact combustors with flame temperatures exceeding the material yield temperature. As a result, the combustor exit liner is fitted with dilution holes which result in a varying thermal expansion that eventually increases the misalignment with the turbine platform. As such, it is invariably necessary to account for the heat transfer and flow characteristics induced by such misalignments in order achieve the desired engine life.

There has been a concerted effort to understand the nature of the near endwall secondary flows that form within the turbine passage. An early study by Herzig et al. [1] followed by works

from Goldstein et al. [2], and Sievrding et al. [3, 4] provided a detailed insight into the formation and development of secondary flows within the passage. These studies highlighted the presence of dominant secondary flows such as the cross passage flows, horseshoe and passage vortices. Langston et al. [5, 6, 7], and Wang et al. [8] further went on to characterize the nature of these passage vortices and their interaction within a turbine passage.

Since then, there have been numerous studies that have analyzed the characteristic of endwall heat transfer distribution as influenced by these secondary flows. Many of these studies, until recently have been carried out in scaled up low speed facilities. Kang et al. [9] investigated heat transfer and flow field characteristics around the leading edge region where the horseshoe vortices form, at various exit Reynolds number. The horseshoe vortex was noted to form closer to the leading edge and become more turbulent at lower Reynolds numbers. Graziani [10] analyzed the effect of inlet boundary layer thickness on endwall heat transfer. The author noted that the heat transfer range was unaffected by incoming momentum boundary layer thickness. However, the heat transfer imprint on the endwall due to the secondary flows was more visibly apparent for thicker inlet boundary layer. There was also less crossflow from the pressure side to the suction side along the endwall surface for a thin inlet boundary layer. This suggested that the size and strength of the horseshoe vortices is dependent on the size of the inlet boundary layer.

The effect of combustor exit conditions on heat transfer has also been of interest. Ames [11] compared the endwall heat transfer at low and high inlet turbulence conditions. The author found that at higher turbulence conditions, the larger scales resulted in less distinct secondary flow features. The effect of turbulence on heat transfer was less dramatics at high Reynolds numbers. Lynch et al. [12] investigated the effect of presence of combustor-turbine interface slot as well as mid-passage interface from which they noted that the midpassage

interface and upstream slot increased heat transfer immediately downstream. In another relatively similar study by Thrift et al. [13], the effect of this upstream slot orientation on heat transfer and film-cooling was investigated. The authors found that a slot orientation at angles less than 45^{o} caused minimal disturbance on inlet flow and better endwall cooling.

Another area of interest has been on the effect of endwall geometrical configuration. The effect of varying the endwall profile was investigated by Thrift et al. [14] and Saha et al. [15]. The authors compared the heat transfer for flat endwall and axisymmetric endwall profile. Endwall profiling was found to generally reduce the heat transfer levels due to weakening of the secondary flows. Piggush et al. [16] investigated an axisymmetric endwall heat transfer with leakage effects at the misalignments. The study revealed that there is gas ingestion at the slash faces despite coolant blowing and this augments heat transfer on the endwall surface due to local boundary layer removal. Laveau et al. [17] extended on the topic by looking at the effect of non-axisymmetric contouring. The authors noted a significant reduction in the passage vortex strength and heat transfer.

There is a need to account for compressibility and Mach number effects that actually exist in an actual gas turbine engine. This calls for testing at transonic conditions which presents a significant challenge in terms of data acquisition, processing and computational modeling. There are few studies in literature that have been conducted under these transonic conditions. Giel et al. [18] decoupled the Mach number, Reynolds number and turbulence effects on endwall heat transfer using transient liquid crystals technique. The author noted that there were shock effects on endwall heat transfer at high exit Mach numbers. Furthermore, the overall effect of having a passive turbulence grid in a transonic testing facility was that the peak heat transfer levels on the endwall were lowered. Arnab et al. [19] investigated the effect of having an

upstream purge slot with and without coolant injection and noted that the presence of the purge slot was the driving factor in influencing endwall heat transfer over coolant injection effects.

The inlet flow conditions effect on turbine endwall heat transfer under transonic conditions have also been investigated in a few studies. Boyle et al. [20] studied the effect of inlet boundary layer thickness and Reynolds number on a stator endwall heat transfer. The authors' findings were that the primary effect of the boundary layer thickness was only on the heat transfer magnitude and not the qualitative distribution. The cross passage flow was also greater at lower inlet Reynolds number. Barringer et al. [21] investigated the effect of the combustor exit profile of the total pressure and total temperature. Three kinds on total pressure profiles were investigated: A uniform profile, turbulent boundary layer shaped profile and profile with inflection near the endwall. The formation of counter rotating vortices within the passage was found to be dependent on the inflection profile and this resulted in higher heat transfer because the counter rotating vortex tended to move hotter fluid closer to the endwall.

From the preceding brief discussion it is clear that there is very limited material in open literature on nozzle endwall heat transfer at transonic conditions. This work seeks to contribute to the current literature by providing a detailed study on the effect of combustor-nozzle endwall misalignment effects at coupled engine presentative Mach/Reynolds number and turbulence conditions. For the first time in literature, the effect of inlet misalignment on heat transfer under transonic conditions has been isolated. With such data, designers can account for potential misalignments effects by strategically contouring the endwall and/or optimizing the turbine platform cooling design to mitigate the effects. Furthermore, this experiment data can also be used for numerical model validations at such conditions and as a basis for comparison for other misalignment studies.

EXPERIMENTAL SETUP

The current study was conducted at the Virginia Tech Transonic Wind Tunnel, which is a blowdown facility capable of producing isentropic exit Mach numbers as high as 1.2. This facility has been used in many previous heat transfer experiments including those by Anto [22], Holmberg [23], Nix et al. [24], Smith et al. [25], Popp et al. [26], Carullo et al. [27] and Nasir et al. [28]. Figure 3.1 shows a scale drawing of the transonic wind tunnel test facility.

An upstream compressor pressurizes air up to 1725 kPa (250 psig) in a high volume storage tank. A main control valve located upstream of the tunnel test section is capable of holding steady inlet pressure for up to 20 seconds, depending on the desired tank and inlet pressure. However, being a blowdown facility, the tunnel is thermally transient meaning that the inlet total temperature decreases with time during testing.

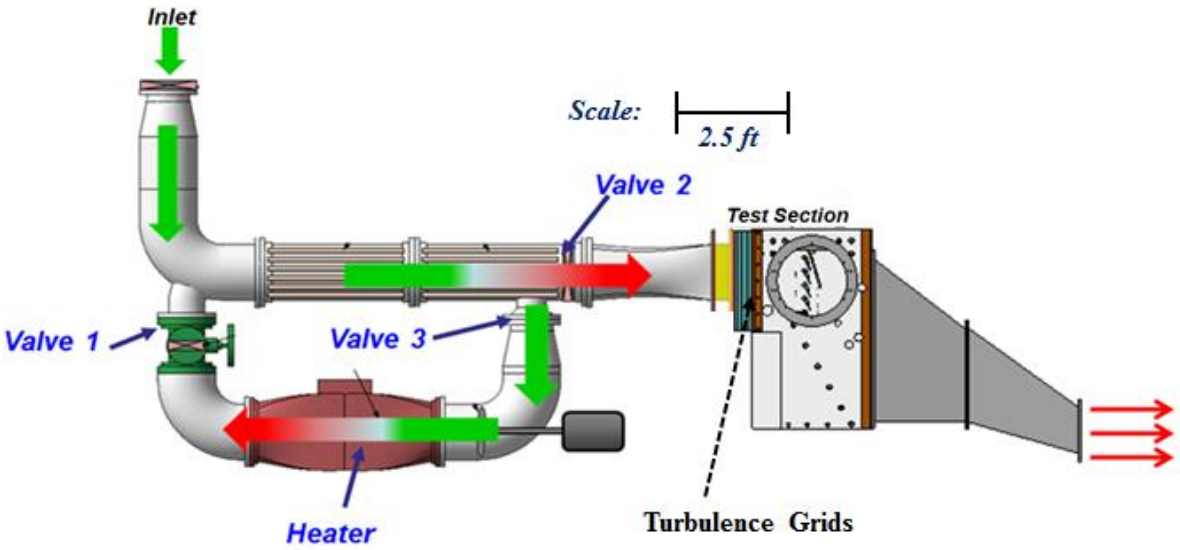

Figure 3.1: Scale representation of the Virginia Tech Transonic Wind Tunnel facility

Before a heat transfer test, valve 2 is closed and the heater and fan are turned on. This heats up the air and the copper rods in the heating loop. When air within the heating loop reaches ~115°C (240°F) valve 2 is opened and pressurized air passes through the copper rods heat exchanger into the test section via the turbulence grids. This passive turbulence grid with 48%

solidity generates a turbulence intensity of ~16% at the inlet, located 0.48 C upstream of the vane leading edge. The turbulence characteristics were measured using hotwire anemometry by Nasir et al. [28] and were also validated at the start of this research undertaking.

Figure 3.2 shows a detailed CAD view of the test section cascade. The test section consisted of five passages with four full vanes. The central passage (see Figure 3.2) was instrumented to obtain endwall pressure and heat transfer data. At the start of this research project, pressure data was collected at midspan of the vanes adjacent to the central passage to ensure that the flow was periodic. The dimensions for this cascade have been scaled up to 1.5 times the size of the actual engine geometry. The transition geometry was located 0.0434 m (0.48C) upstream of the leading edge. The step transition between the combustor exit and nozzle platform was also scaled appropriately from engine specs. A step height of 6.78 x 10^{-3} m (0.267 in) was used based on the average combustor exit and nozzle endwall mismatch.

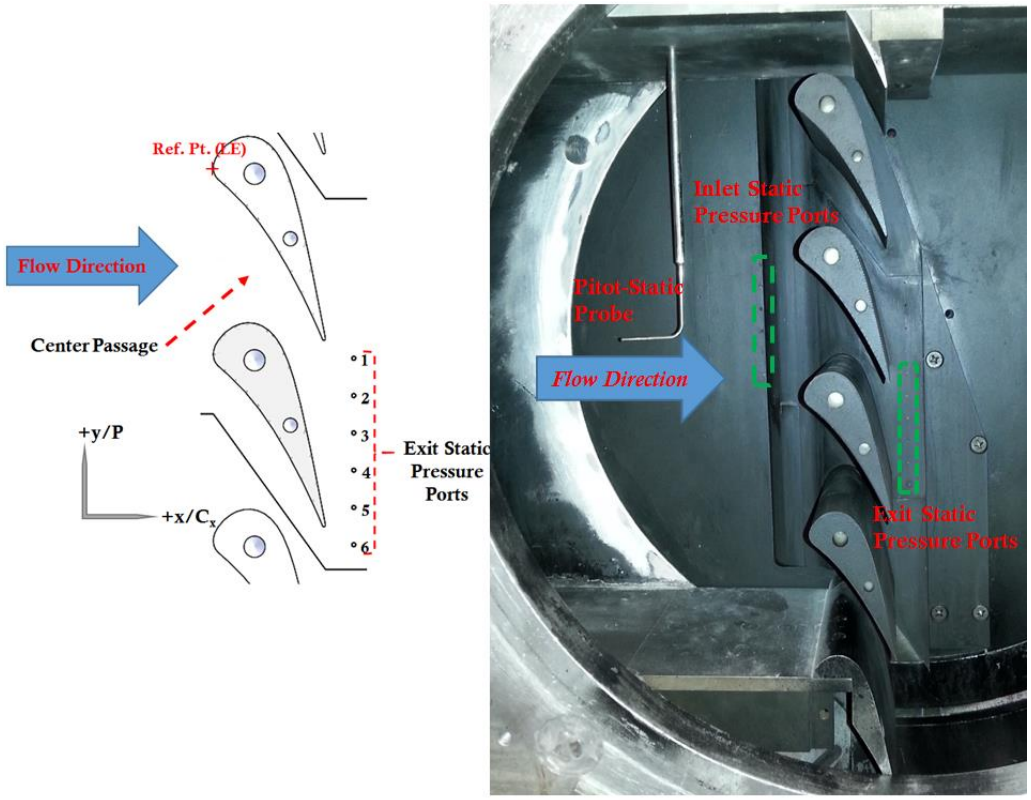

Figure 3.2: Vane cascade with endwall made of low conductivity ABS material.

The vanes and endwall were printed adjoined in ~~the~~ a Fortus 250mc three-dimensional printing machine by Stratasys using ABS P-430 material which has a low thermal conductivity of 0.188 W/(m-K). The printed endwall extended approximately 0.0434 m (~0.48 C) upstream of the leading edge, which coincides with the turbine section inlet plane. This configuration allowed for different engine representative NGV endwall profiles to be tested in this test section. A slot located one chord upstream of the vane leading edge was used to ascertain the inlet total temperature and total pressure profiles as well as the turbulence conditions. A summary of the cascade test section and the endwall configurations are shown in Table 3.1 and Figure 3.3 respectively.

Table 3.1: Vane Cascade Properties

Chord, C	91.2 mm
Axial Chord, C_x	50.0 mm
Pitch, P	83.1 mm
Entry Step Height	6.78 mm
Exit Isentropic Mach Number, M_2	0.60, 0.85 (design), 1.0
Inlet Turbulence Intensity, Tu_1	16%

CONFIGURATION NAME	CAD Illustration
FLAT COMBUSTOR-NOZZLE TRANSITION with FLAT PASSAGE ENDWALL (BASELINE)	
STEP COMBUSTOR-NOZZLE TRANSITION with FLAT PASSAGE ENDWALL	

Figure 3.3: CAD model illustration of the endwall configurations investigated

DATA REDUCTION TECHNIQUE

A linear regression technique was used to calculate the heat transfer coefficient on the endwall platform surface. This linear regression method was developed by Xue et al. [29] and allows for the simultaneous resolution of the surface heat transfer coefficient and recovery temperature. Using Newton's Law of Cooling, the convective heat flux q_w, is defined as in Equation 3.1, where T_r is the recovery temperature, T_w the wall temperature and h is the local heat transfer coefficient. For compressible flows, T_r is the driver temperature which is an adjusted value of the mainstream total temperature to account for friction heating and thermal dissipation due to transonic conditions.

Equation 3.1 can be re-expressed in a linear form, (see Equation 3.2), based on the fact that the Virginia Tech transonic tunnel conditions are aerodynamically steady but thermally transient during data collection. The temperatures in this equation are then normalized using the measured upstream total temperature T_t. The wall temperature, T_w, is measured with a calibrated FLIR A325 infrared camera at a frequency of 10 Hz. The recovery temperature, T_r, is calculated using Equation 4, where r_c is the local recovery factor, M is the local Mach number, γ is the specific heat ratio of air and $T_{t,\infty}$ is the mainstream total temperature. The term in parenthesis, represented as C_r, is not known at every location across the endwall surface. The value of C_r is dependent on the Mach number only, as shown in Equation 3.4 and introduced into Equation 3.3, and is therefore a constant at a particular point during the data reduction time window. The heat transfer coefficient can be determined from the slope of the regression line and the recovery temperature from the y-intercept. Further details on the regression method can be referred to in Xue et al. [29].

$$q = h(T_r - T_w) \tag{3.1}$$

$$\frac{q}{T_t} = h\frac{T_r}{T_w} - h\frac{T_w}{T_t} \tag{3.2}$$

$$\frac{q}{T_t} = hC_r - h\frac{T_w}{T_t} \tag{3.3}$$

$$y = C + mx$$

$$T_r = T_{t,\infty}\left(\frac{1+r_c\frac{\gamma-1}{2}M^2}{1+\frac{\gamma-1}{2}M^2}\right) = T_{t,\infty}C_r \tag{3.4}$$

The final unknown term in the linear regression equation is the convective heat flux, q''_w. The heat flux was calculated using the Cook-Felderman method (Equation 3.5) which assumes semi-infinite and one-dimensional heat conduction with uniform initial temperature throughout the domain. The output heat flux of this method is very similar to that obtained using a finite-difference technique. However, the Cook-Felderman method is more computationally efficient than the finite difference method.

$$q(t_n) = \frac{2\sqrt{k\rho C_p}}{\sqrt{\pi\Delta t}}\sum_{j=1}^{n}\frac{T_j - T_{j-1}}{\sqrt{n-j}+\sqrt{n+1-j}} \tag{3.5}$$

The uncertainty of this study was calculated using a two part method that consisted of the perturbation technique proposed by Moffat [30] and the regression uncertainty technique proposed by Brown et al. [31]. In the first part which involved calculating the heat flux uncertainty using the perturbation method, the random IR camera error was the significant factor. The average uncertainty in heat flux was found to be approximately $\pm$6.3%. This uncertainty together with that for the upstream total temperature thermocouple was then used in the regression uncertainty calculation. An overall Nusselt number (heat transfer coefficient) uncertainty of $\pm$9.6% was calculated. It is worth noting that this uncertainty is only valid in regions where the one dimensional semi-infinite heat conduction assumption is valid. However, this assumption breaks down around the edges of the printed part and intersecting corners; therefore the uncertainty in these regions is much higher.

NUMERICAL METHOD

Solver and Turbulence Models

In this study, the Reynolds-Averaged Navier Stokes Equations were solved using the commercial CFD solver ANSYS *Fluent 15.0*. A pressure-based steady-state solver was used. An extensive study was conducted to determine the best suited model for prediction of the endwall heat transfer. The complexity of the endwall secondary flow at high speed and high turbulence conditions poses a significant challenge in prediction of the heat transfer. It was determined, as will be shown later, that the Reynolds Stress Model (RSM) was best suited for predicting the endwall heat transfer. Compressibility effects, curvature correction and viscous heating effects were accounted for in the model. Air was used as the working fluid and was modelled as an ideal gas. Viscosity, conductivity and specific heat of the fluid were modelled using molecular kinetic theory. The coupled turbulence algorithm was applied and a second order or higher upwind advection scheme was used to solve the flow variables.

Computational Domain and Boundary Conditions

Figure 3.4 shows the computational domain and the endwall, vane and periodic surface mesh. A multi-block structured grid was generated using the commercial meshing software *Pointwise v.17*. A total of ~5.5 million cells were used to resolve the domain after grid dependency study had been performed. The maximum y+ value on the endwall surface was y+ = 0.485 which ensures that the viscous sub layer in the boundary layer was well resolved on the endwall surface flow.

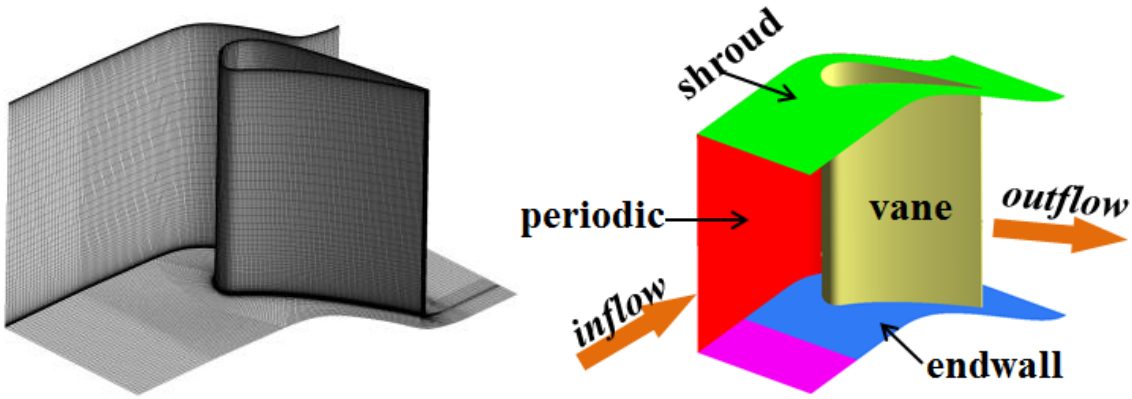

Figure 3.4: The CFD computational domain

Heat Transfer Prediction Methodology

The heat transfer coefficient was determined using a two simulation technique. This technique involves executing a first simulation with adiabatic wall conditions on the surfaces. This way, the adiabatic wall temperature (T_{aw}) is determined. In the second simulation, a uniform wall temperature or surface heat flux was applied. For this study, the second simulation was carried out with a uniform wall temperature 300 ^{o}K and the corresponding wall heat flux (q) was found. The heat transfer coefficient was then calculated from Equation 3.6.

$$h = \frac{q}{T_{aw} - T_w} \tag{3.6}$$

RESULTS AND DISCUSSION

Numerical Model Validation

The numerical model used in prediction of the heat transfer results presented throughout this paper was selected after an extensive analysis of various turbulence models. It was desired to effectively resolve the boundary layer flow and therefore turbulence models that rely on wall functions were not analyzed. A total of four turbulence models were investigated: Realizable k-epsilon, standard k-omega, Transition-SST and Reynolds Stress turbulence models. The predicted endwall heat transfer distribution results are shown in Figure 3.5 below.

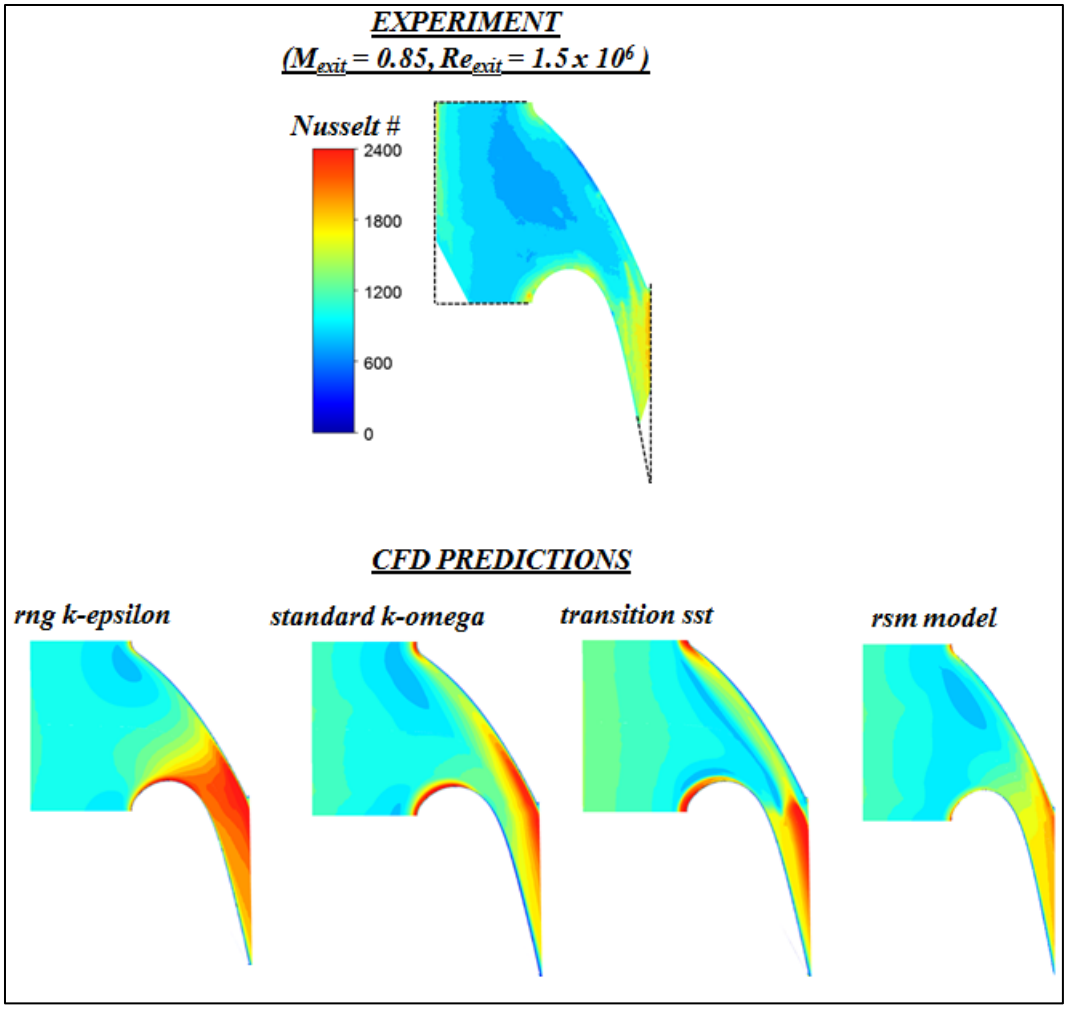

Figure 3.5: Endwall heat transfer distribution predicted by various turbulence models

An even better qualitative comparison of the heat transfer prediction is shown in Figure 3.6 where the heat transfer along the mid-passage stream is compared to experiment results. A significant difference in the prediction results exist in the passage downstream of the throat. With the exception of the rsm model, the CFD results over predict the level of heat transfer even though similar trends in this regions is observed between the k-omega, transition SST and rsm turbulence models. The rng k-epsilon shows very different heat transfer trend downstream of the throat compared to the experiment. From this investigation, the rsm turbulence model was selected and all the numerical results presented in this paper are based on this turbulence model results.

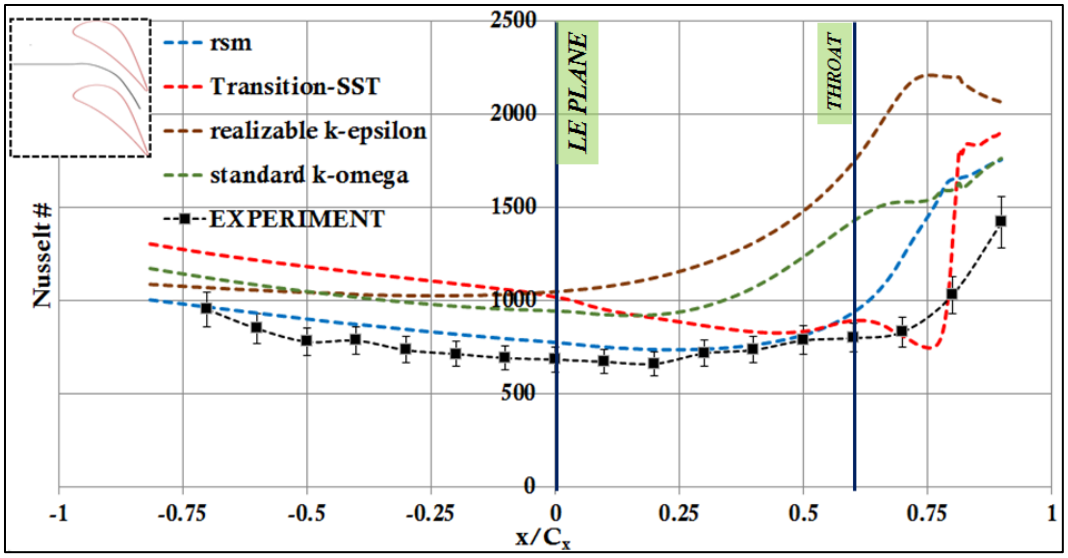

Figure 3.6: Comparison of the flat endwall heat transfer prediction along the mid-passage streamline (shown inset) at $M_{exit} = 0.85$ ($Re_{in} = 3.5 \times 10^5$)

Endwall Flow Field Characteristics

This section analyses in detail the flow characteristics near the endwall surface. While the classical endwall secondary flows for a flat endwall have been thoroughly investigated and understood, it is of interest to understand the nature of the endwall surface flow that arises due to the presence of an upstream step.

Figure 3.7 shows a comparison of the endwall static to total pressure ratio as measured from the experiment and predicted using CFD. Also shown in Figure 3.8 is the nature of the surface flow streamlines for the flat endwall (baseline). The results show very good aerodynamic agreement with the classical flat endwall secondary flow features i.e. pressure side and suction side horseshoe vortices. This flat endwall flow is briefly described in the next paragraph to set the stage for a detailed discussion on the effect of introducing an upstream step.

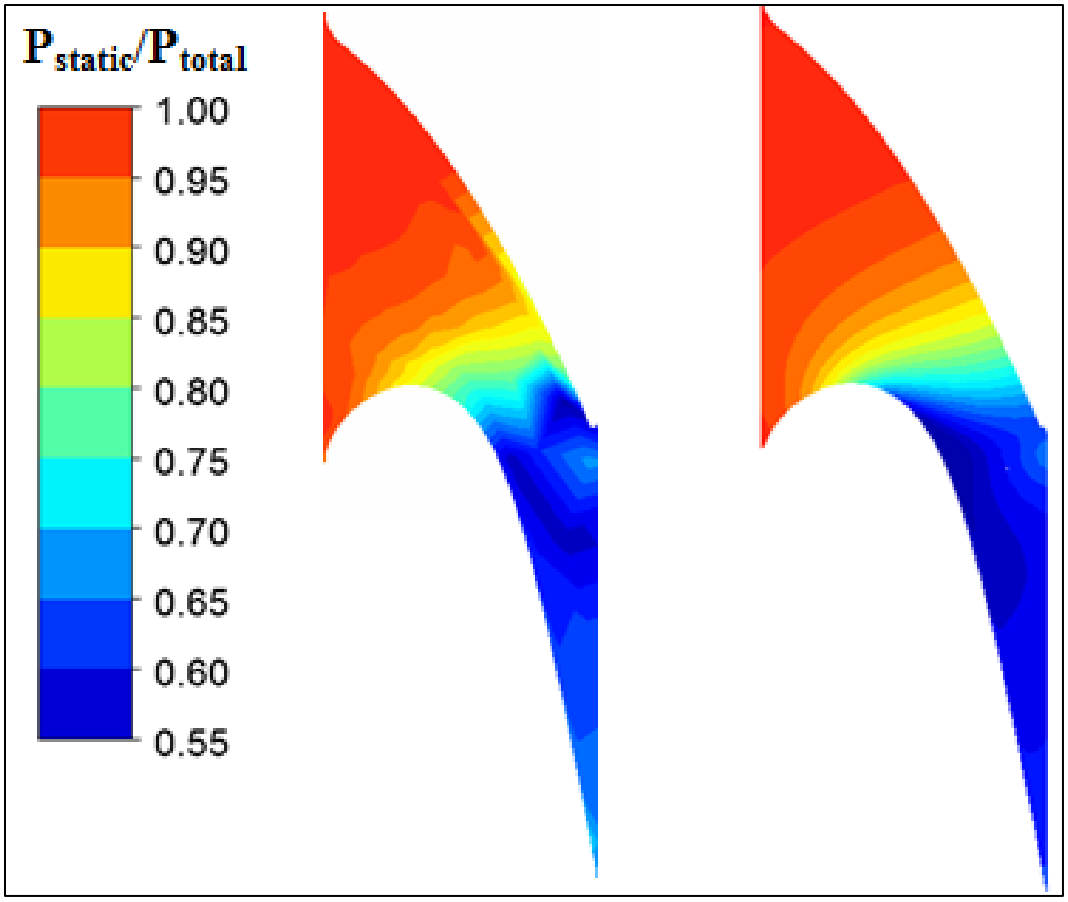

Figure 3.7: Endwall static to total pressure ratio distribution at M_{exit} 0.85

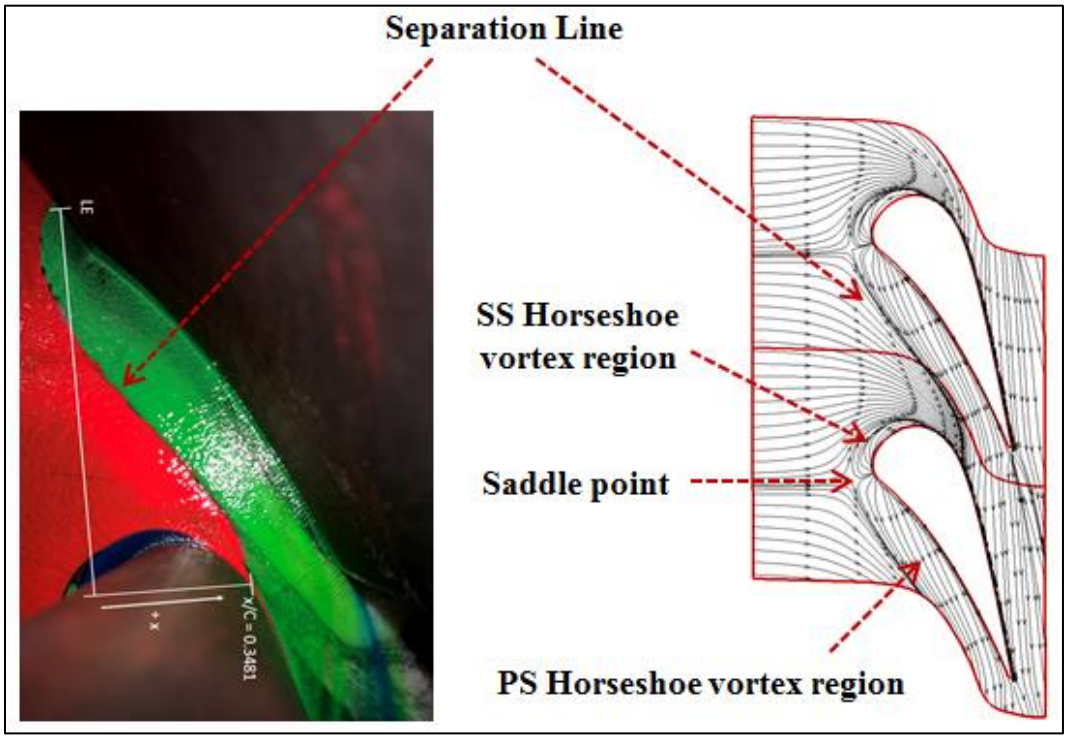

Figure 3.8: Flat endwall surface flow from experiment oil flow visualization and CFD surface streamlines

The flow characteristics on a flat endwall are dominated by the pressure and suction side legs of the horseshoe vortex. As the incoming boundary layer approaches the vane leading edge, it is gradually stagnated and the low momentum fluid within the boundary is the first to be stagnated. Due to this radial gradient in momentum, the boundary layer rolls up into a vortex widely known as the horseshoe vortex. A saddle point is formed where the reverse flow meets the approaching flow and the horse shoe vortex splits into a pressure side and suction legs as shown in Figure 3.8 above. The suction side leg wraps around the suction surface briefly and due to the strong flow acceleration on this surface, it is quickly lifted off the endwall surface and its effect on endwall flow disappears at around $x/C_x \sim 0.25$. On the other hand the pressure side leg ingests the incoming boundary layer fluid creating a separation line. This separation line divides the flow into what Spencer et al. [32] referred to as upstream and downstream endwall crossflow regions.

Downstream of this separation line a new boundary layer is formed that is three dimensional in nature due to strong axial and transverse pressure gradients in this passage region as seen from the endwall static pressure distribution in Figure 3.7. The three dimensional nature of this newly formed boundary layer coupled with the strong flow acceleration near the throat explains the large differences in CFD prediction of heat transfer around this region between the two equation turbulence models and the rsm turbulence model. Instead of resolving the turbulent stresses, the two equation models rely on an isotropic turbulent stress tensor assumption for closure and heat transfer prediction. While this closure model is sufficient where the boundary layer is predominantly two dimensional, it results in excessive heat transfer prediction in predominantly three dimensional boundary layers where the actual turbulent stresses are anisotropic.

The cross passage migration of the pressure side leg is gradual at first before a sudden migration to suction side at around $x/C_x \sim 0.65$ which coincides with the throat location. This is because of the endwall surface pressure distribution imposed by the vane. Figure 3.9 shows a comparison of the endwall surface flow between the flat endwall and a flat endwall with an upstream step included. Even though the step is located approximately 0.48 Chords upstream of the leading edge, it results in significant distortion of the classical endwall secondary flow. The saddle point for the step configuration is much closer to the vane leading edge compared to the flat configuration. This suggests that there is a significant reduction in the horseshoe vortex size which is further supported by the fact that, for the step configuration, the suction leg of the horseshoe vortex is nearly non-existent in Figure 3.9 below. Furthermore, the separation line is closer to the vane pressure side. This makes sense and should be expected because the size of the horseshoe vortex is dependent on the size of the incoming momentum boundary layer. With the separation induced by the step, this boundary layer is destroyed and is very thin after the flow reattachment.

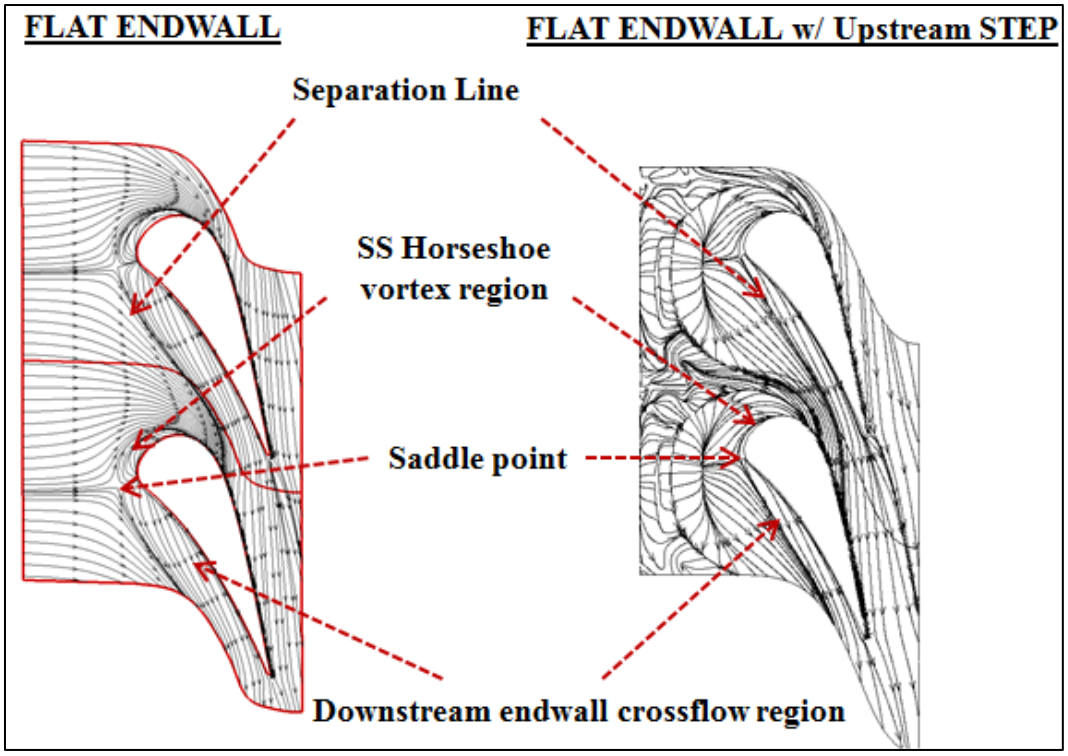

Figure 3.9: Near endwall surface streamlines for flat and step configurations at M_{exit} = 0.85

While flow separation after a backward facing step has been extensively studied in literature, its effect in a transonic nozzle cascade is largely unexplored. The findings of this study indicate that it has a first order effect on the passage flow throughout the cascade. In fact, it appears that the flow never reattaches at around y/P ~ 0.30 because of the radial gradients caused by the vane leading edges. The separated flow on either side of this pitch location feeds into this region creating a high speed separated flow into the passage. This flow creates two separation lines that divides the near suction side flow from the near pressure side flow. The fluid between these two separation lines is fed from the separation vortices that form after the step across the pitch. It can also be seen that as a consequence, the cross-passage migration of the pressure side leg of the horseshoe vortex occurs much deeper in the passage closer to the exit at x/C_x ~ 0.80. The yaw angle of the exiting streamlines are much further reduced downstream of the throat for a step configuration versus a flat configuration. Therefore, it can further be inferred that the three

dimensional nature of the passage endwall boundary layer is significantly reduced by the addition of an upstream step.

Heat Transfer Results

This section delves into the characteristics of the endwall surface heat transfer distribution for a step configuration compared to the flat configuration. The heat transfer distribution will be discussed and the complex near surface flow characteristics used to explain the heat transfer characteristics noted.

Figure 3.10 shows the endwall heat transfer distribution on a flat and step endwall configurations from both experiment and CFD at M_{exit} = 0.85 (Re_{exit} = 1.45 x 10^6). There are significant differences in heat transfer distribution across the nozzle stage due the perturbation of the inlet configuration. For a flat configuration, heat transfer is largely uniform approaching the nozzle passage. There is a wedge shaped low heat transfer region at the passage entrance (Region X, Figure 3.10) bounded by the suction and pressure side legs of the horse shoe vortex. This region is associated with low speed fluid with a thick boundary layer which results in low heat transfer. This wedge shaped region culminates at about x/C_x ~ 0.65 which coincides with the location of rapid horseshoe vortex migration to the suction side as discussed earlier. The high heat transfer distribution downstream of the throat (Region Y, Figure 3.10) is due to the combined effect of new boundary layer formation and flow acceleration at the throat.

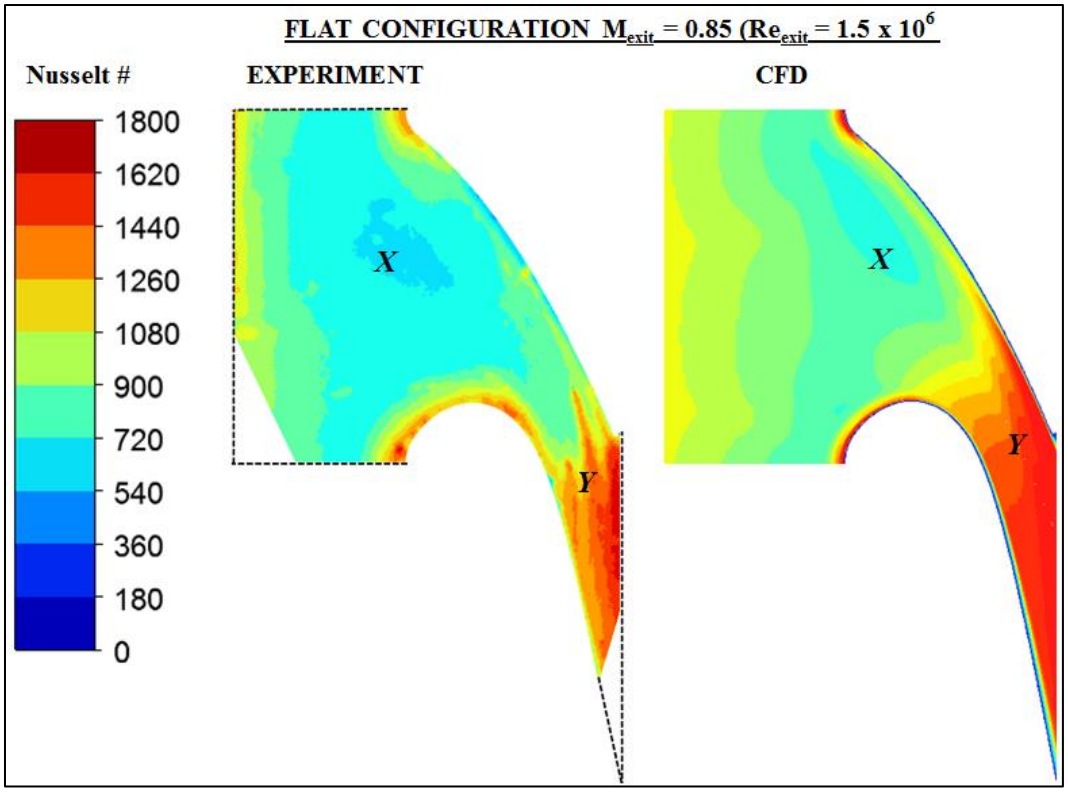

Figure 3.10: Endwall heat transfer distribution for the flat endwall configuration

Figure 3.11 shows the endwall heat transfer distribution for the step configuration. The experiment result and CFD prediction show very similar heat transfer characteristics, although the features in the CFD result are more distinct. The step causes steep gradients in the spatial heat transfer distribution. The high heat transfer imprint on the endwall due to the horseshoe vortices is very small. This is due to the smaller size of these vortices caused by the step. The uniform low heat transfer distribution upstream of the passage disappears and instead, high heat transfer regions are created ahead of the leading edge due to flow reattachment after the step and new boundary layer formation.

It is interesting to note that the size of the low heat transfer region created after the step (Region A, Figure 3.11) varies in the pitchwise direction and extends far into the nozzle passage at y/P ~ 0.30. The flow separation and reattachment after the step pushes the low heat transfer wedge shaped region, which was observed in the flat configuration, closer to the pressure side

(Region C in Figure 3.11). Furthermore, the heat transfer around the throat region and downstream is very non-uniform with steep lateral thermal gradients for the step configuration. Even though the peak heat transfer in this region is comparable to the flat configuration, the step configuration shows lower heat levels than the flat configuration which was unexpected. In fact, the high heat transfer is restricted to near the pressure side close to the trailing edge, before dropping rapidly across the passage towards the suction side. A detailed look at the passage flow field shows very unique flow characteristics throughout the passage due to the upstream step. The upstream step results in an auxiliary vortex system within the passage that plays a central role in the preceding unique observations and this is discussed in detail in the subsequent section.

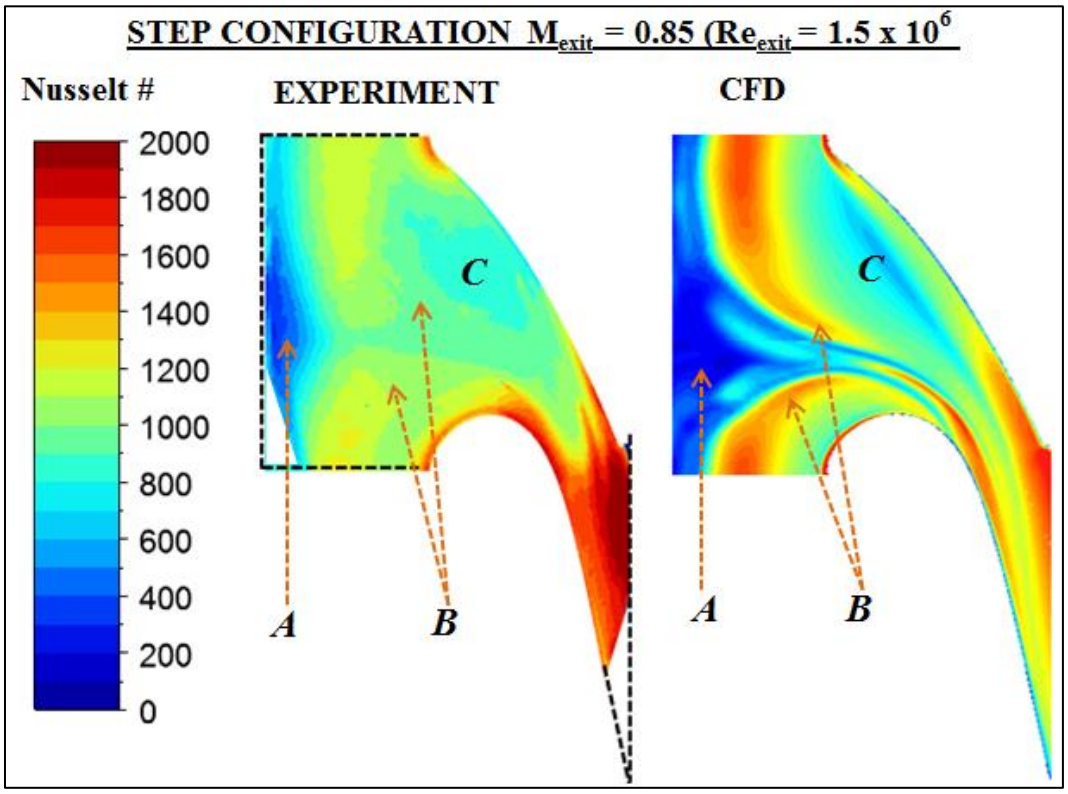

Figure 3.11: Endwall heat transfer distribution for the step endwall configuration

Step Induced Auxiliary Vortex System

In this subsection, the evolution of the separated flows behind the step into an auxiliary vortex system that propagates though the passage is analyzed. Figure 3.12 shows the separation and

reattachment of flow behind the step and ahead of the leading edge. The double separation vortex system observed ahead of the leading edge is typical of flow over a backward facing step. However, the presence of the vane potential field induces a finite helicity to the recirculation behind the step. Because there exist both a lateral and axial pressure gradients, these separation vortices migrate radially towards the mid-pitch region and the reattachment region narrows and shifts axially further into the passage.

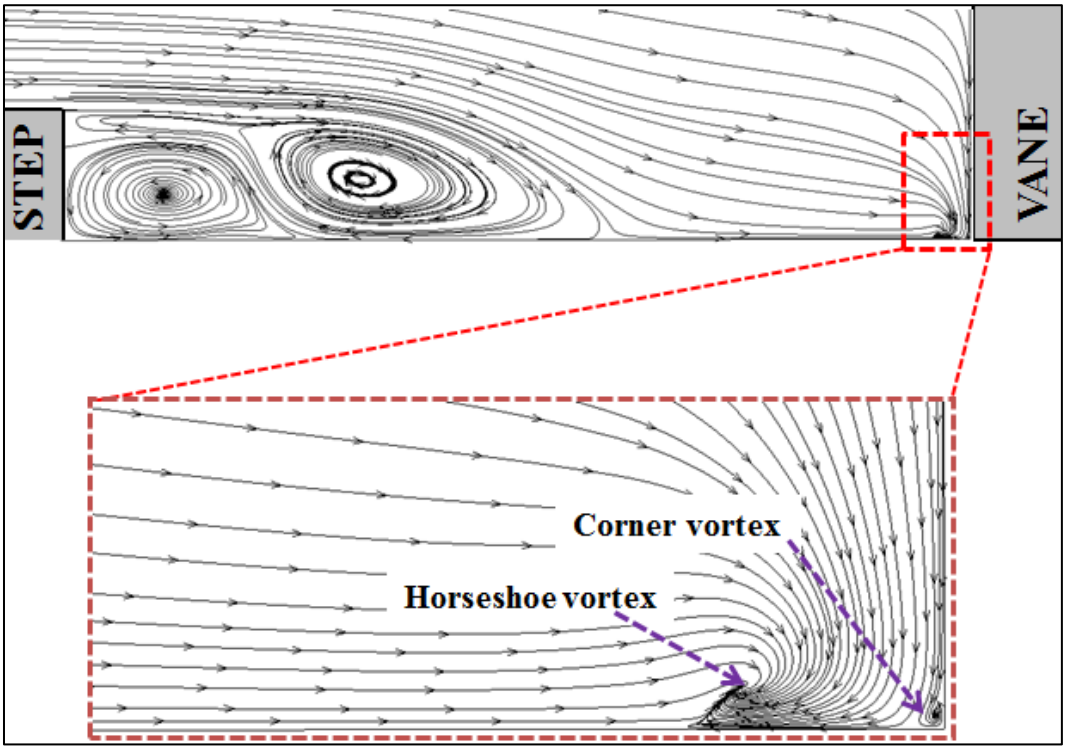

Figure 3.12: Separation flow behind the step and horse shoe vortex formation ahead of the leading edge

The two separation vortices which form ahead of the leading edge meet at about y/P ~ 0.30. The lateral and axial pressure gradients turn these separation vortices such that their vorticity axis aligns to the local streamwise flow resulting in a triple vortex system as shown in Figure 3.13. However, the two stronger vortices weaken and dissipate the smaller vortex and the system degenerates into a dual auxiliary vortex system.

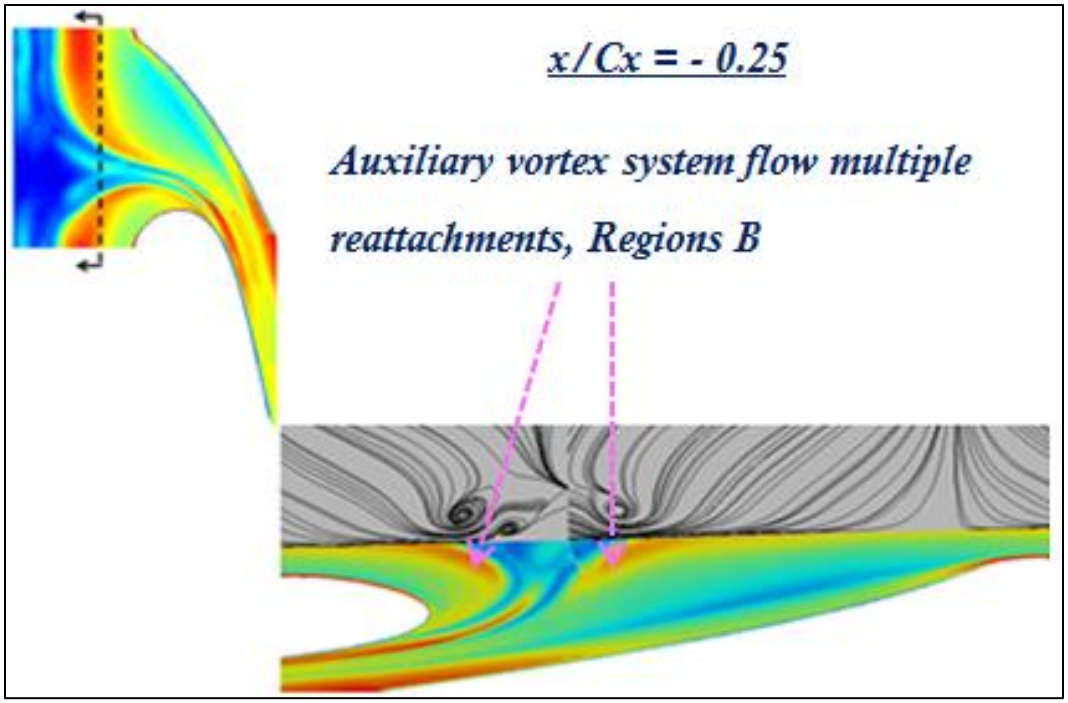

Figure 3.13: Auxiliary vortex system near the endwall surface on a plane $x/C_x = 0.25$ ahead of leading edge

This auxiliary vortex system significantly alters the heat transfer distribution on the NGV endwall step configuration compared to the flat configuration. It acts as a wedge dividing the reattachment region. On either side of the vortex core, there is high heat transfer region (Region B in Figure 3.11 and 3.13) as separated flow from the step is reattaching much further/deeper into the passage albeit under the influence of the dual auxiliary vortex system. This is surprising and unexpected that the reattachment region from the step extends as far as $x/C_x \sim 0.40$ into the passage, driven by this auxiliary vortex system.

Moving into the passage, the dual vortex system further dissipates into a single auxiliary vortex with the stronger leg coming over the suction side weakening that from the pressure side. This can be seen in Figure 3.14 below. Because the flow acceleration is stronger near the suction side, the near suction side vortex in the auxiliary system is dominant.

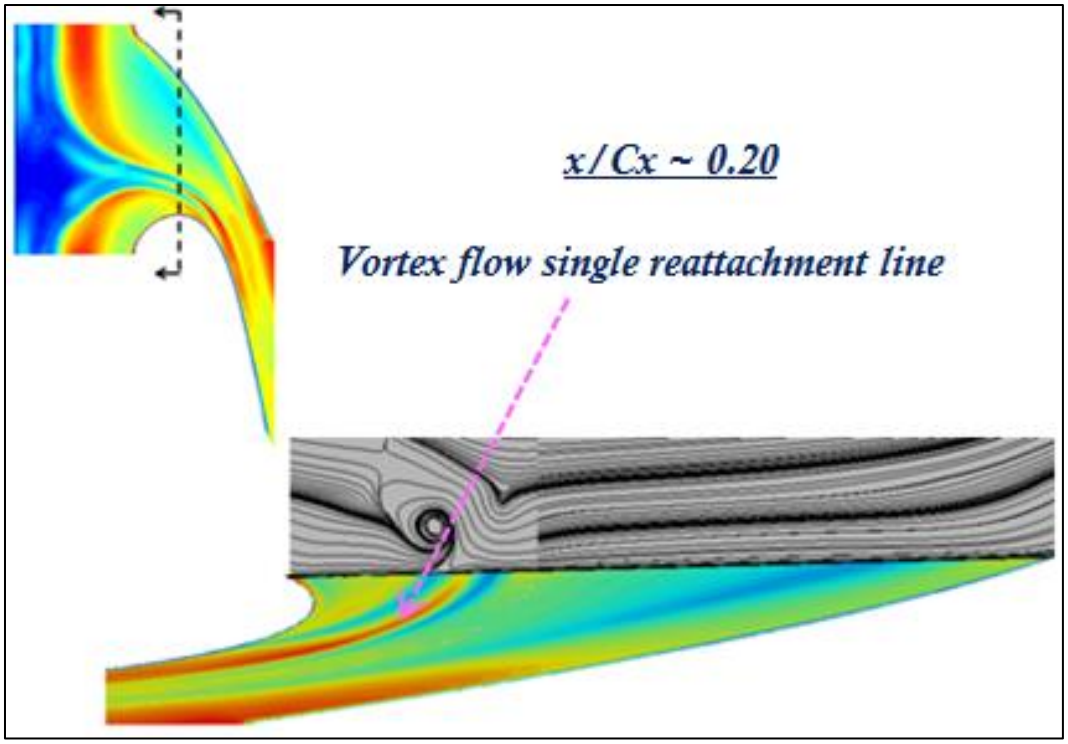

Figure 3.14: Auxiliary vortex system development in the nozzle passage, shown on a plane $x/C_x = 0.20$

Heat Transfer Downstream of the Throat

Within the NGV passage, the heat transfer at the throat region and downstream is of extreme interest to turbine designers. In this region, the flow reaches the highest Mach number, the boundary layer is thinner, and there is high turbulence production which results in very high heat transfer. It is worth noting that the heat transfer level and distribution at the throat region differs significantly between the flat and step configurations (refer to Figure 3.10 and Figure 3.11). In general the heat transfer is higher and uniform for the flat configuration. The step configuration shows high heat transfer level only close to the pressure side and lower heat transfer levels in the lateral direction for the rest of the passage downstream of the throat. These differences are linked to the upstream step in the following two ways.

First, the destruction of the momentum boundary layer by the upstream step causes the pressure side leg (and subsequent passage vortex) to be smaller. As a result, the heat transfer imprint on the endwall due to the horseshoe vortex is diminished and marginal. Secondly, the

auxiliary vortex system that forms within the passage becomes the dominant factor on endwall heat transfer imprint. It restricts the horseshoe vortex close to the pressure side and delays its cross-passage migration as was noted in the earlier discussion (reference Figure 3.9). As a result, the endwall cross flow and flow yaw angle is diminished for the step configuration compared to the flat configuration because the new boundary layer forming around the throat region is generally two-dimensional for the step configuration and restricted to the pressure side region.

It is important to note that since the cross-passage migration is delayed, the new boundary layer formation is restricted to close to the pressure side for most of the passage endwall. Consequently, the boundary layer downstream of the throat for the step configuration is predominantly two dimensional which is also evidenced by the small yaw angles. These effects combined explain the strong lateral heat transfer variation for the step configuration while that for the flat configuration is generally uniform.

Figure 15 shows the general heat transfer augmentation on the nozzle endwall. The augmentation factor was calculated along three passage streamlines shown inset in Figure 3.15. It can be seen that, apart from the region just behind the step, there is positive heat transfer is augmented throughout the passage due to the step. The highest heat transfer augmentation of about 40%-50% occurs at the flow reattachment region after the step. Within the passage, the augmentation is highest near the suction side and mid-pitch region (approximately 20%-40%) due to flow reattachment and the auxiliary vortex system. Heat transfer augmentation is lowest near the pressure side at about 10% and this is because for both configurations, this region is influenced by the pressure side leg of the vortex.

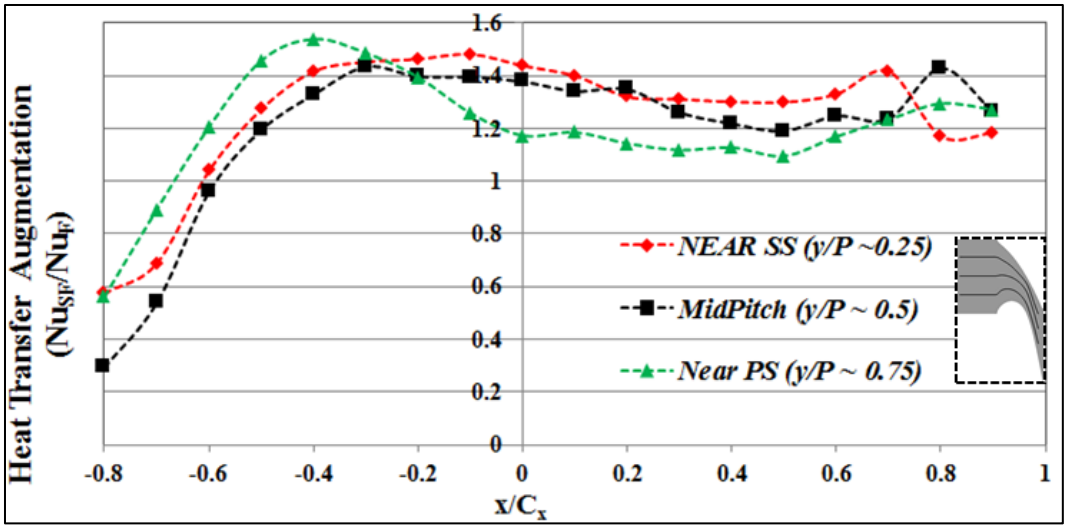

Figure 3.15: Heat transfer augmentation on the platform surface due to combustor-nozzle misalignment

Effect of Exit Mach/Reynolds Number

This section briefly presents the effect of coupled exit Mach/Reynolds number on the endwall heat transfer and NGV stage aerodynamic losses. This data is especially useful in off-design engine operation such as during transients and/or load following.

Figure 3.16 shows the variation of endwall heat transfer distribution across three exit Mach numbers. The heat transfer generally increases across the endwall as the exit conditions are elevated. However, the spatial size of the reattachment and separation regions remains unchanged. The highest heat transfer augmentation occurs at the reattachment regions ahead of the leading edge by as much as 23.0%. At sonic exit conditions, the oblique shock effect on the local endwall heat transfer is notable. In this study, this shock effect on heat transfer was notable for the step configuration but not for the flat configuration at the same sonic exit condition.

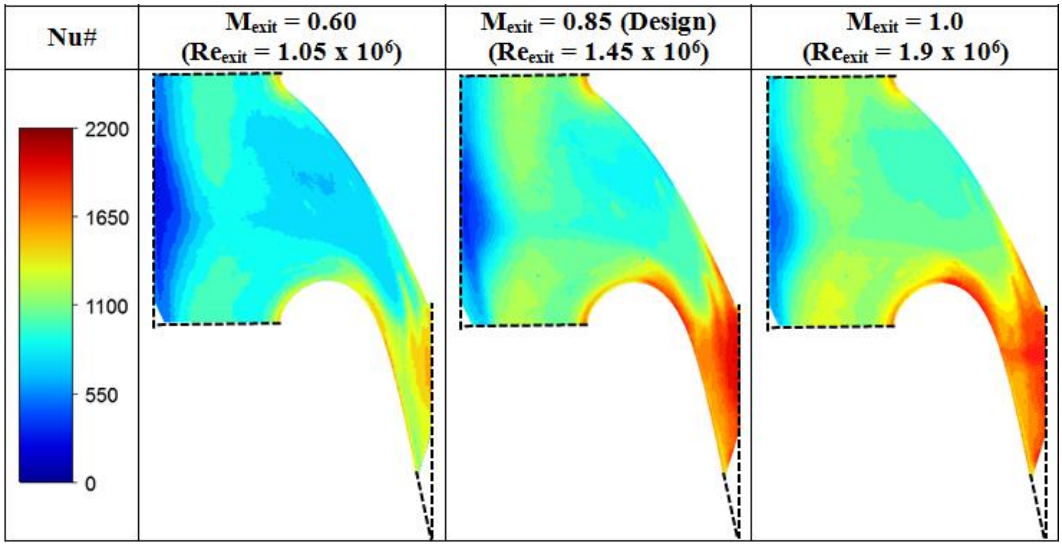

Figure 3.16: Variation of endwall heat transfer distribution across three Mach numbers

Finally, Figure 3.17 shows the variation of NGV stage aerodynamic losses with changes in exit conditions for both the flat and step configurations. At any given exit condition, the step configuration as a higher stage loss compared the flat configuration but the differences increases with exit Mach/Reynolds number. At design exit conditions, the difference in loss coefficient is ~37%. The loss coefficient is for the flat configuration remains relatively constant while that for the step configuration increases linearly. Recall that the step results in weaker horseshoe vortices within the passage and therefore, this suggests that the losses due to the step recirculation and the auxiliary vortex system dominate the losses caused by the horse shoe vortices.

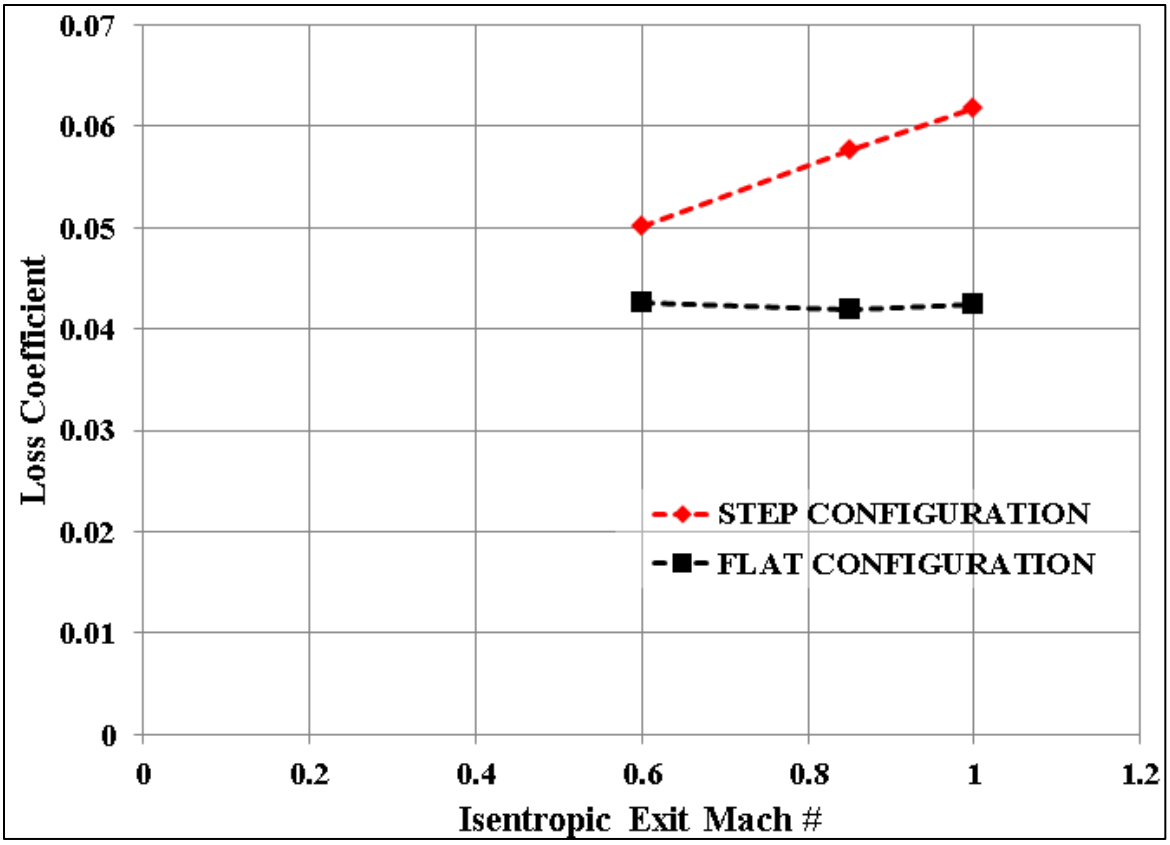

Figure 3.17: Variation of the loss coefficient at the exit of NGV passage across three Mach numbers

General Remarks

So far, this study has provided insight into the nature of the flow and heat transfer across the endwall surface induced by an upstream combustor-NGV endwall misalignment. Particularly interesting is that nearly all the recirculating flow after the step has a lateral helicity and feeds into the mid-passage auxiliary vortex system. In the actual gas engines, it is normal for coolant to be injected at the corner of the step. Aside from preventing hot gas ingestion, this coolant is likely to have a marginal effect on uniformly cooling the passage endwall after reattachment. Instead, it might be beneficial to use some of this coolant on carefully designed cooling configuration around the flow reattachment regions. It also remains to be seen how this coolant injected at the combustor-NGV endwall gap and addition of endwall contours weakens the auxiliary vortex system.

CONCLUSIONS

This paper has presented a detailed study on the heat transfer and flow characteristics on a nozzle endwall platform under land based gas turbine engine representative conditions. Using experimental data and numerical prediction, the effects of combustor-nozzle transition misalignment in the form of a backward facing step on endwall aerothermal characteristics was analyzed. The heat transfer distribution on the endwall platform with and without the upstream steam was measured under transonic high turbulence conditions in a linear cascade. Numerical results were also used to shed light into the flow characteristics that explain the heat transfer distributions observed. The following is a summary of the key findings.

The heat transfer for a flat configuration is governed by the classical endwall secondary flows i.e. the horseshoe and passage vortices. However, by having a step configuration, the horseshoe and passage vortices are severely weakened and heat transfer distribution on the NGV endwall is affected by the aft-step flow recirculation and an auxiliary vortex system which moves through the passage. Heat transfer augmentation is as high as 50% was observed at the flow reattachment regions ahead of the vane leading edge. The augmentation within the passage was between 20%-40% and close to the suction side due to the presence of the auxiliary vortex system.

In addition to this, the auxiliary vortex system delays the migration of horseshoe vortex to much further downstream and effective diminishes the endwall crossflow. As a result, there is a strong lateral gradient in heat transfer downstream of the throat for a step configuration while heat transfer is fair uniform downstream of the throat for a flat configuration. In general, the boundary layer forming on the passage endwall for a flat configuration was largely three dimensional compared to that for the step configuration.

Finally, heat transfer augmentation with Mach number is highest at the flow reattachment region after the step at high exit Mach numbers. At sonic exit Mach number, a shock effect on endwall heat transfer was noticeable. The aerodynamic losses are relatively unchanged for the flat configuration while a linear increase in losses was observed for the step configuration. At design exit conditions (M_{exit}/Re_{exit} = 0.85 / 1.45 x 10^6), there was a ~37.2% increase in the aerodynamics loss coefficient between the two configurations.

Acknowledgement

Special thanks to the sponsors of this work, Solar Turbines Inc.

REFERENCES

[1] Herzig, H. Z., Hansen, A. G., and Costello, G. R., "*A Visualization Study of Secondary Flows in Cascades*," NACA Report 1163, Feb. 1953.

[2] Goldstein, R. J., and Karni, J., "*The Effect of a Wall Boundary Layer on Local Mass Transfer from a Cylinder in Crossflow*," Journal of Heat Transfer, Vol. 106, May 1984, pp. 260–267.

[3] Sieverding, C. H., and Van den Bosche, P., "*The Use of Coloured Smoke to Visualize Secondary Flows in a Turbine Cascade*," Journal of Fluid Mechanics, Vol. 134, 1983, pp. 85–89.

[4] Sieverding, C. H., "*Recent Progress in the Understanding of Basic Aspect of Secondary Flows in Turbine Blade Passages*," Journal of Engineering for Gas Turbines and Power, Vol. 107, April 1985, pp. 248–257.

[5] Langston, L. S., Nice, M. L., and Hooper, R. M., "*Three-Dimensional Flow Within a Turbine Cascade Passage*," Journal of Engineering for Power, Vol. 99, Jan. 1977, pp. 21–28.

[6] Langston, L. S., "*Crossflow in a Turbine Cascade Passage*," Journal of Engineering for Power, Vol. 102, No. 4, 1980, pp. 866–874.

[7] Langston, L. S., "*Secondary Flows in Axial Turbines—A Review*," Turbine 2000 Workshop, Proceedings of the International Symposium on Heat Transfer in Gas Turbine Systems, Cesme, Turkey, Annals of the New York Academy of Sciences, edited by R. J. Goldstein, Vol. 934, NY Academy of Sciences, New York, pp. 11–26

[8] Wang, H. P., Olson, S. J., and Goldstein, R. J., "*Flow Visualization in a Linear Turbine Cascade of High Performance Turbine Blades*," Journal of Turbomachinery, Vol. 119, No. 1, 1997, pp. 1–8.

[9] Kang, M. B., Kohli, A., and Thole, K. A., "*Heat Transfer and Flowfield Measurements in the Leading Edge Region of a Stator vane Endwall*," Journal of Turbomachinery, Vol. 121, 1999, pp. 558–569.

[10] Graziani, R. A., Blair, M. F., Taylor, J. R., and Mayle, R. E., "*An Experimental Study of Endwall and Airfoil Surface Heat Transfer in a Large Scale Turbine Blade Cascade*," Journal of Engineering for Power, Vol. 102, 1980, pp. 257–267.

[11] Ames, F. E., Barbot, P. A., and Wang, C., "*Effects of Aeroderivative Combustor Turbulence on Endwall Heat Transfer Distributions Acquired in a Linear Vane Cascade*," Journal of Turbomachinery, Vol. 125, 2003, pp. 210–220.

[12] Lynch, S. P., and Thole, K. A., "The *Effect of the Combustor-Turbine Slot and Midpassage Gap on Vane Endwall Heat Transfer*," Journal of Turbomachinery, Vol. 133, 2011, pp. 041002–1-9.

[13] Thrift, A., Thole, K. A., and Hada, S., "*Impact of the Combustor-Turbine Interface Slot Orientation on the Durability of a Nozzle Guide Vane Endwall*," Journal of Turbomachinery, Vol. 135, 2013, pp. 041019–1-10.

[14] Thrift, A., Thole, K. A., and Hada, S., "*Effects of an Axisymmetric Contoured Endwall on a Nozzle Guide Vane: Convective Heat Transfer Measurements*," Journal of Turbomachinery, Vol. 133, 2011, pp. 041008–1-10.

[15] Saha, A. K., and Acharya, S., "*Computations of Turbulent Flow and Heat Transfer Through a Three-Dimensional Nonaxisymmetric Blade Passage*," Journal of Turbomachinery, Vol. 130, 2008, pp. 031008–1-10.

[16] Piggush, J. D., and Simon, T. W., "*Heat Transfer Measurements in a First-Stage Nozzle Cascade Having Endwall Contouring: Misalignment and Leakage Studies*," Journal of Turbomachinery, Vol. 129, 2007, pp. 782-790.

[17] Laveau, B., Abhari, R. S., Crawford, M. E., and Lutum, E., "*High Resolution Heat Transfer Measurements on Flat and Contoured Endwalls in a Linear Cascade*," Journal of Turbomachinery, Vol. 135, 2013, pp. 041020–1-9.

[18] Giel, P. W., Thurman, D. R., Van Fossen, G. J., Hippensteele, A. A., and Boyle, R. J., "*Endwall heat transfer measurements in a transonic turbine cascade*", J. Turbomachinery, Vol. 120, 1998, pp. 305-313.

[19] Roy, A., Blot, D. M., Ekkad, S. V., Ng, W. F., Lohaus, A. S., and Crawford, M. E., "*Effect of Upstream Purge Slot on a Transonic Turbine Blade Passage: Part 2 – Heat Transfer Performance*", ASME Paper No. GT2013-94581.

[20] Boyle, R. J., and Russel, L. M., "*Experimental Determination of Stator Endwall Heat Transfer*", Journal of Turbomachinery, Vol. 112, 1990, pp. 547-558.

[21] Barringer, M. D., Thole, K. A., and Polanka, M. D., "*An Experimental Study of Combustor Exit Profile Shapes on Endwall Heat Transfer in High Pressure Turbine Vanes*", Journal of Turbomachinery, Vol. 131, 2009, pp. 021009–1-10.

[22] Anto, K. S. Xue and Ng, W. F., Zhang, L. J. and Moon, H. K., "*Effects of Tip Clearance Gap and Exit Mach Number on Turbine Blade Tip and Near-Tip Heat Transfer*," Proceedings of ASME Turbo Expo GT2013-94345.

[23] Holmberg, D .G., and Diller, T. E., "*Simultaneous Heat Flux and Velocity Measurements in a Transonic Turbine Cascade*," ASME Journal of Turbomachinery, Vol. 127, 2005, pp. 502-506.

[24] Nix, A. C., Diller, T. E., and Ng, W. F., "*Experimental Measurements and Modeling of the Effects of Large-Scale Freestream Turbulence on Heat Transfe*r," ASME Journal of Turbomachinery, Vol. 129, 2007, pp. 542-550.

[25] Smith, D. E., Bubb, J. V., Popp, O., Grabowski, H. C., Diller, T. E., Schetz, J. A. and Ng. W. F., "*Investigation of Heat Transfer in a Film Cooled Transonic Turbine Cascade, Part I: Steady Heat Transfer*," 2000, Proceedings of ASME 2000-GT-202.

[26] Popp, O., Smith, D. E., Bubb, J. V., Grabowski, H. C., Diller, T. E. Schetz, J. A. and Ng. W. F., 2000, "*Investigation of Heat Transfer in a Film Cooled Transonic Turbine Cascade, Part II: Unsteady Heat Transfer*," Proceedings of ASME 2000-GT-203.

[27] Carullo, J. S., Nasir, S., Cress, R. D., Ng, W. F., Thole, K. A., Zhang, L. J., and Moon, H. K., "*The Effects of Freestream Turbulence, Turbulence Length Scale, and Exit Reynolds Number on Turbine Blade Heat Transfer in a Transonic Cascade*," ASME Journal of Turbomachinery, Vol. 133, 2011, 011030-1-11.

[28] Nasir, S., Carullo, J. S., Ng, W. F., Thole, K. A., Wu, H., Zhang, L. J., and Moon, H. K., "*Effects of Large Scale High Freestream Turbulence, and Exit Reynolds Number on Turbine Vane Heat Transfer in a Transonic Cascade*," ASME Journal of Turbomachinery, Vol. 131, 2009, pp. 021021-1-11.

[29] Xue, S., Roy, A., Ng, W. F., and Ekkad, S. V., "*A Novel Transient Technique to Determine Recovery Temperature, Heat Transfer Coefficient, and Film Cooling Effectiveness Simultaneously in a Transonic Turbine Cascade*," ASME Journal of Thermal Science Engineering Application, Vol. 7, 2014, pp. 011016-1-10.

[30] Moffat, R. J., 1988, "*Describing Uncertainties in Experimental Results*," Exp. Thermal and Fluid Science, 1988, pp. 3-17.

[31] Brown, K. H., Coleman, H. W., and Steele, W. G., 1995, "*Estimating Uncertainty Intervals for Linear Regression*," AIAA–1995-0796

[32] Spencer, M. C., Lock, G. D., Jones, T. V., and Harvey, N. W., "*Endwall Heat Transfer and Aerodynamic Measurements in an Annular Cascade of Nozzle Guide Vanes*," International Gas Turbine and Aero engine Congress and Exposition, 95-GT-356.

CHAPTER 4

Conclusions

The heat transfer and flow characteristics on the blade tip, near-tip and endwall of a high pressure turbine have been investigated under engine representative transonic high turbulence conditions in a linear cascade. The underlying secondary flow physics behind the observed aerothermal characteristics for different tip and endwall configurations were analyzed using experimental and computational methods. The findings, presented herein, are new and add significantly to the existing body of literature.

The aerothermal characteristics of a blade tip vary significantly depending on the tip configuration. For a flat blade tip, the heat transfer is governed by turbulence production due to cross-flow along the pressure side edge close to the leading edge. These turbulent properties are transported across the tip resulting in a large region of elevated heat transfer on the tip surface. The downstream lobe of a flat blade tip surface was found to have supersonic leakage flow which results in multiple over-tip shocks. These shock-boundary layer interactions cause a large spatial variation in heat transfer due to the sudden pressure rise after the shock causing the boundary layer to suddenly thicken. Such high Mach number effects underline the importance of transonic experiments in analyzing the turbine surface heat transfer characteristics. Unlike a flat tip, the leakage flow over a squealer tip is predominantly subsonic and the highest heat transfer level exists where the flow reattaches on the cavity floor. In-cavity squealer vortices form acting act as a labyrinth seal and thereby reducing the over-tip leakage flow. However, these squealer vortices cause increased stage aerodynamic losses and low film-cooling effectiveness due to increased mixing between the coolant and the leakage flow. Furthermore, the interaction between

the tip purge flow and leakage flow was found to result in multiple reattachments i.e. hot spots, on the tip surface.

Finally, the heat transfer and secondary flow characteristics on a flat endwall was found to be first-order dependent on the combustor-turbine transition configuration. A combustor-turbine misalignment, in the form of a backward facing step at the turbine inlet, severely weakens the classical endwall secondary flows i.e. the horseshoe and passage vortices. Instead, a new auxiliary vortex system is formed from the interaction between the recirculating flow after the step and the vane potential field. This auxiliary vortex system propagates through the passage resulting in ~20%-40% heat transfer augmentation on the endwall and ~37% increase in the stage aerodynamic losses. In conclusion, these studies revealed that the peak heat transfer tends to occur in regions with local secondary flow reattachment and new boundary layer formation. Furthermore, increasing the exit Mach/Reynolds number does not significantly alter the secondary flow structure but increases its intensity thereby augmenting the surface heat transfer while maintaining similar spatial distribution.

CHAPTER 5

Future Work

Several aspects related to the research topic presented in this manuscript still require further investigation. The possibility of using rotor tips with optimized contoured surface to optimize the turbine stage aerodynamic and/or heat transfer characteristics requires further investigation. For instance, there exists a possibility of using tip contours to induce shocks that can choke the tip clearance and effectively control the leakage mass flow. There is also need to explore the effect of leakage and tip purge flow on the turbine shroud surface heat transfer and film-cooling characteristics. Similarly, the shroud surface cooling flow is likely to have a significant effect on the leakage flow and tip heat transfer. This study has also highlighted the effect of having combustor-endwall misalignment at the turbine inlet for a flat endwall. However, there is need for future studies to couple this inlet misalignment with an engine representative endwall contour and investigate the resulting endwall aerothermal characteristic. Furthermore, it is likely that there exists a significant amount of interaction between the endwall platform cooling flows and the endwall secondary flows which needs to be investigated.

Appendix A: The Virginia Tech Transonic Test Facility

Figure A.1 shows a CAD model of the Virginia Tech blowdown transonic tunnel which is located in the basement of Randolph building. This test facility consists of an electric Ingersoll Rand piston compressor, two external tanks, heating loop and a test section cascade. This wind tunnel is a quasi-steady state facility capable of exit Mach numbers of ~1.2 and heat transfer measurements. As a quasi-steady state facility, the cascade achieves aerodynamic steady state conditions for approximately 15-20 seconds (depending on the mass flow) but with transient inlet total temperature as illustrated in Figure A.2. The maximum mass flow is approximately 12 lbms/sec with inlet turbulence intensities as high as 16%.

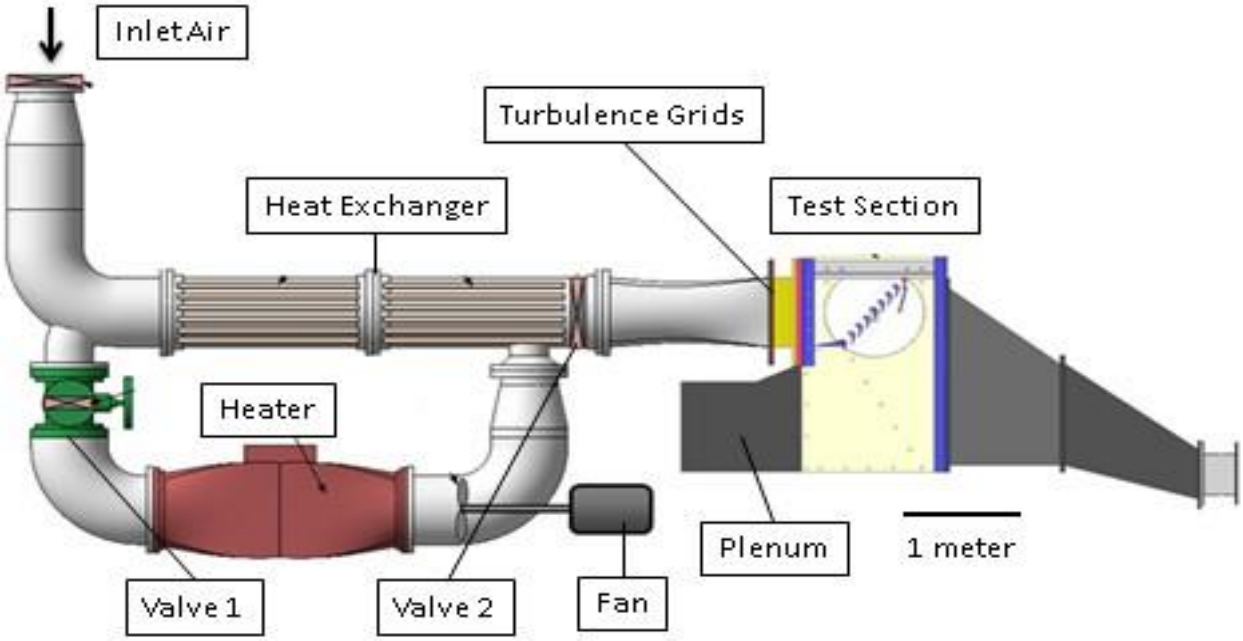

Figure A.1: A scale model of the linear transonic wind tunnel at Virginia Tech

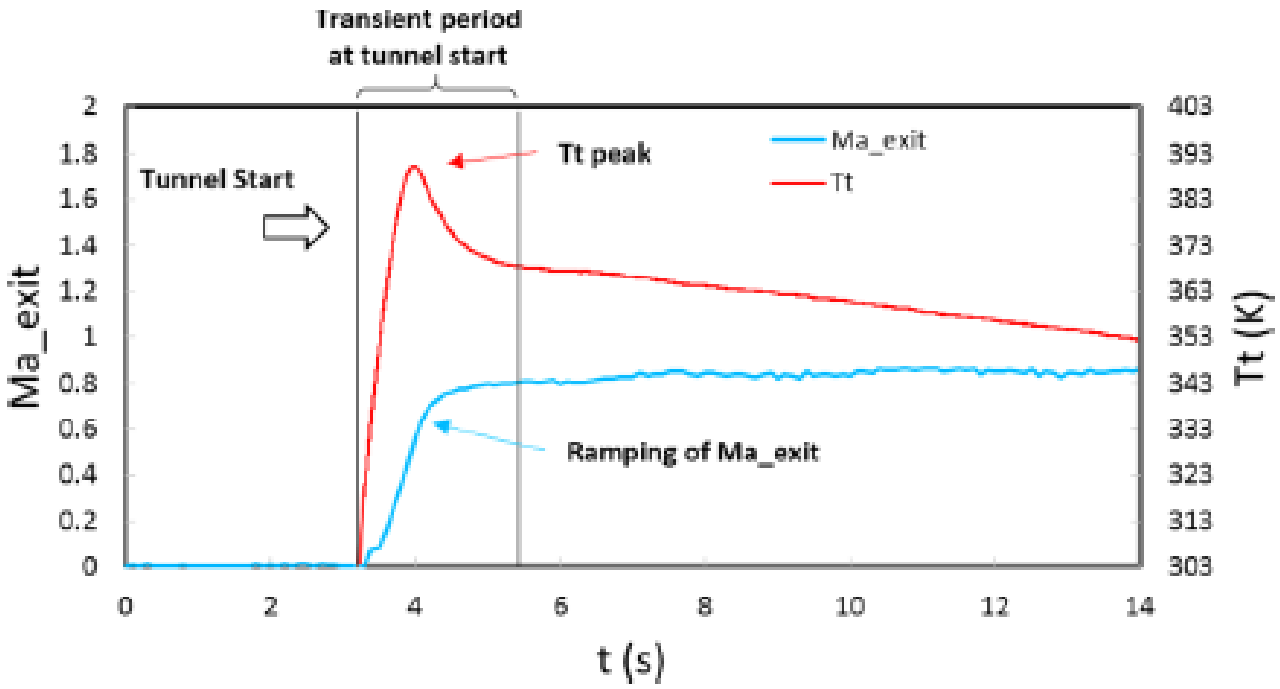

Figure A.2: A sample data plot of the cascade inlet conditions variation with time illustrating the quasi-steady state nature of the transonic wind tunnel facility

During aero measurement experiments, the external tanks are pressurized by the compressor upto nearly 200psi while an upstream control valve, valve 1 and valve 2 are closed. After the desired tank pressure is reached, the control valve and valve 2 are opened and compressed air flows through the test section and exits through the exhaust. The desired exit Mach number is achieved by specifying the objective pressure of the control valve. The objective pressure controls the valve angle position to ensure a constant mass flow. This objective pressure is usually determined through a series of shakedown runs prior to the actual data collection run.

The operation cycle is slightly different for heat transfer experiments to accommodate for the compressed air to be heated prior to entering the test section. Prior to blowdown, valve 1 is opened while the inlet control valve and valve 2 remain closed. The heater and fan are then turned on which in turn heats up the air and the copper rods within the heat exchanger loop. The copper rods act as a thermal capacitor. Once the air and copper rods in the heating loop reach the desired temperature (usually ~120^{o}C), valve 1 is closed and the inlet control valve and valve 2

are opened simultaneously. The compressed air is heated as it passes through the bank of copper rods heat exchanger and the temperature data is simultaneously recorded at the surface of interest in the test section. The mainstream inlet total temperature is measured using a total temperature probe located within the heating loop, slightly upstream of valve 2. Another static temperature thermocouple located upstream of the turbulence grid measures the test section airflow temperature and is used to determine the tunnel start time. The start time for the heat transfer experiments is defined by a 0.2^{o}C rise in the test section air flow temperature. A meshed passive inlet turbulence grid was placed upstream of the cascade to generate the desired engine representative inlet turbulence. Further details on the cascade inlet turbulence conditions can be found in Appendix H.

Appendix B: Rotor Tip Cascade Set Up

The rotor blade cascade used for both the flat and squealer tip studies consisted of seven full blades and two half blades as shown in Figure B.1. The pressure side and suction side half blades were placed at the top and bottom of the cascade respectively. The half blades, in combination with the fixed tail board shown in Figure B.1, were used to promote flow periodicity through the cascade. The periodicity of a similar cascade with the same blade geometry was established by Carullo et al. [1].

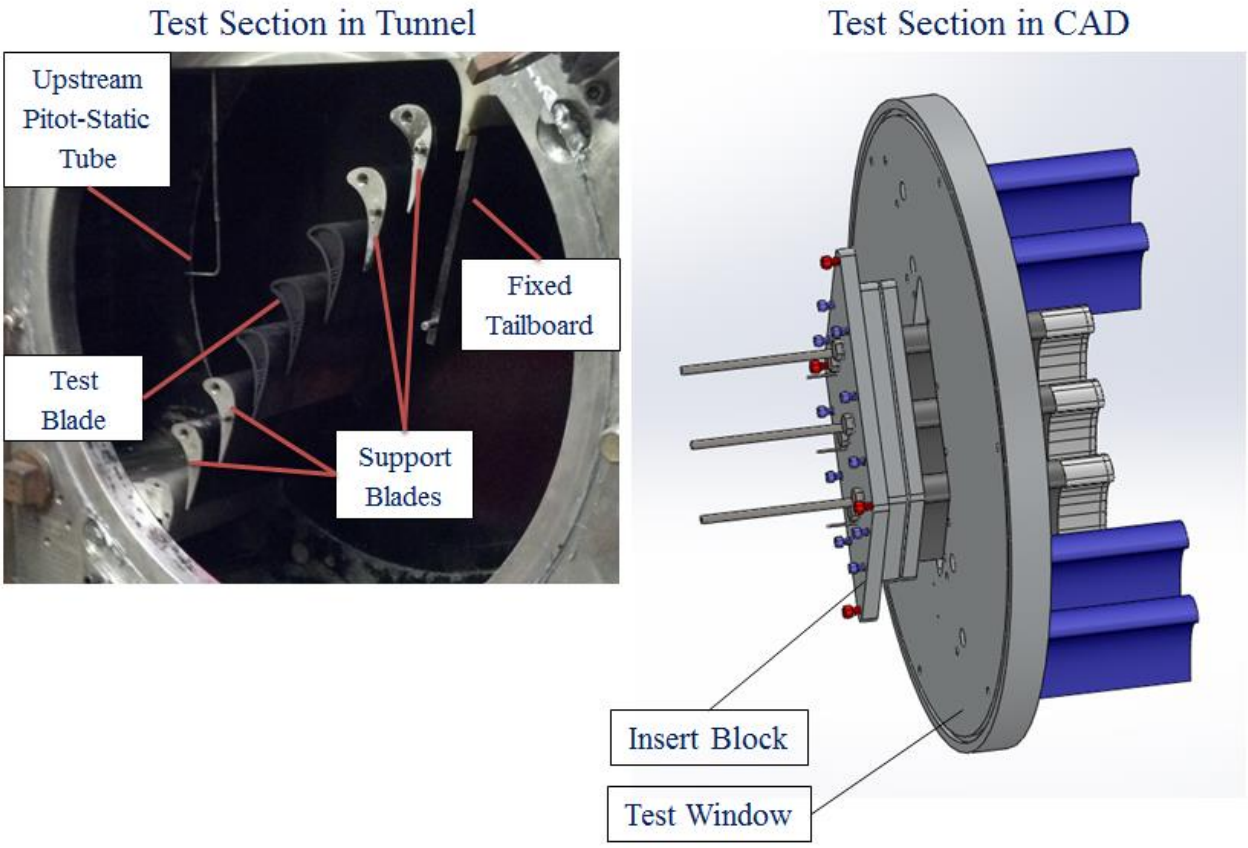

Figure B.1: The rotor blade cascade set up

The inlet for this cascade was located approximately 0.6C upstream of the test blade leading edge. Prior to the heat transfer experiments, a series of hotwire, Kiel and thermocouple measurements were taken on this plane by Carullo et al. [1] to determine the inlet turbulence, pressure and temperature profiles which were then used as boundary conditions for

computational modeling. During each experiment, the inlet and exit conditions were measured using an inlet midspan pitot-static probe and six exit wall static pressure ports located 0.5C downstream of the trailing edge plane. A summary of the cascade geometric properties are shown in Table B.1. However, it is important to note that the actual engine span is 7.62 cm (3 in), and the rotor tip clearance is always specified as a percentage of this engine span.

Table B.1: Summary of the Blade Cascade

Chord, C	69.9 mm
Axial Chord, C_x	35.2 mm
Pitch, P	58.2 mm
Tip Clearance Size	1% of engine span
Exit Isentropic Mach Number, M_2	0.60, 0.85 (design), 1.0
Inlet Turbulence Intensity, Tu_1	12%
Blade Turn Angle	107.5°

All the blades in the cascade, with the exception of the three central blades, were supported on either side of the test section walls. The three center blades were attached to a removable insert block which allowed for equal tip clearances for the three blade tips. Even though heat transfer data was measured on only the central blade tip as shown in Figure B.2, creating similar treatments to each of the adjacent blades ensures flow periodicity around the instrumented central blade tip. The test section wall adjacent to the central blade tip was made of Zinc Selenide (ZnSe) infrared window. The IR window allowed for optical access to the blade tip surface and provided high infrared transmissivity for the IR camera to record the temperature history of the blade tip surface.

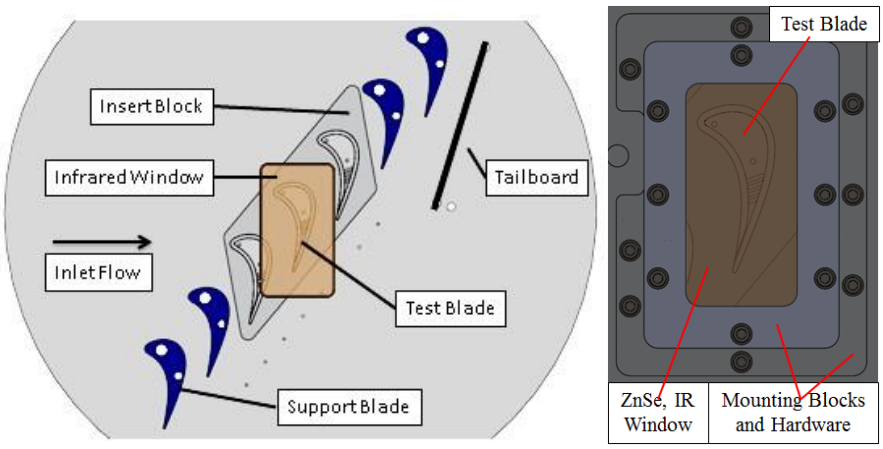

Figure B.2: CAD model of the blade cascade showing the mounting of the infrared window

Figure B.3 shows further details of the rotor tip geometries as well as the internal structure of the squealer tip design. The blade profile for the flat tip and squealer tip designs were the same with the only difference being in the tip surface design. The blade tips were 3D printed using the Fortus 250mc rapid prototyping machine by Stratasys. The printed tips span was 1.5 inches (3.81 cm) and were joined to a 4.5 in (11.43 cm) span metal blade base attached to the insert block. It was necessary to have the tip made of ABS material due to its low conductivity (k = 0.188 W/mK) that allowed for the 1-D semi-infinite heat conduction assumption in the data reduction technique. The ABS parts were treated with acetone to smooth the surface and "seal" the surface from leakage. The tips were then screwed to the base metal blades and the junction smoothened using J-B Weld epoxy. This design also allowed for interchanging of the blade tips while keeping the same insert block.

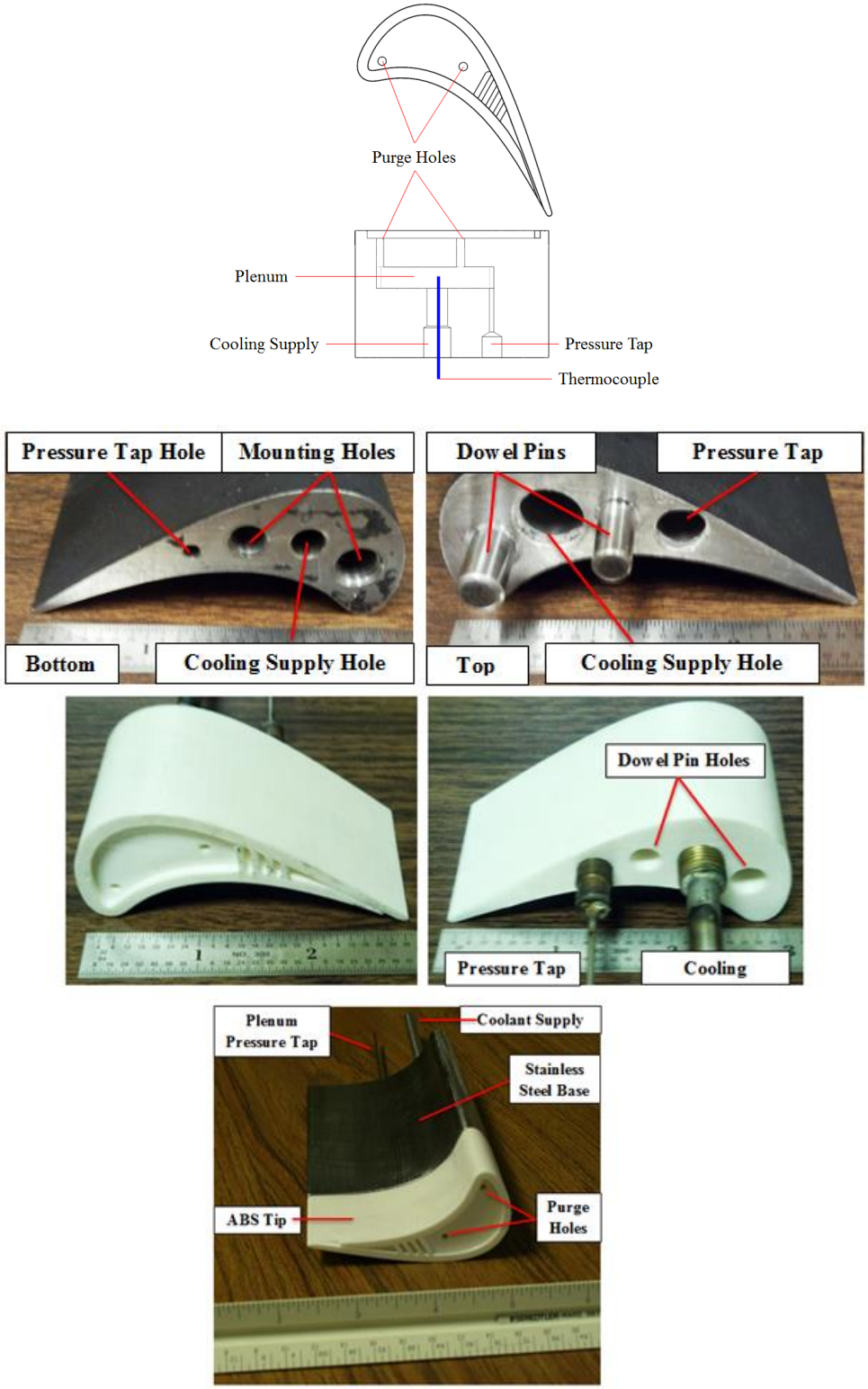

Figure B.3: A cross-section of the ABS tip showing the internal features, instrumentation and the assembly of the tip to the base metal piece

The squealer tip design had a coolant supply line to an inbuilt plenum/tank from which then cooling air was ejected through the two purge holes on the tip surface. The straight

cylindrical purge holes had a diameter of 0.1 in (0.254 cm) and the squealer tip cavity depth was 0.09 in (0.229 cm) with a bleeder cutout on the pressure side near the trailing edge. Four parallel ribs were located inside the cavity for structural and aerodynamic purposes. The pressure and temperature inside the plenum for each of the three center tips was measured through the respective temperature and pressure tap channels (see Figure B.3). Monitoring of the plenum pressures of the three tips was used to very that there was uniformity in the three blowing ratios. During the tests, the plenum pressures were controlled to within 3% of each other.

References

[1] Carullo, J.S., Nasir, S., Cress, R.D., Ng, W.F., Thole, K.A., Zhang, L.J., and Moon, H.K., 2011, "The *Effects of Freestream Turbulence, Turbulence Length Scale, and Exit Reynolds Number on Turbine Blade Heat Transfer in a Transonic Cascade*," ASME J. Turbomach., Vol. 133, 011030.

Appendix C: Nozzle Endwall Cascade Set Up

The test section and cascade for the nozzle endwall heat transfer experiments is shown in Figure C.1. This cascade is very similar to that used by Nasir et al. [1] albeit with some modifications to allow for endwall geometry modifications and heat transfer measurements. The turbulence grid position was modified from that used in the rotor tip studies so that the turbulence intensity was 16% at the cascade inlet plane located 0.48C upstream of the vane leading edge. Further details on the inlet flow conditions can be found in Appendix H. Table C.1 summarizes the cascade geometry specifications.

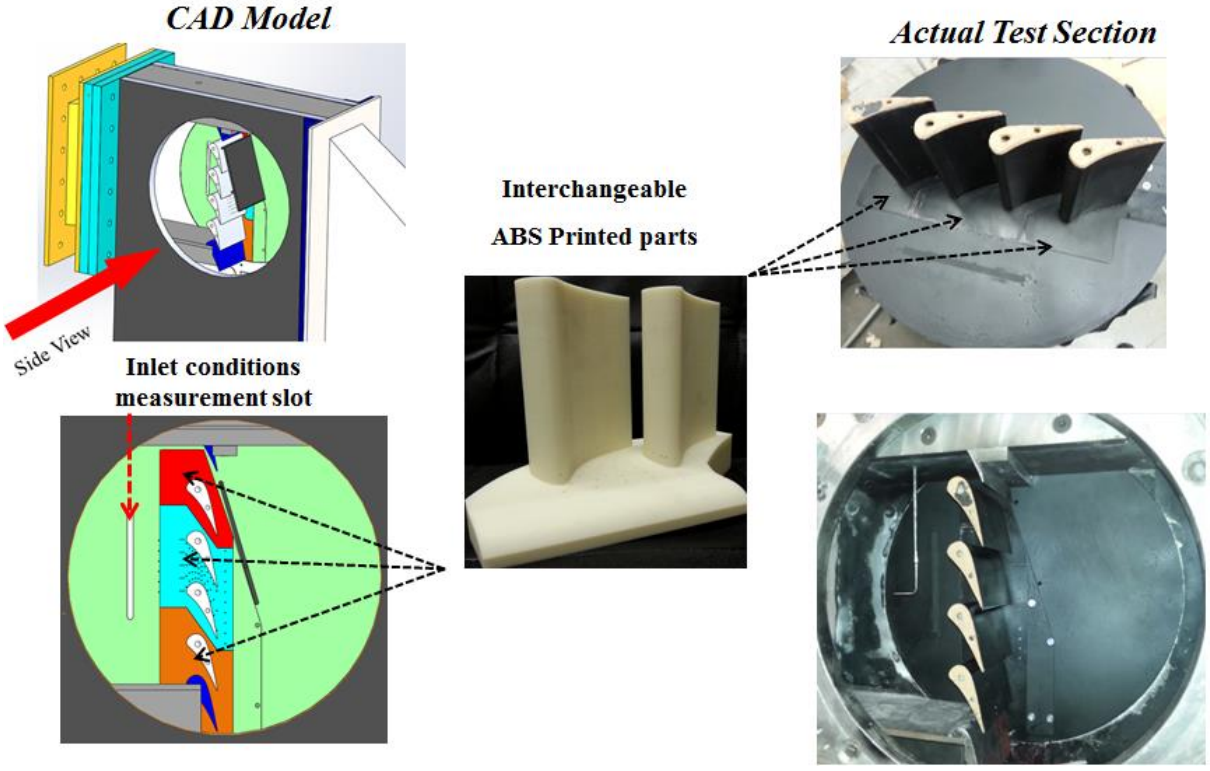

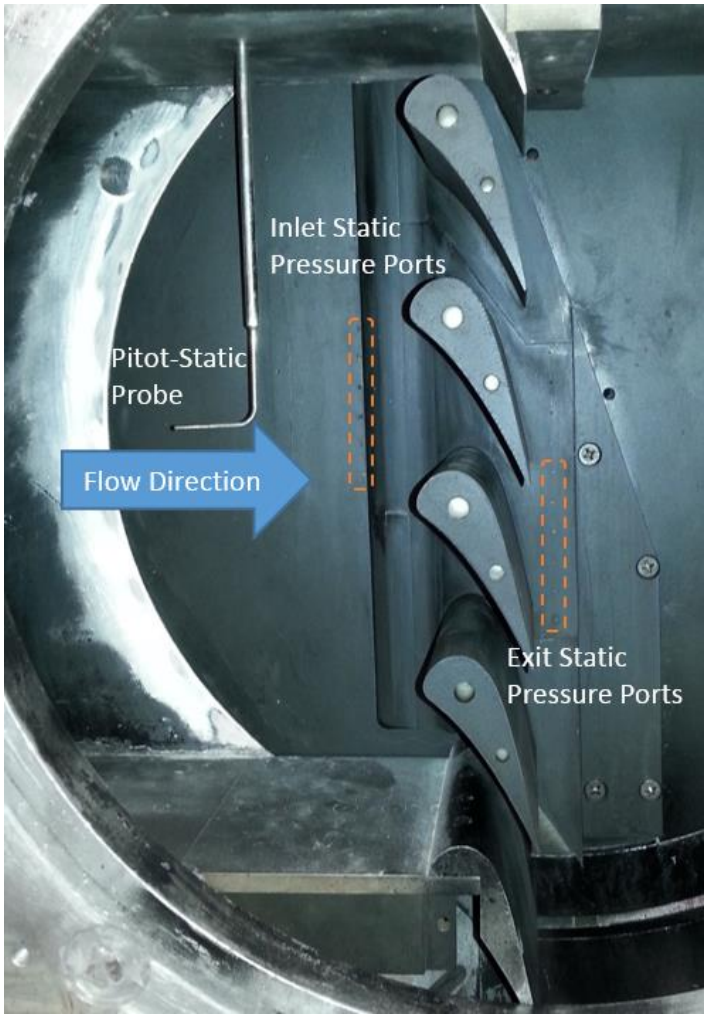

Figure C.1: Vane cascade set up for the endwall heat transfer experiments

Table C.1: Summary of the Vane Cascade

Chord, C	91.2 mm
Axial Chord, C_x	50.0 mm
Pitch, P	83.1 mm
Entry Step Height	6.78 mm
Exit Isentropic Mach Number, M_2	0.60, 0.85 (design), 1.0
Inlet Turbulence Intensity, Tu_1	16%

The cascade side walls were made of Lexan polycarbonate which was then painted black to minimize light reflections that may interfere with the IR measurements. However, on the endwall side, a section of the Lexan polycarbonate material was cut out and replaced with a printed ABS endwall and vane shown in Figure C.2. This was necessary for heat transfer measurements to be made on the endwall surface and accommodate the 1-D semi-infinite conduction medium in during the data reduction. Due to the size of the test section and the 3D printer's size limitations, the endwall geometries were made in three parts; a center piece containing two vanes with a central heat transfer measurement passage, and an upper and lower piece, each with one vane. This design also allowed for re-usability of some of the parts between the pressure measurement experiments and heat transfer experiments. An illustration of this three piece set-up for the Flat Entry – Flat Endwall configuration is shown in Figure C.2.

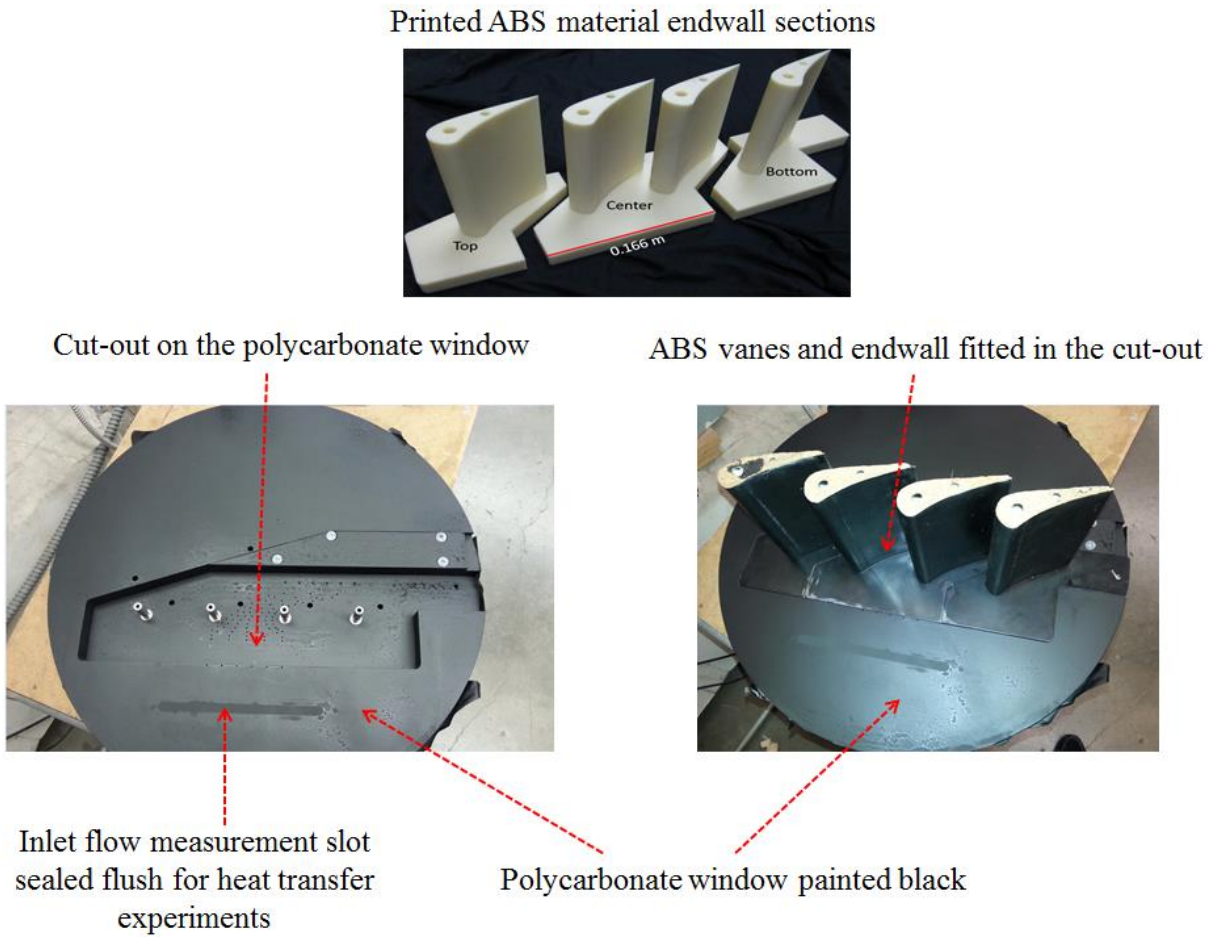

Figure C.2: ABS parts fitted onto the test section polycarbonate window

To prepare the printed parts for testing, the surfaces of all the parts were lightly sanded then treated with acetone to obtain a smooth surface finish. The parts were then lightly sprayed with black paint for improved IR measurement. The vanes were then secured to the polycarbonate window with screws on the backside and the three sections bonded together using silicone and JB Weld to prevent leakage through the mate faces. The setup was then inserted into the test section and matefaces treated again with silicone and JB Weld epoxy to prevent any leakage. The excess JB Weld epoxy and silicone on the matefaces were finally lightly sanded for a smooth finish.

Twelve 1/16" brass tubes for measuring the cascade inlet and exit static pressure were then inserted into the test section window and secured in place with epoxy. A pitot-static probe

was also inserted through the top of the test section at 1C (0.0912 m) upstream of the cascade leading edge, in the center of the inlet flow passage. The assembled test section is shown in Figure C.1.

An accurate measurement of the endwall surface temperature throughout the duration of each tunnel run was collected using a FLIR A325 infrared camera. The IR camera uses blackbody emission radiated from a surface to output that surface's temperature. The inside of the test section was painted black to reduce reflections and increase emissivity of the infrared wavelength. Prior to testing, the IR camera was calibrated to a precision error of +/-0.3^{o}C. The test section wall opposite the endwall surface was fitted with a Zinc Selenide (ZnSe) infrared window as shown in Figure C.3 below. The window had an anti-reflective coating applied on it and transmitted nearly 97% of 9.3 μm infrared wavelength.

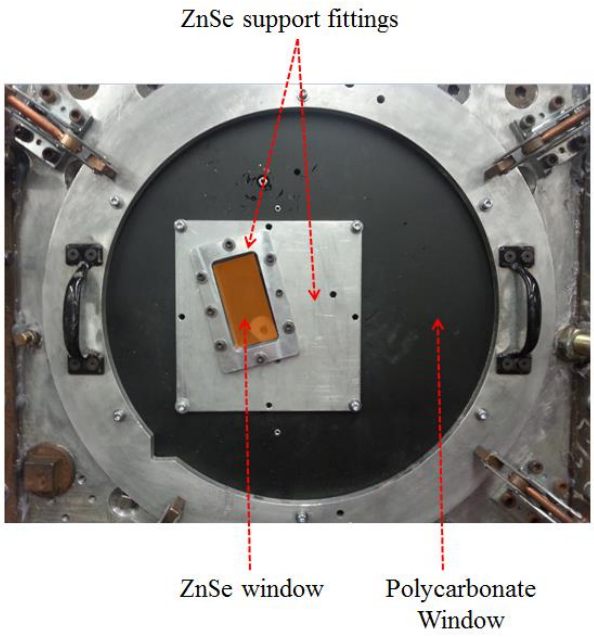

Figure C.3: ZnSe infrared window mounting onto the test section side wall

The IR window was installed in two positions to allow for thermal imaging of the whole endwall platform. These two IR window positions are shown in Figure C.4 below. It was desired

to map out the entire endwall platform heat transfer distribution starting from the inlet plane located 0.48C upstream of the leading edge to the passage trailing edge. However, due to financial and design constraints, a complete map of the endwall temperature data had to be collected using two separate runs: The first run recorded the upstream endwall data and the second run recorded the downstream region of the passage. Figure C.5 shows the effective viewing area of the endwall passage after combining the temperature data from the two IR window positions. Finally, an in house Matlab code was used to stitch the two data sets to obtain a complete map of the endwall platform heat transfer data.

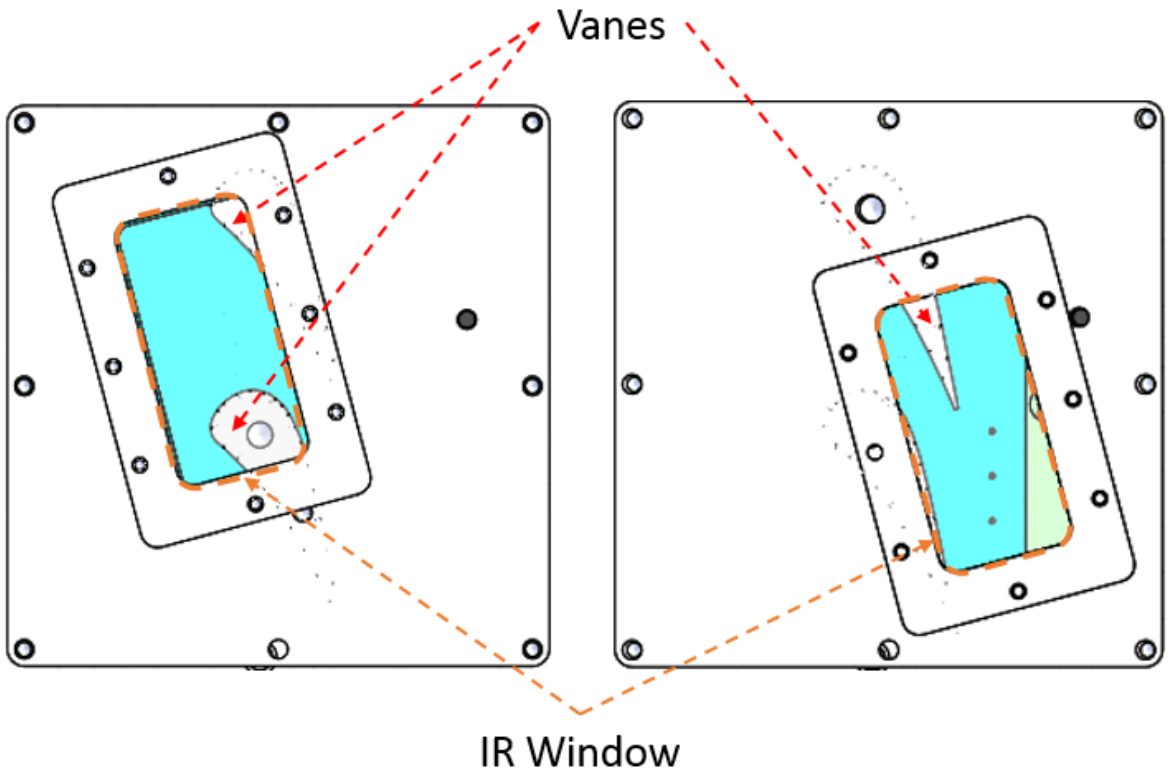

Figure C.4: Positions of the IR window. The left orientation captures the upstream section of the endwall while the right orientation captures the downstream section.

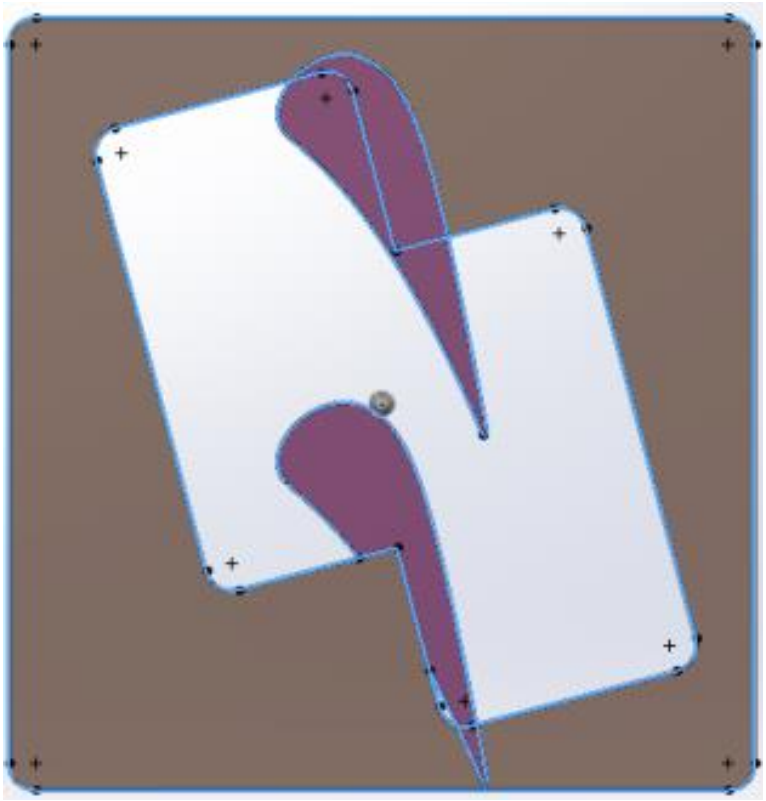

Figure C.5: The effective passage endwall heat transfer data measurement region

References

[1] Nasir, S., Carullo, J.S., Ng, W.F., Thole, K.A., Wu, H., Zhang, L.J., and Moon, H.K., 2009, "*Effects of Large Scale High Freestream Turbulence, and Exit Reynolds Number on Turbine Vane Heat Transfer in a Transonic Cascade*," ASME J. Turbomach., Vol. 131, 021021.

Appendix D: Experiment Non-dimensional Variables

In order to conveniently organize the information from the cascade experiments and for future comparison to other experiments, the flow variables and cascade configuration were non-dimensionalized using the Buckingham pi Theorem. It is important to understand that, while the Nusselt number is only a function of the local fluid variables, these local flow variables are influenced by the cascade configuration/geometry. Therefore, the flow conditions as well as the cascade geometry characteristics determine the heat transfer characteristics on the surface of interest.

The following flow variables were identified to have a first order effect on the Nusselt number. Notice that, from the start, the turbulence intensity and heat capacity ratio were already dimensionless.

Variable	**Dimension**
Velocity, V	$[LT^{-1}]$
Density	$[ML^{-3}]$
Gas constant, R	$[L^2T^{-2}\Theta^{-1}]$
Gamma, γ	[1]
Viscosity,μ	$[ML^{-1}T^{-1}]$
Temperature, Θ	$[\Theta]$
Chord, C	[L]
Turbulence intensity, Tu	[1]
Specific heat, C_p	$L^2MT^{-2}\Theta^{-1}$

Thermal conductivity, k	$MLT^{-3}\Theta^{-1}$

From the listed ten variables, there are four unique dimensions. The Buckingham Pi theorem indicates that we should expect 10 - 4 = 6 independent dimensionless variables as follows:

$$\text{Nu\#} = f\left(\frac{\rho VC}{\mu}, \frac{V}{\sqrt{\gamma RT}}, \frac{\mu RCp}{k}, \frac{V^2}{\Theta Cp}, \text{Tu}, \gamma, \text{geometry}\right)$$

Dimensionless Variable	**Name**
$\frac{\rho VC}{\mu}$	Reynolds number, Re
$\frac{V}{\sqrt{\gamma R\Theta}}$	Mach number, M
$\frac{\mu RCp}{k}$	Prandtl number, Pr
	Turbulence intensity, Tu
	Gamma, γ
$\frac{V^2}{\Theta Cp}$	Eckert number, Ec

The Nusselt number at any position in the cascade is defined by the local values of the above flow dimensionless numbers. However, in actual experiments, it is often not possible to define all the local fluid variables. Therefore, these variables are often defined using either the cascade inlet or exit flow conditions as reference.

The variation of these variables across the cascade (and consequently the Nusselt number variation) depends on the cascade geometry. As a result, the cascade configuration has a

secondary effect on the Nusselt number in the passage. To account for the effect of these geometric variables and account, a new non-dimensional number – Cascade Configuration Number (CC#) – was defined. This variable provides an indication of the variation in heat transfer characteristics from a baseline configuration due to the perturbation geometry of interest (tip clearance or inlet misalignment size)

Variable	**Value**
Aspect ratio, (Chord/Span), AR	0.45(blade), 0.60 (vane)
Solidity, (Chord/Pitch), S	1.20 (blade), 1.10(vane)
Turning angle (radians), θ	1.88(blade), 1.22 (vane)
Perturbation geometry (Tip clearance, misalignment height), h	0.000762[m], 0.0068 [m]
Perturbation geometry Reynolds number, Re_h	$\frac{\rho V_\infty h}{\mu}$
Inlet distance	a

Using non-dimensional analysis, we can define a Cascade Configuration Number (CC#) as shown below. This Cascade Configuration Number (CC#) is just an indicator of the extent to which the perturbation geometry of interest affects the heat transfer and flow characteristics in the cascade. It can be seen that the effect of the perturbation geometry depends on the size of the geometry, its Reynolds number and distance from the surface of interest.

$$\text{CC\#} = \frac{\text{h x AR x } Re_h \; x \; cos\left(\frac{\theta}{2}\right)}{\text{a x S}}$$

Therefore: Nu# characteristics = f ($\frac{\rho VC}{\mu}$, $\frac{V}{\sqrt{\gamma RT}}$, $\frac{\mu RCp}{k}$, $\frac{V^2}{\Theta Cp}$, Tu, γ, CC#)

Appendix E: ABS Material Properties Validation

The thermal material properties used to deduce the heat transfer data were obtained from the supplier of the ABS P-430 printing plastic. However, it was important to ascertain that these properties were valid for the printed and surface treated parts. Therefore, a sample of the printed part was sent to an outside vendor to establish the thermal properties. The density, heat capacity and thermal diffusivity of the part were measured. The thermal diffusivity was measured using the laser flash technique. The properties were established for the temperature ranges within which the actual experiments are conducted (~25^{o}C to ~100^{o}C).

An average of the material properties between the temperature range of 25^{o}C and 75^{o}C was used to determine if there was any significant effect on the calculated endwall heat transfer coefficient. It can be noted that, while there is variability in the individual material properties (ABS supplier specifications versus the actual measured properties), the overall difference in the calculated heat transfer coefficients is minimal/negligible as shown in Figure E.1. From the cook-felderman equation, it can be seen that the calculated surface heat flux varies as a function of $\sqrt{k\rho C_p}$. Therefore, it can be expected that the maximum difference in the predicted heat flux would be approximately 0.977%, which is significantly lower than the heat flux uncertainty.

Nu#	ABS Supplier Material Properties	3D Printed Part Measured Properties
	Density = 1080 kg/m3 ***Specific Heat = 1675 J/K.kg*** ***Thermal Conductivity = 0.188 W/m.K***	***Density = 1015 kg/m3*** ***Specific Heat = 1470 J/K.kg*** ***Thermal Conductivity = 0.2235 W/m.K***
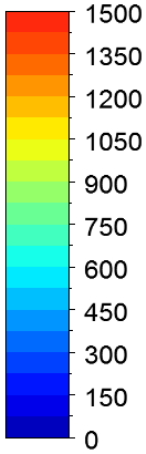	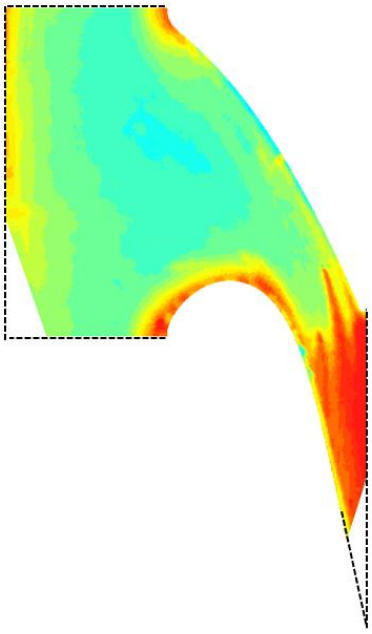	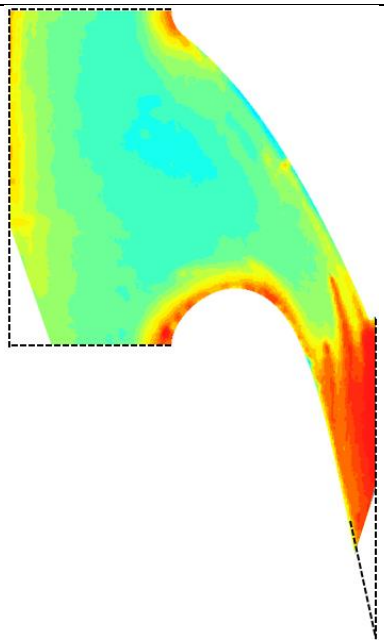

Figure E.1: Deduced endwall Nusselt number distribution using the supplier and measured material properties

Appendix F: Data Reduction Technique Fundamentals

This section highlights the key fundamentals of the experimental data processing technique used to obtain the heat transfer data presented in this manuscript. During the heat transfer experiments, only the inlet total temperature and the surface temperature of interest were recorded. The challenge was to use these two temperatures to determine the local recovery temperature and subsequently the local heat transfer coefficient throughout the passage endwall. The measured surface temperature history was used to calculate the surface heat flux and subsequently the surface heat transfer coefficient using the Cook-Felderman equation, Equation F-1, and linear regression technique respectively.

The cook-felderman equation determines the surface heat flux by solving the heat diffusion equation based on a 1-D semi-infinite conduction. It is important to note that, it is possible to use the finite difference scheme instead of the cook-felderman equation to determine the surface heat flux. However, this is at the expense of grid sensitivity errors and high computational expense. For Equation F-1, ρ, C_p and k are density, specific heat, and thermal conductivity of the solid domain. Delta-t, Δt, represents the time step which corresponds to the frequency of the IR camera. In these particular experiments, the IR frequency was 10 Hz which yields a Δt of 0.1 seconds.

$$q''_w(t_n) = \frac{2\sqrt{k\rho C_p}}{\sqrt{\pi\,\Delta t}} \sum_{j=1}^{n} \frac{T_j - T_{j-1}}{\sqrt{n-j} + \sqrt{n+1-j}} \qquad \text{(F-1)}$$

The second phase of the data reduction process used the calculated surface heat flux, together with the measured upstream total temperature, to calculate the heat transfer coefficient using a linear regression technique developed by Xue et al. [1]. It is worth noting that, even though the upstream total temperature was used in the regression technique, the calculated heat

transfer coefficient was based on the local recovery temperature on the surface of interest. The Linear Regression (LR) technique was used to calculate the surface heat transfer coefficient for tests without any surface film-cooling. Its variant, the Dual Linear Regression (DLR) technique, was used to calculate the surface heat transfer coefficient and film-cooling effectiveness for tests with surface film cooling.

Unlike low speed flow conditions, high Mach number conditions have significant compressibility and frictional heating effects and the driving temperature head is the recovery temperature as shown in Equation F-2. In low speed conditions, it is usually acceptable to use the upstream total temperature as the heat transfer driving temperature. With the surface heat flux already calculated, Equation F-2 can be re-expressed into a linear form, (see Equations F-3 and F-4). This re-expression is only valid because the Virginia Tech transonic wind tunnel is quasi-steady state (aerodynamically steady but thermally transient during data collection) facility. Therefore, the temperatures in this equation can be normalized using the measured upstream total temperature T_t. The wall temperature, T_w, is measured with a calibrated FLIR A325 infrared camera at a frequency of 10 Hz.

$$q'' = h(T_r - T_w) \tag{F-2}$$

$$\frac{q}{T_t} = h\frac{T_r}{T_w} - h\frac{T_w}{T_t} \tag{F-3}$$

$$\frac{q}{T_t} = hC_r - h\frac{T_w}{T_t} \tag{F-4}$$

$$y = C + mx$$

$$T_r = T_{t,\infty}\left(\frac{1+r_c\frac{\gamma-1}{2}M^2}{1+\frac{\gamma-1}{2}M^2}\right) = T_{t,\infty}C_r \tag{F-5}$$

Theoretically, the recovery temperature, T_r, can be calculated using Equation F-5, where r_c is the local recovery factor, M is the local Mach number, γ is the specific heat ratio of air and $T_{t,\infty}$ is the mainstream total temperature. However, the term in parenthesis represented as C_r is not known at every location across the endwall surface. The value of C_r is dependent on only the Mach number, as shown in Equation F-5, and is therefore a constant at a particular point on the endwall during the data reduction time window. Linearization of the heat transfer equation allows for the surface heat transfer coefficient to be determined from the slope of the regression line and the recovery temperature from the y-intercept.

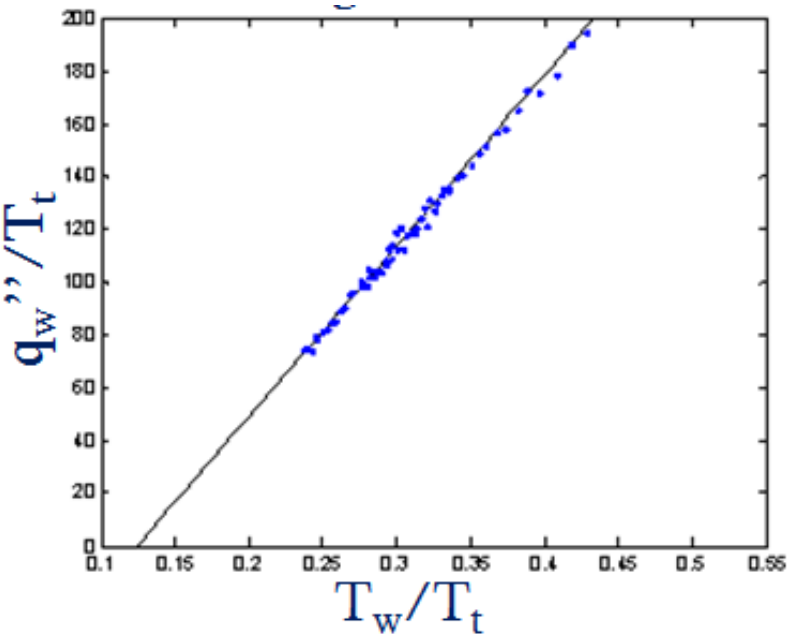

Figure F.1: A sample of linear regression applied to heat transfer data

The Dual Linear Regression technique is a slightly modified version of the linear regression technique and is used to simultaneously determine the heat transfer coefficient and the film-cooling effectiveness. The film-cooling effectiveness is a measure of the ability of the coolant fluid to protect the surface from high temperature mainstream flow by forming a low temperature fluid film on the surface of interest. The adiabatic film-cooling effectiveness is defined by Equation F-6. Again, the heat transfer equation can be linearized into the form shown

in Equation F-7. However, in this particular scenario, we face a problem whereby we have one equation and two unknowns (T_r and h). In order to resolve this problem, a second experiment was conducted with the same tunnel conditions but using chilled air as the coolant. Using two data sets with different coolant temperatures reduces the noise-to-signal ratio and provides a second data set to be used to determine the two unknown variables. Since the tunnel aerodynamic conditions are the same between the two runs, the heat transfer coefficient (regression slope) have to be the same. Therefore, we can now guess a series of T_r values (starting from $T_r = T_t$) and iterate until the R^2 value is minimized and the two data sets have the same slope as shown in Figure F.2. The slope of this regression line yields the heat transfer coefficient and the film-cooling effectiveness can be determined from the x-intercept.

$$\eta = \frac{T_r - T_{aw}}{T_r - T_c} \tag{F-6}$$

$$\frac{q''_w}{T_r - T_c} = h\frac{T_r - T_w}{T_r - T_c} - h\eta \tag{F-7}$$

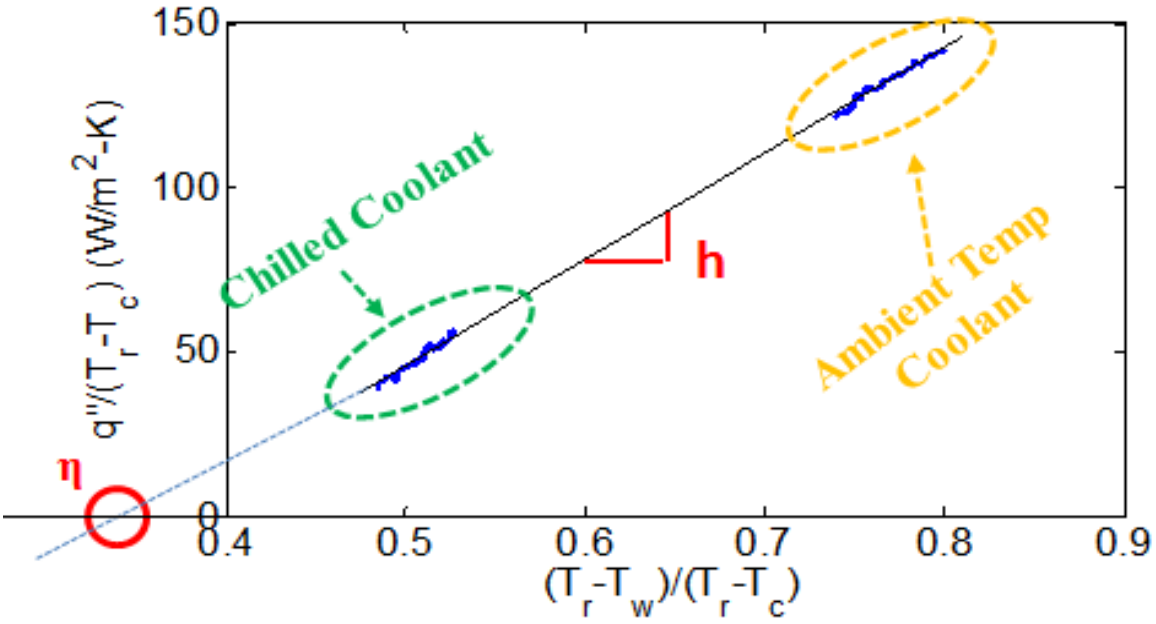

Figure F.2: A sample of dual linear regression applied to heat transfer data

References

[1] Xue, S., Roy, A., Ng, W. F., Ekkad, S. V., 2015, "A Novel Transient Technique to Determine Recovery Temperature, Heat Transfer coefficient, and Film Cooling Effectiveness Simultaneously in a Transonic Turbine Cascade", ASME J. Thermal Sci. and Eng. Appl. 7(1) Paper No. 011016

Appendix G: Uncertainty Analysis

This section provides a detailed discussion into the determination of the uncertainty associated with the heat transfer data presented in this manuscript. The experimental uncertainty associated with the heat transfer coefficient and film-cooling effectiveness measurements were calculated using a combination of two uncertainty calculation techniques: The perturbation technique as described by Moffat et al. [1] and the regression uncertainty technique described by Brown et al. [2].

The perturbation technique was used to determine the uncertainty in the calculated surface heat flux from the measured surface temperature. In this calculation, the surface temperature values which were input into the cook-felderman equation were "perturbed" by the IR temperature uncertainty, ∂T_w. The IR temperature reading uncertainty, ∂T_w, consists of a fixed "bias" error and a random "precision" error. However, only the precision error contributes to overall uncertainty of the heat flux due to the fact that the cook-felderman equation uses the temperature difference between two time steps. Figure G.1 summarizes the perturbation sequence for determining the uncertainty in the calculated wall heat flux.

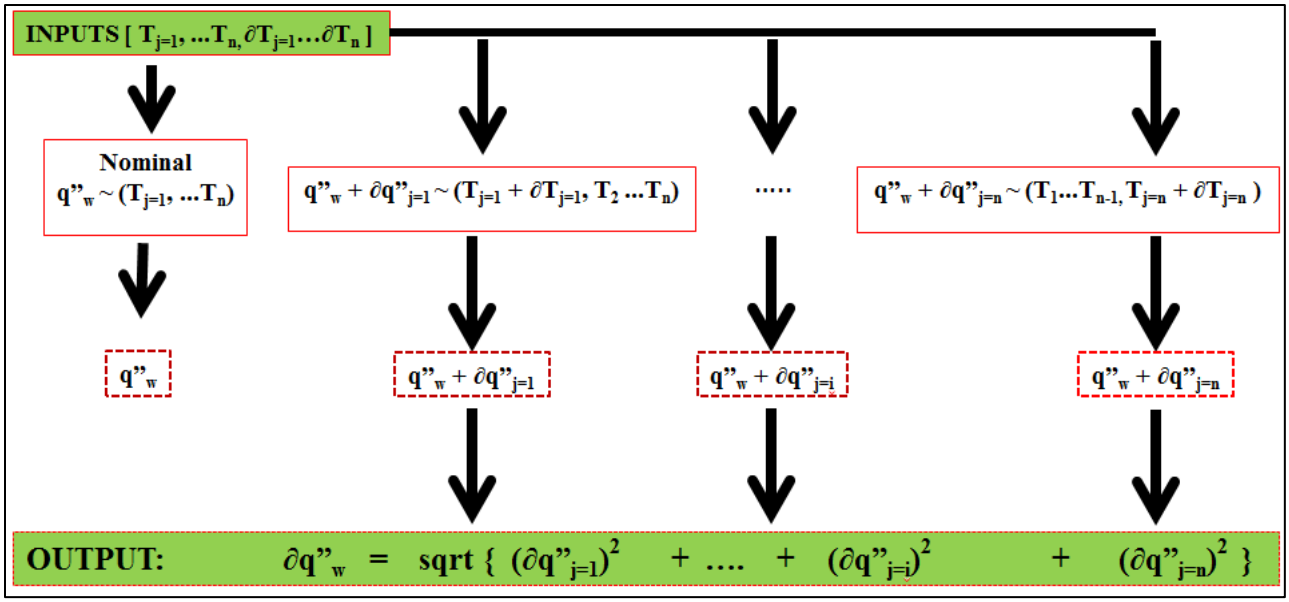

Figure G.1: A flow chart illustrating the application of the Moffats perturbation technique to determine the uncertainty in the calculated heat flux.

The regression uncertainty technique proposed by Brown et al. [2] was then used to determine the propagation of the heat flux and temperature uncertainties through the linear regression scheme to the calculated heat transfer coefficient. In other words, this regression uncertainty technique determines the uncertainty in the slope (heat transfer coefficient) and the x-intercept (recovery temperature/film-cooling effectiveness). According to Brown et al., for a regression scheme with known x and y values and their respective uncertainty, the uncertainty in the slope, *m*, is:

$$U_m^2 = \sum_{j=1}^{n} \left(\frac{dm}{dy_j}\right)^2 P_{yj}^2 + \sum_{j=1}^{n} \left(\frac{dm}{dy_j}\right)^2 B_{yj}^2 + \sum_{j=1}^{n} \left(\frac{dm}{dx_j}\right)^2 P_{xj}^2 + \sum_{j=1}^{n} \left(\frac{dm}{dx_j}\right)^2 B_{xj}^2$$

$$+ 2 \sum_{j=1}^{n-1} \sum_{k=1+1}^{n} \left(\frac{dm}{dy_j}\right)\left(\frac{dm}{dy_k}\right) B_{yj} B_{yk}$$

$$+ 2 \sum_{j=1}^{n-1} \sum_{k=1+1}^{n} \left(\frac{dm}{dx_j}\right)\left(\frac{dm}{dx_k}\right) B_{xj} B_{xk} + 2 \sum_{j=1}^{n} \sum_{k=1}^{n} \left(\frac{dm}{dy_j}\right)\left(\frac{dm}{dx_k}\right) B_{yj} B_{xk}$$

In this particular case, the x values could represent either; $-\frac{T_w}{T_{t,\infty}}$, $T_{t,\infty} - T_w$ or $\frac{T_r - T_w}{T_r - T_c}$ depending on the linearization form of heat transfer equation in the LR or DLR. Similarly, the y values represent either, $\frac{q''_w}{T_{t,\infty}}$, q''_w or $\frac{q''_w}{T_r - T_c}$ and the slope, *m*, represents the heat transfer coefficient, h.

Similarly, the uncertainty in the y-intercept value, *c*, is:

$$U_c^2 = \sum_{j=1}^{n} \left(\frac{dc}{dy_j}\right)^2 P_{yj}^2 + \sum_{j=1}^{n} \left(\frac{dc}{dy_j}\right)^2 B_{yj}^2 + \sum_{j=1}^{n} \left(\frac{dc}{dx_j}\right)^2 P_{xj}^2 + \sum_{j=1}^{n} \left(\frac{dc}{dx_j}\right)^2 B_{xj}^2$$

$$+ 2 \sum_{j=1}^{n-1} \sum_{k=1+1}^{n} \left(\frac{dc}{dy_j}\right)\left(\frac{dc}{dy_k}\right) B_{yj} B_{yk}$$

$$+ 2 \sum_{j=1}^{n-1} \sum_{k=1+1}^{n} \left(\frac{dc}{dx_j}\right)\left(\frac{dc}{dx_k}\right) B_{xj} B_{xk} + 2 \sum_{j=1}^{n} \sum_{k=1}^{n} \left(\frac{dc}{dy_j}\right)\left(\frac{dc}{dx_k}\right) B_{yj} B_{xk}$$

Where the partial derivatives are defined as follows:

$$\frac{dm}{dy_j} = \frac{n x_j - \sum_{j=1}^{n} x_j}{n \sum_{j=1}^{n} \left(x_j^2\right) - \left(\sum_{j=1}^{n} x_j\right)^2}$$

$$\frac{dc}{dy_j} = \frac{\sum_{j=1}^{n} (x_j^2) - x_j \sum_{j=1}^{n} x_j}{n \sum_{j=1}^{n} \left(x_j^2\right) - \left(\sum_{j=1}^{n} x_j\right)^2}$$

$$\frac{dm}{dx_j} = \frac{n y_j - \sum_{j=1}^{n} y_j}{n \sum_{j=1}^{n} \left(x_j^2\right) - \left(\sum_{j=1}^{n} x_j\right)^2} - \frac{\{n \sum_{j=1}^{n} x_j y_j - \sum_{j=1}^{n} x_j \sum_{j=1}^{n} y_j\} \quad \{2n x_j - 2 \sum_{j=1}^{n} x_j\}}{\{n \sum_{j=1}^{n} \left(x_j^2\right) - \left(\sum_{j=1}^{n} x_j\right)^2\}^2}$$

$$\frac{dc}{dx_j} = \frac{2x_j \sum_{j=1}^{n} y_j - \sum_{j=1}^{n} x_j y_j - y_j \sum_{j=1}^{n} x_j}{n\sum_{j=1}^{n}(x_j^2) - (\sum_{j=1}^{n} x_j)^2} - \frac{\{\sum_{j=1}^{n}(x_j^2)\sum_{j=1}^{n} y_j - \sum_{j=1}^{n} x_j \sum_{j=1}^{n} x_j y_j\} \quad \{2nx_j - 2\sum_{j=1}^{n} x_j\}}{\{n\sum_{j=1}^{n}(x_j^2) - (\sum_{j=1}^{n} x_j)^2\}^2}$$

To find the uncertainty interval for the x-intercept (η), the "large sample assumption" was made and the 95% confidence expression for U_η becomes:

$$U_\eta = \sqrt{U_m^2 + U_c^2}$$

B =bias limit

$B_{ik} = B_i B_k$ = covariance estimator

c = y-intercept

m = line slope

n = number of data points

U = uncertainty

x = independent variable

y = dependent variable

The average uncertainty calculated for the rotor tip and endwall heat transfer coefficients was found to be approximately ±9.6%. The uncertainty in the tip film-cooling effectiveness, Eta, was approximately ±0.102%. All of these uncertainties had a confidence interval of 95% which is equivalent to two standard deviations. It is worth noting that the uncertainty in the tunnel Mach number condition plays a role towards the measured heat transfer. However, it is not necessary to "double count" this in the uncertainty analysis since the observed/measured wall temperature varies with the Mach number. Therefore, uncertainty in heat transfer due to Mach number uncertainty is indirectly accounted for in the measured wall temperature values. The same applies for other aerodynamic fluid variables.

References

[1] Moffat, R. J., 1988, "*Describing Uncertainties in Experimental Results*," Exp. Thermal and Fluid Science, 1988, pp. 3-17.

[2] Brown, K. H., Coleman, H. W., and Steele, W. G., 1995, "*Estimating Uncertainty Intervals for Linear Regression*," AIAA–1995-0796.

Appendix H: Cascade Inlet Flow Characteristics

This section presents data collected on the vane cascade inlet conditions. The inlet conditions play an important role in the aerodynamic and heat transfer characteristics observed on the cascade passage. It aides in understanding the underlying physics within the cascade. Furthermore, this data was important for use as boundary conditions for numerical modelling of the cascade. The pressure, temperature and turbulence characteristics were measured slightly upstream of the inlet plane of the vane cascade test section. The inlet plane was located at 0.48C upstream of the vane leading edge and the measurements were taken at 1C upstream of the leading edge. Ideally, it was desired to take these measurements at the inlet plane. However, this was not feasible without additional cost/time because the combustor-turbine transition feature was located here.

The inlet pressure profile was measured using a pitot-static probe which was placed at eight different spanwise locations between midspan and the endwall as marked in Figure H.1. It was important that the probe was carefully aligned with the mainstream flow. Only the static pressure was measured at the endwall surface ($z/S = 0$) and because of the no slip boundary layer condition at the wall, the static pressure is equal to the total pressure at the wall. The data was then normalized as a ratio of the static pressure to total pressure.

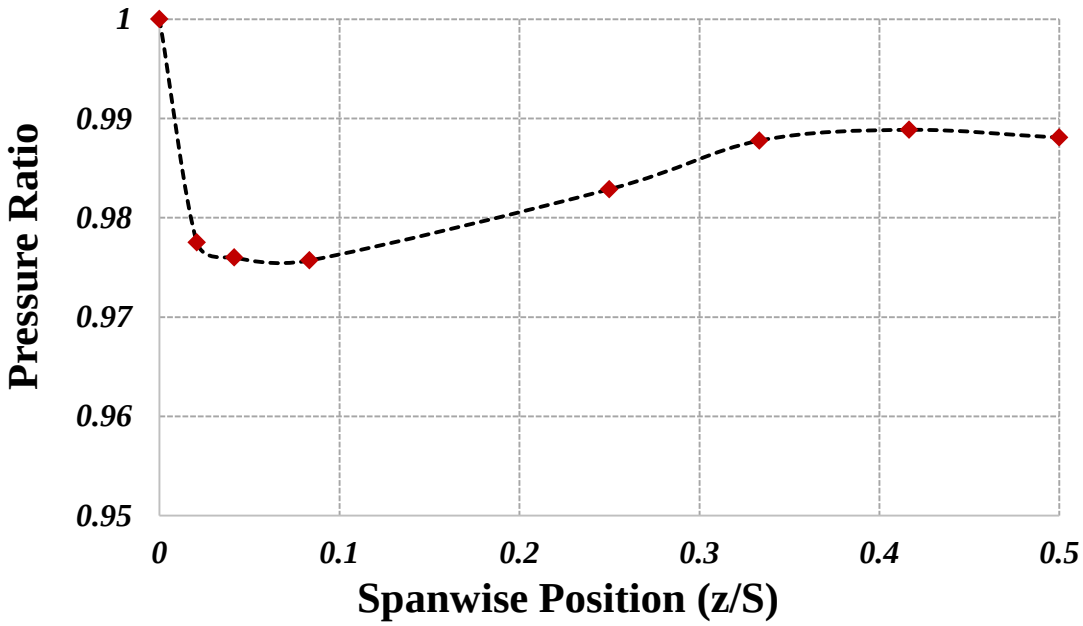

Figure H.1: Spanwise variation of the pressure ratio at the cascade inlet mid-pitch.

It is also important to fully understand the near-wall turbulence and thermal characteristics as this are key parameters that influence heat transfer. The midspan turbulence intensity and lengthscale for a similar cascade setup and flow conditions was measured by Nasir et al. [1] using hotwire anemometry at the inlet plane located 0.48C upstream of the leading edge. In this research work, we were interested in resolving the spanwise and pitchwise variation of these turbulence parameters and establish their effect on the CFD heat transfer prediction. The turbulence parameters were measured at six spanwise locations at the passage mid-pitch and three pitchwise locations close to the endwall.

Hot wire anemometry uses the relationship between the local heat transfer coefficient and its effect on the power fluctuations supplied to maintain a constant temperature of a thin wire exposed to the flow. The power fluctuation is then used to estimate the local velocity within the flow. A hot wire anemometry system usually consists of a very small, thin metallic wire which is connected to a Wheatstone bridge. The output voltage from this bridge is amplified, filtered, and recorded. In order to relate the output voltage from this device to a velocity, a calibration curve is

developed by placing the hot wire system in a laminar flow field along with a pitot-static probe. The velocity of this laminar flow field is varied slowly across a range of velocities while the velocity and hot wire voltage are recorded simultaneously. The results from this test are used to find the constants, A, B, and n for King's Law, which relates the hot wire voltage, E, to the local fluid velocity, u. The constant n is typically between 0.4 and 0.9 while A and B vary depending on the size and shape of the wire exposed to the flow. An example of a calibration curve is shown in Figure H.2 below.

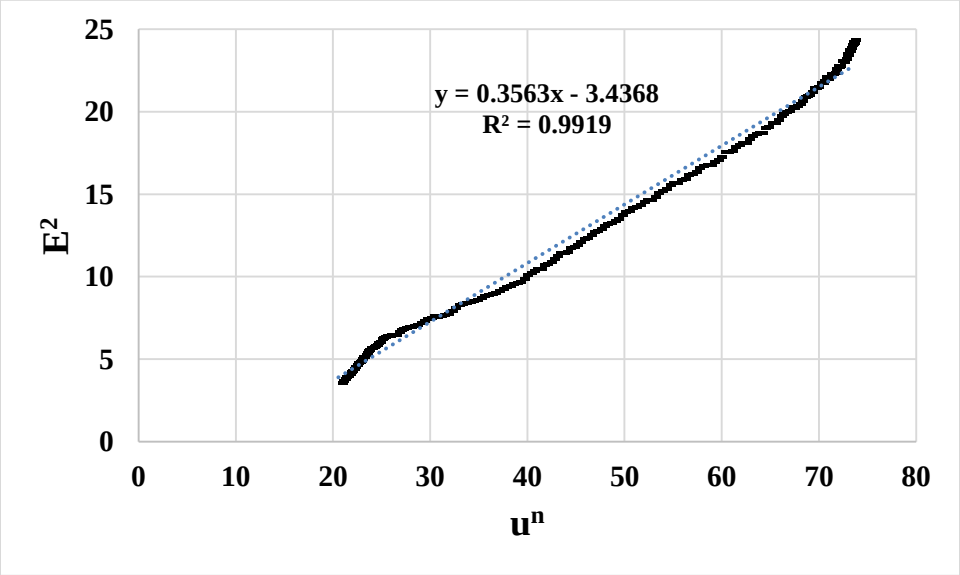

Figure H.2: Sample hotwire calibration curve

$$E^2 = A + Bu^n \text{ (King's Law)}$$

Once the constants for the calibration curve have been found, the hot wire can be used to determine the turbulence intensity. High frequency measurements (> 100 kHz) are taken by the hot wire at the desired locations with the flow in the cascade being aerodynamically steady. The velocity of the flow at the measured location is then calculated using King's Law. The turbulence intensity at this location is found by calculating the RMS value of the velocity data and dividing it by the average velocity. The spanwise variation of turbulence intensity at mid-pitch is shown

in Figure H.3. The turbulence intensity or u_{rms} increases as one moves from the freestream towards the wall due to increasing shear/velocity gradients. Turbulence is an instability that is produced by shear. However, at the region much closer to the wall the turbulence intensity drops drastically and reaches zero at the wall. This is because of the no slip boundary condition at the wall and creates a thin region with very little turbulence known as the laminar sub-layer.

$$u_{rms} = \sqrt{\overline{u'(t)^2}}$$

$$\text{Turbulence Intensity, Tu} = \frac{U_{rms}}{\bar{U}}$$

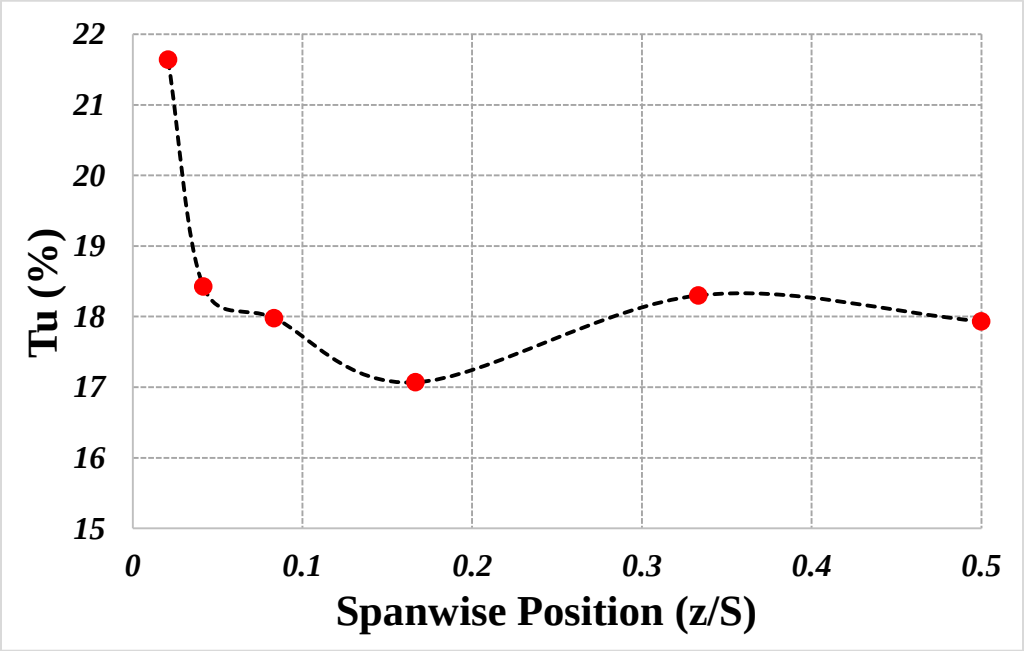

Figure H.3: Spanwise variation of the turbulence intensity at the cascade inlet mid-pitch

The variation of the integral length scale with span was also calculated. The integral lengthscale is a measure of the scale for the largest energy containing eddies in a flow. The integral length scale was determined by first performing an autocorrelation on the velocity fluctuations recorded from the hot wire measurement. The sum of all the autocorrelation values from the start of the run until the point where the correlation drops below zero was found and

divided by the recording frequency. Multiplying this value by the mean velocity gives the integral length scale. Figure H.4 shows the variation of the length scale with span at mid-pitch.

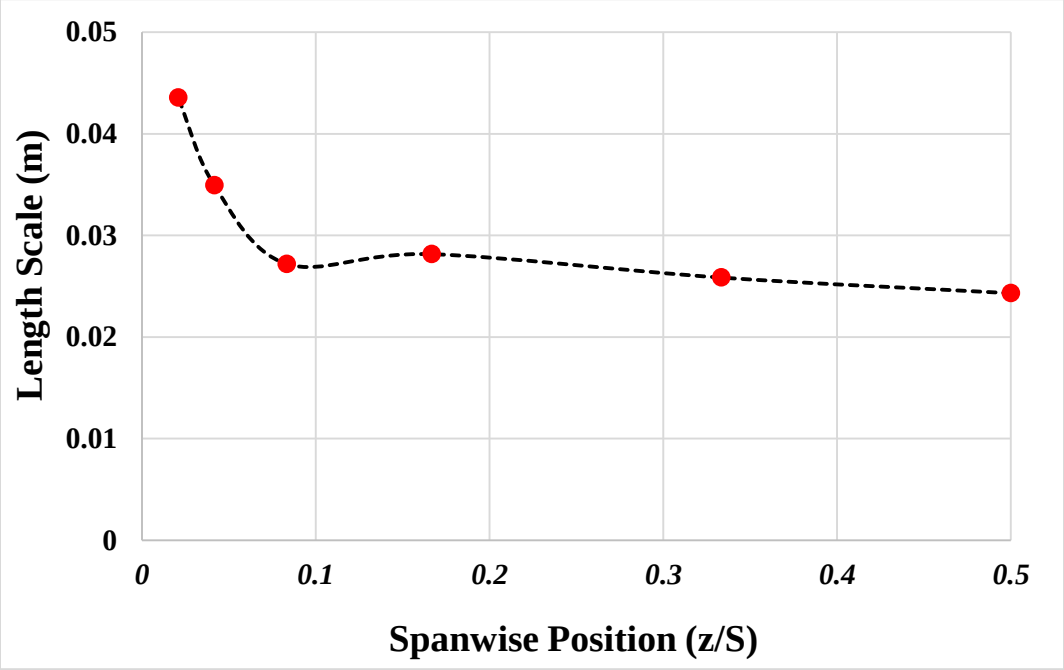

Figure H.4: Spanwise variation of the integral length scale at the cascade inlet mid-pitch

Finally, the variation of the turbulence characteristics with pitch close to the endwall was also investigated i.e. at z/S = 0.0208 (0.125 in) from the endwall. The pitchwise variation of the turbulence characteristics was relatively uniform compared to the range of variation in the spanwise direction. The pitchwise variation of these turbulence parameters is shown in Figure H.5 and Figure H.6. The sensitivity of the CFD heat transfer prediction to inlet profiles was extensively investigated.

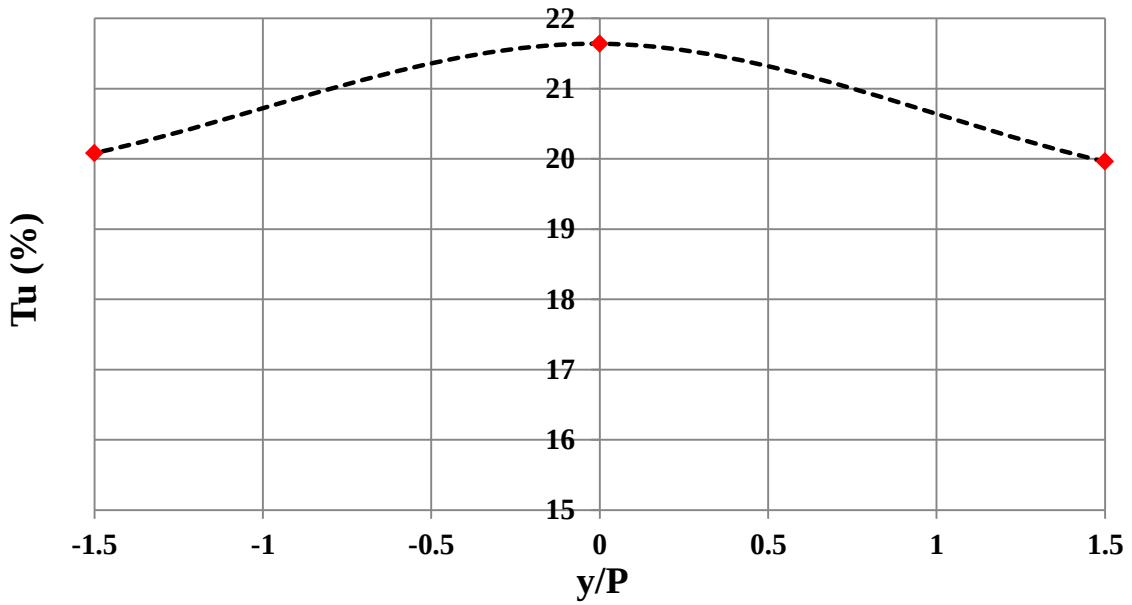

Figure H.5: Pitchwise variation of the turbulence length scale close to the endwall surface

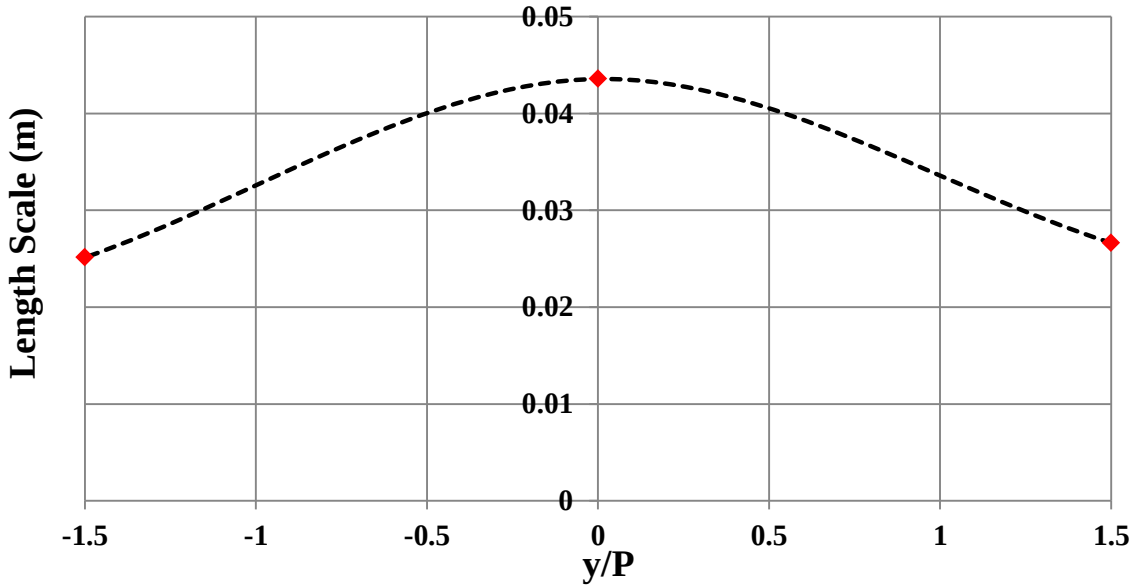

Figure H.6: Pitchwise variation of the integral length scale close to the endwall surface

The effect of having these inlet aerodynamic and thermal variable profiles on the endwall heat transfer prediction by CFD was extensively investigated. It was found that the CFD prediction of the heat transfer coefficient at the turbine extremity surfaces, especially the near-tip region, was affected by the inlet momentum and thermal profile. However, the heat transfer prediction was generally unaffected by the turbulence variables profiles i.e. the heat transfer

prediction using a uniform turbulence condition at the inlet was very similar to that using the measured inlet turbulence profiles. Instead, a strong sensitivity to the level of inlet turbulence length scale was noted.

It is also worth noting that the experimentally measured integral turbulence length scale is different from that inputted at the CFD inlet boundary. This is because the integral length scale defines the size of the largest eddies in the flow. On the other hand, the lengthscale defined at the CFD inlet boundary is representative of the average length scale of the energy containing eddies. A study carried out by Luo and Razinsky [2], determined that a good approximation of the energy average lengthscale can be found by multiplying the integral lengthscale by 1/5.

References

[1] Nasir, S., Carullo, J.S., Ng, W.F., Thole, K.A., Wu, H., Zhang, L.J., and Moon, H.K., 2009, "*Effects of Large Scale High Freestream Turbulence, and Exit Reynolds Number on Turbine Vane Heat Transfer in a Transonic Cascade*," ASME J. Turbomach., Vol. 131, 021021.

[2] Luo, J., and Razinsky, E.H., 2008, "*Prediction of Heat transfer and Flow Transition on Transonic Turbine Airfoils under High Freestream Turbulence*," Proceedings of ASME Turbo Expo GT2008-50868.

Appendix I: Endwall Pressure Measurement

The following static pressure port locations are measured from the leading edge (x/C_x = 0, y/P = 0) of the upper vane bounding the center passage within the test section.

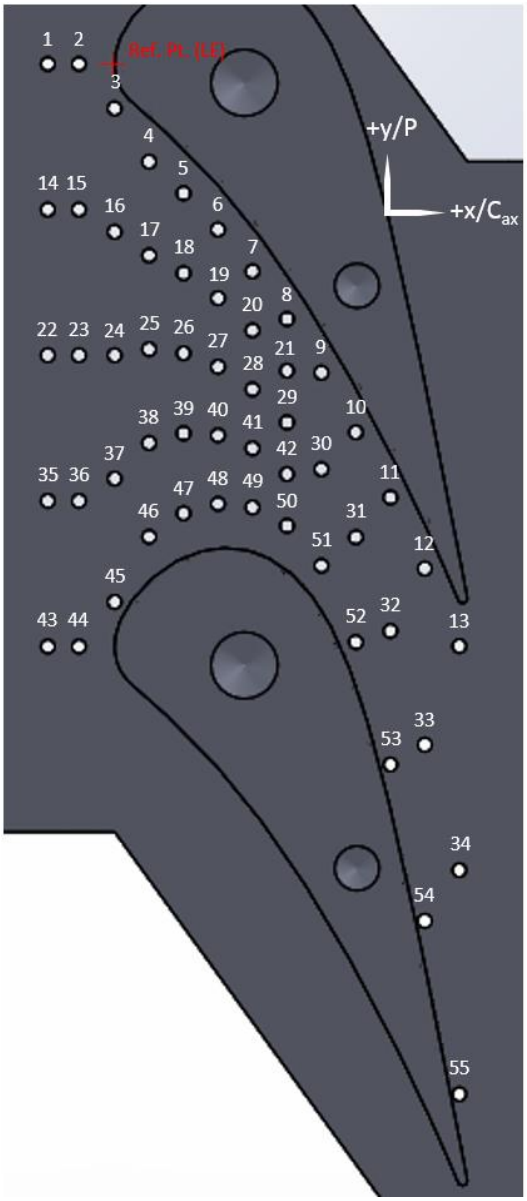

Figure I.1: Endwall static pressure port locations with the reference leading edge point marked

Table I.1: Passage Endwall pressure measurement port locations

	x/C_x	y/P
1	-0.190500	0.000000
2	-0.101600	0.000000
3	0.000000	-0.076506
4	0.098227	-0.168086
5	0.196454	-0.222356
6	0.294681	-0.284802
7	0.392908	-0.356623
8	0.491136	-0.438624
9	0.589363	-0.531004
10	0.687590	-0.633403
11	0.785817	-0.745451
12	0.884044	-0.867866
13	0.982271	-1.001123
14	-0.190500	-0.250458
15	-0.101600	-0.250458
16	0.000000	-0.288711
17	0.098227	-0.329351
18	0.196454	-0.359956
19	0.294681	-0.402744
20	0.392908	-0.458129
21	0.491136	-0.527518
22	-0.190500	-0.500916
23	-0.101600	-0.500916
24	0.000000	-0.500916
25	0.098227	-0.490616
26	0.196454	-0.497557
27	0.294681	-0.520686
28	0.392908	-0.559635
29	0.491136	-0.616413
30	0.589363	-0.696956
31	0.687590	-0.813876
32	0.785817	-0.975121
33	0.884044	-1.170783
34	0.982271	-1.386437
35	-0.190500	-0.751373
36	-0.101600	-0.751373
37	0.000000	-0.713120
38	0.098227	-0.651881
39	0.196454	-0.635157
40	0.294681	-0.638628

41	0.392908	-0.661141
42	0.491136	-0.705307
43	-0.190500	-1.001831
44	-0.101600	-1.001831
45	0.000000	-0.925325
46	0.098227	-0.813145
47	0.196454	-0.772757
48	0.294681	-0.756570
49	0.392908	-0.762647
50	0.491136	-0.794202
51	0.589363	-0.862909
52	0.687590	-0.994349
53	0.785817	-1.204791
54	0.884044	-1.473699
55	0.982271	-1.771750